ENERGY TRANSFER AND GAS DIFFUSION AT GAS-LIQUID INTERFACES

A Dissertation

presented to

the Faculty of the Graduate School

at the University of Missouri-Columbia

In Partial Fulfillment

of the Requirements for the Degree

Doctor of Philosophy

---

by

DANIEL J. SHAUGHNESSY

Dr. John E. Adams, Dissertation Supervisor

MAY 2015

The undersigned, appointed by the dean of the Graduate School, have examined the dissertation entitled

ENERGY TRANFER AND GAS DIFFUSION
AT GAS-LIQUID INTERFACES

presented by Daniel J. Shaughnessy,

a candidate for the degree of Doctor of Philosophy,

and hereby certify that, in their opinion, it is worthy of acceptance.

Professor John E. Adams

Professor Carol A. Deakyne

Professor Jerry L. Atwood

Professor Ioan Kosztin

ACKNOWLEDGMENTS

I would like to express my gratitude to the following people, without whom I would not have been able to successfully complete my work. First and foremost, I'd like to thank my advisor, Dr. John Adams for his guidance, extensive knowledge, kindness and the Zen-like patience he had with me at times while I was his student. I would also like to thank Dr. Carol Deakyne for help with all matters of quantum chemistry, Gaussian, and for always having an encouraging word when I needed one. I'd like to thank Dr. Tommy Sewell for his help in understanding quantum chemistry and statistical mechanics. I'd also like to extend my thanks to Dr. Gary Baker for his useful discussions with me on ionic liquids. I am thankful to Dr. John Simpson, Dr. Megan Coleman, Dr. Eric Weiss, and Dr. Beau Ballard for many useful conversations on chemistry, graduate school, and life, the universe, and everything. I'd additionally like to thank past and present members of the Adams and Deakyne groups, Dr. Haunani Thomas, Jack Cox, Katie Brewer, Collin Mayhan and Matthew Briete, for their continued support and help. I'd like to thank Mr. Phil Silverman for making my teaching job easier, and for the innumerable cups of coffee. I'd like to thank Mr. Jerry Brightwell for always helping me with registration and anything else I needed help with. I'd like to extend a special thanks to Dr. Richard Metzler for his many late-night talks with me on science and everything else. And lastly, I'd like to thank Dr. Carol Roach for her continuing love, support, and knowledge of MATLAB.

TABLE OF CONTENTS

ACKNOWLEDGEMENTS……...ii

LIST OF TABLES……...v

LIST OF FIGURES……....vi

ABSTRACT…...……...……...……..ix

Chapter 1……...1

Introduction……1

Chapter 2……..8

Energy Transfer of a CO_2 Molecule Scattering at a Lennard-Jones Gas-Liquid Interface…….....8

I. Introduction……....8
II. Computational Methods.……...15
III. Results and Discussion…..……....22
1. Varying Incident Energy Results...……...……...22
2. Varying Incidence Angle Results ……36
3. Varying Initial Temperature Results……...…….46
IV. Conclusion……..……...65
V. Possibilities for Future Study…...……..67

Chapter 3……...70

Introduction: Room Temperature Ionic Liquids.....……70

Chapter 4……74

Gas Diffusion in Room-Temperature Ionic Liquids……..74

I. Introduction……...74
II. Computational Methods……76
III. Results and Discussion……..84
IV. Conclusion……...101
V. Possibilities for Future Study……..103

Appendix A……105

Appendix B……109

References Cited……119

Vita……127

LIST OF TABLES

Table Page

2.1. Average Final CO_2 translational and rotational energy values, 436 K liquid In surface, 55^0 incidence angle, IS and TD channel distributions……23

2.2. Average CO_2 translational and rotational energy values, 436 K liquid In surface, 55^0 incidence angle, TD channel, surface step distribution……27

2.3. Average CO_2 translational and rotational energy values, 436 K liquid temperature, 22.5^0 incidence angle……37

2.4. Average CO_2 translational and rotational energy values, 436 K liquid temperature, 0^0 incidence angle……..44

2.5. TD channel fractional occupancy……45

2.6. Average CO_2 translational and rotational energy values, 459 K liquid In surface, 55^0 incidence angle……..47

2.7. Average CO_2 translational and rotational energy values, 511K liquid surface, 55^0 incidence angle……...51

2.8. Average CO_2 translational and rotational energy values, 560 K liquid In surface, 55^0 incidence angle……..56

2.9. Fraction of trajectories scattered via the TD channel, 55^0 incidence angle……..60

4.1. Average density values for bmim-PF_6 from our computations compared to experimental values from Lopes et al.[1]……..84

4.2. Diffusion constants for cation and anion species, 10^{-6} cm^2/sec, with comparison literature values from Bhargava et al.[2]……..93

4.3. Diffusion constants for cation and anion species calculated using VACF, 10^{-6} cm^2/sec, with comparison literature values……94

4.4. Calculated diffusion constants for gas species, 10^{-6} cm^2/sec, Trapped results marked with asterisk……..…….98

LIST OF FIGURES

Figure Page

1-1. Diagram of a common MBS setup, used by Nathanson et al.[3]…..……..3

2-1. Diagram of trajectory steps...…….……...10

2-2. Percent Histogram Bin Occupancy vs. CO_2 Translational Energy, 436 K liquid temperature, 55^0 incidence angle, Surface Step Distribution, TD channel……25

2-3. Percent Time Occupancy vs. Gas center-of-mass z-coordinate, 436 K liquid temperature, 55^0 incidence angle, Scattering Step Distribution, TD channel……29

2-4. Percent Histogram Bin Occupancy vs. Final CO_2 Translational Energy, 436 K liquid temperature, 55^0 incident CO_2 angle, IS and TD channel distributions……...30

2-5. Average Energy vs. CO_2 center-of-mass z-coordinate, 436 K liquid temperature, 55^0 incidence angle, TD channel…….……..32

2-6. Diagram of long-range attractive forces acting on CO_2 while CO_2 is on the liquid surface……34

2-7. Percent Histogram Bin Occupancy vs. CO_2 Translation Energy, 436 K liquid temperature, 22.5^0 and 55^0 incidence angles, IS channel distributions……..36

2-8. Percent Histogram Bin Occupancy vs. CO_2 Rotational Energy, 436 K liquid temperature, 22.5^0 and 55^0 incidence angles, IS channel distributions.....……..….37

2-9. Percent Histogram Bin Occupancy vs. CO_2 Translation Energy, 436 K liquid temperature, 22.5^0 incidence angle, 6.25kJ/mol incident energy, IS and TD channel.....40

2-10. Percent Histogram Bin Occupancy vs. CO_2 Translational Energy, 436 K liquid temperature, 22.5^0 incidence angle, Surface Step Distribution, TD channel…….41

2-11. Average Energy vs. CO_2 center-of-mass z-coordinate, 436 K liquid temperature, 22.5^0 incidence angle, TD channel……43

2-12. Percent Histogram Bin Occupancy vs. CO_2 Translational Energy, 55^0 Incidence angle, 459K temperature, surface step distribution, TD channel……..48

2-13. Percent Time Occupancy vs. CO_2 center-of-mass z-coordinate, 459K liquid temperature, 55^0 incidence angle, Scattering Step Distribution, TD channel……...49

Figure Page

2-14. Average CO_2 Energy vs. CO_2 center-of-mass z-coordinate, 459 K liquid temperature, 55^0 incidence angle, TD channel……..51

2-15. Percent Time Occupancy vs. CO_2 center-of-mass z-coordinate, 511 K liquid temperature, 55^0 incidence angle, TD channel……..53

2-16. Percent Histogram Bin Occupancy vs. CO2 Translational Energy, 55^0 Incidence angle, 511K temperature, surface step distribution, TD channel……...54

2-17. Average CO_2 Energy vs. CO_2 center-of-mass z-coordinate, 511K liquid temperature, 55^0 incidence angle, TD channel……...……...54

2-18. Percent Time Occupancy vs. CO_2 center-of-mass z-coordinate, 560K liquid temperature, 55^0 incidence angle, Scattering Step Distribution, TD channel……57

2-19. Percent Histogram Bin Occupancy vs. CO_2 Translational Energy, 55^0 Incidence angle, 560K temperature, surface step distribution, TD channel……...58

2-20. Average Energy vs. CO_2 center-of-mass z-coordinate, 560K liquid temperature, 55^0 incidence angle, TD channel……...59

2-21. Natural logarithm of the fraction of species remaining on the surface vs. Time……...63

2-22. Percent Time Occupancy vs. CO_2 center-of-mass z-coordinate position, TD channel distributions……..64

4-1. bmim PF_6 Density vs. Temperature, calculated and experimental values……85

4-2. Histogram Bin Occupancy vs. Center-of-mass z-coordinate, 300K initial temperature……86

4-3. MSD (in cm^2) vs. Time Interval, 300 K liquid temperature, methane diffusing gas……..88

4-4. MSD in cm^2 vs. Time Interval in seconds, 500 K liquid temperature, methane diffusing gas……...88

4-5. MSD vs. Time Interval, x, y, z components, 300 K liquid temperature, methane diffusing gas……...89

4-6. MSD vs. Time Interval, x, y, z components, 500 K liquid temperature, methane diffusing gas……...90

Figure Page

4-7. MSD vs. Time Interval, 300 K liquid temperature, cation distribution……....92

4-8. Normalized Cation and Anion VACF vs. Time interval…..…….….95

4-9. Methane VACF vs. Time Interval……...…….…….96

4-10. Running Numeric Integral of Methane VACF vs. Time interval, 300K…….....97

4-11. Diffusion constant, $10^{-6}cm^2/sec$ vs. Gas Species Mass…...……..…...99

4-12. Diffusion constant, $10^{-6}cm^2/sec$ vs. Gas Species Dipole moment……..100

ENERGY TRANSFER AND GAS DIFFUSION

AT GAS-LIQUID INTERFACES

Daniel J. Shaughnessy

Dr. John E. Adams, Dissertation Supervisor

ABSTRACT

The interactions of gasses and liquids play an important role in many systems in chemistry. Gas-liquid surface scattering techniques are a useful tool towards the investigation of energy transfer resulting from gas-liquid collisions. We use molecular dynamics to simulate surface scattering in order to investigate the effects of incident energy, incidence angle, and surface temperature on energy transfer of a CO_2 molecule scattering from a liquid indium surface modeled as a simple Lennard-Jones liquid. We focus our investigation on the two-channel theory of gas-liquid scattering with a primary focus on the trapping-desorption scattering channel. We use a novel technique to investigate the average trajectory of the scattering gas species to determine the effects of energy transfer on this channel. We find species scattering via this channel are unaffected by incident energy and incidence angle in agreement with experimental trends. We find our gas species scattered by the trapping desorption channel emerge with four degrees of freedom thermalized to the surface temperature, with substantial variance in the translational degree of freedom in the surface normal direction which we attribute to both the enthalpy of desorption and interactions with vapor-phase indium atoms. We observe a substantial increase in interactions with vapor-phase indium with increasing temperature.

Our second simulation uses molecular dynamics to examine the diffusion of various gas species through a room temperature ionic liquid at standard pressure conditions. We were able to replicate the bulk properties of the bmim PF_6 ionic liquid with reasonable accuracy compared with other experimental and theoretical work. We varied the gas species mass, the gas species dipole moment, and the ionic liquid temperature to examine the effects of each variable on gas diffusivity. We find a general trend of increased diffusivity with increasing temperature; however, we are unable to discern a definite trend relating to gas species mass or dipole moment. We observe significant short-time trapping effects on our diffusing gas species, particularly at low temperatures, that make examining the diffusivity of our gases problematic.

Chapter 1

Introduction

The interactions of gases and liquids play an important role in many systems in the physical world. These interactions are of great importance to chemical, biological, environmental, and mechanical processes encountered in everyday life. Chemical processes such as synthesis and chromatographic analysis techniques are influenced by the interactions of gases and liquids. Biological processes such as respiration and photosynthesis make use of gas-liquid interactions in order to function. Precipitation and the absorption of gases into water play an important role in the environment and the maintenance of habitable conditions for many forms of life. Most forms of mechanical and electrical energy are generated through the uses of either boiling water to form high-pressure steam or the direct combustion of some form of fuel.[4-9]

In chemistry, the effects of gas-liquid interactions have long been observed, such as phase changes, the vapor pressure of liquids, and the absorption of gases onto surfaces by physisorption and chemisorption.[10] While there is a good deal of scientific theory and understanding of the effects of these interactions, until recently there has been little theory on the mechanisms by which many of these interactions function. The confluence

of statistical mechanics and computational chemistry, along with computer systems powerful enough to model complex chemical systems, has allowed us to begin to understand the means by which these interactions function at a fundamental level. Additionally, an increase in understanding of the liquid phase has allowed for computational models which can model liquid systems with reasonable accuracy.

The emergence of molecular beam scattering (MBS) and other surface sensitive techniques has provided powerful tools for experimental examination of energy changes in gas species interacting with liquid surfaces.[11] Surface scattering experiments on liquids commonly use two methods to generate liquid surfaces. The first, used by Nathanson et al,[3, 11] uses a rotating wheel to draw a thin film of liquid from a temperature regulated reservoir. The second, used by Lu et al, creates a self-assembled liquid monolayer on a temperature regulated metal plate.[12-13] The liquid surface is held at a fixed angle to an incident beam of gas particles generated at constant energy. These beams are generated by expanding a high pressure gas adiabatically through a nozzle with a ~1mm opening. The incident energy of the gas beam is controlled by the thermodynamics of the gas expansion and the geometry of the nozzle system. A detector is typically placed at the exit angle of interest for a given set of initial conditions. Mass spectrometry and laser measurement are commonly used to determine the translational energy of the scattering gas species,[14] while IR and RAMAN spectroscopy have been used to examine vibrational and rotational energy levels of the scattered gas.[15] A diagram of a common experimental setup for MBS on liquids is displayed below in figure

1-1. These experiments are performed under ultrahigh vacuum to remove the interference of gas-phase molecules on the molecular beam.[11]

Figure 1-1. Diagram of a common MBS setup, used by Nathanson et al.[3]

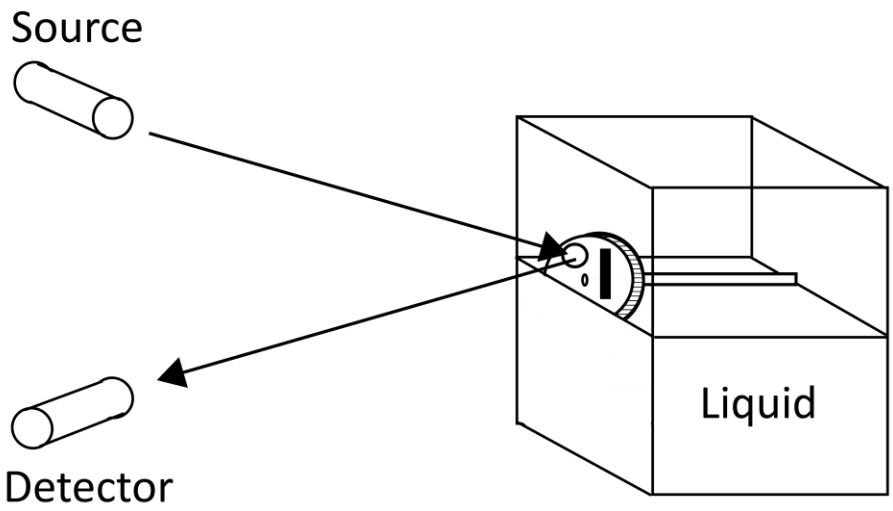

The common experimental setup for liquid scattering experiments is relatively easy to replicate using molecular dynamics (MD). While there is no commercially available MD software that models surface scattering, it is possible to modify existing MD programs in order to support surface scattering functionality. Several gas-liquid scattering studies have been performed using MD[16-20] and have found good agreement with similar experimental studies.[13-14, 21-24] Molecular dynamics simulations offer several advantages over experimental study when examining gas-liquid surface scattering. Unlike experimental setups which rely on a fixed detector, it is possible to track species that scatter to angles outside the plane of the detector. Furthermore, we are able to examine all of the internal degrees of freedom of the scattered species without resorting

to using multiple kinds of detectors. We also are able to track the entire trajectory of the incident gas particle instead of relying on a snapshot taken after the incident species has scattered. Additionally, MD is potentially far more cost effective, as the cost of all the equipment necessary for surface scattering experiments can be prohibitive.

Recent experimental[3, 12-14, 23] and computational[17-20] studies of gas-liquid scattering have shown considerable evidence that gasses scatter from liquids by two distinct channels: 1.) inelastic scattering (IS) and 2.) trapping-desorption (TD). The IS channel consists of species that undergo few collisions with the surface and retain some memory of their initial trajectories subsequent to scattering from the surface, while the TD channel consists of species that undergo enough collisions with the surface to equilibrate to the surface temperature prior to desorbing from the surface. The final observed distribution of gas energies is commonly separated into these channels for analysis by either trajectory time of flight (TOF)[11-12, 14, 20] or scattering angle[25]. Time of flight separates these channels based on the assumption that species scattered by the IS channel will have significantly shorter residence times on the surface and significantly higher energies than those scattered by the TD channel, thus resulting in a shorter average TOF. Scattering angle is used to separate these channels based on the assumption that angles closer to the angle normal to the surface are favored by the TD channel, while angles closer to the incidence angle will be favored by the IS channel. Both of these methods have inherent flaws in their ability to separate the scattering channels. In the case of TOF, species that scatter via the IS channel and exit the surface at low energy will have a longer TOF than expected and thus potentially be counted as part of the TD

channel distribution. In the case of scattering angle, it has been shown that the roughness of the liquid surface can yield angles closer to the angle normal to the surface even in the IS channel distribution.[25]

The total distribution of final energy states of the scattering species is typically represented by a function defined by the sum of the IS and TD channel energy distribution functions multiplied by their fractional occurrences.[14] The energy distributions of gas species scattered by the TD channel have been assumed to conform to Maxwell-Boltzmann distributions about the liquid surface temperature (T_s).[11, 13-14, 20, 23, 26] Several methods have been proposed to fit the IS channel energy distributions. One of the most common techniques is to fit the energy distribution to a Maxwell-Boltzmann distribution consistent with the incident energy of the gas species multiplied by a function accounting for gas species energy loss resulting from inelastic collisions with the surface.[14] When the total energy distribution is separated into its IS and TD channel components as discussed above it becomes trivial to estimate the fractional occurrence of each scattering channel, thus allowing ready computation of the total energy distribution function. This method of analysis has been shown to yield functions that conform well to the final observed energy distributions of both the translational and rotational degrees of freedom for various gas species in both experimental[13-14, 27] and computational[16-18, 20] results.

While recent experimental and computational efforts have provided new and significant insights into the basic mechanics of gas-liquid interactions, a full understanding of the underlying mechanisms by which energy exchange occurs at gas-

liquid interfaces remains elusive. In order to provide further insight into the underlying mechanisms of gas-liquid energy exchange, we have used MD simulation techniques to model a common experimental setup for MBS. Previous efforts by our group focused on the scattering of noble gasses from both liquid metal and nitromethane surfaces.[20] We use a similar method to study the effects of CO_2 scattering from a liquid indium surface over a range of initial conditions. We hope our present work will provide further insight into both the effects of vapor pressure on gas-liquid scattering interactions and the mechanism by which energy exchange occurs in the TD scattering channel.

We additionally use MD to simulate the diffusion of various gas species through the 1-butyl-3-methylimidazolium hexafluorophosphate room-temperature ionic liquid. We are able to approximate the bulk properties of the bmim-PF6 system with reasonable accuracy using a relatively small system size. We examine the effects of the gas species' mass, the gas species' dipole moment, and liquid temperature on the diffusion of gases in an effort to elucidate the important parameters governing gas diffusion rates. In an effort to identify the most efficient methodology, we examine diffusivity using both the Einstein method (mean square displacement) and the Green-Kubo method (velocity autocorrelation).

In the following chapter, we will present our rationale for our specific computations, our computational methods, and our findings on the scattering of CO_2 from liquid indium surfaces over a range of initial conditions. We will discuss in further detail the mechanism by which energy exchanges occur in the TD scattering channel in the context of our results and examine the implications of our results in terms of both general

thermodynamics and statistical mechanics. We will additionally examine the effects of vapor pressure on gas scattering in both the IS and TD scattering channels and hope to provide insight into the effects of vapor pressure on gas-liquid energy exchange.

Chapter 2

Energy Transfer of a CO_2 Molecule Scattering at a Lennard-Jones Gas-Liquid Interface

I. Introduction

The role of surfaces in the exchange of energy is of fundamental importance to many applications of chemistry. Surface interactions play an integral role in the catalysis of many chemical reactions,[28] and have important effects relating to phase changes, absorption, and the behavior of the solid and liquid phases of matter. Surfaces have been examined experimentally for at least the last half century with increasingly refined techniques. Molecular beam scattering (MBS) has become a useful method for examining energy exchange between gasses and both solid and liquid surfaces.[11, 29] Several molecular dynamics (MD) studies have computationally replicated MBS experiments for several gas-liquid combinations[16-20] and found good agreement with experimental results.[13-15, 20, 30-31] These MD simulations have typically mirrored experimental studies by primarily examining the final energy states of gas particles that have scattered from a liquid surface. This method of analysis allows for direct

comparison with experimental results, but fails to make full use of the ability of MD to observe the gas species energy over the full course of a scattering trajectory.

The majority of gas-liquid scattering experiments use large organic molecules as their liquid surfaces due to their infinitesimal vapor pressures at ambient temperature, and thus their compatibility with the ultrahigh vacuum environments required for experimental scattering studies.[13, 15, 27, 30] Computations have likewise focused on liquids with infinitesimal vapor pressures in order to be directly comparable with experimental results.[16-19] These experiments yield in principle an understanding of gas-liquid interactions wherever vapor pressure effects can be ignored; however, many of these interactions in nature are influenced by vapor pressure effects. We use a liquid with finite vapor pressure at ambient temperature in our study in an effort to understand the effects of vapor pressure on gas-liquid scattering interactions.

It has been noted that determining an average trajectory for gas-liquid scattering would be useful to our understanding of gas-liquid interactions; however, such an average scattering trajectory has proved problematic to determine using MD. There are significant variances in surface retention times and trajectory times of flight (TOF) over a distribution of trajectories, which results in difficulty describing an average scattering trajectory relative to time.[3] We find that it is possible to describe an average scattering trajectory by means other than time change. Each scattering trajectory can be described by three steps, which we call the incident step, the surface step, and the scattering step. A diagram of these steps is shown below in figure 2-1.

Figure 2-1. Diagram of trajectory steps

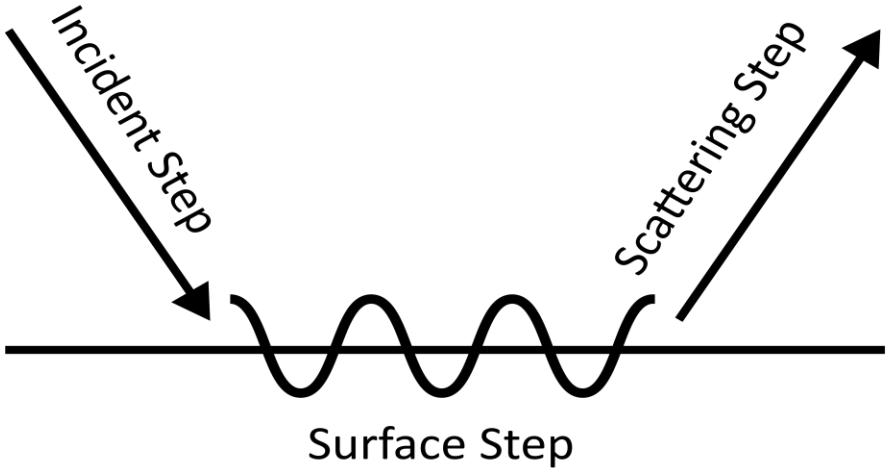

Trajectories begin with the incident step as the gas species is directed at the surface with fixed incident energy. Over the course of this step there should be little change in the energy of the incident species until it reaches the potential of the liquid surface, although there is some possibility of interaction with vapor-phase surface molecules as our liquid model includes vapor pressure effects. During the surface step the gas species undergoes one or more collisions with liquid phase molecules. The time length of the surface step varies considerably across trajectories and is directly proportional to the number of collisions between the gas species and the liquid. During the scattering step, the gas leaves the liquid surface by either the inelastic scattering (IS) channel or trapping desorption (TD) channel based on the number of collisions it has undergone with the surface as described above.[14] Once the gas has escaped the long-range attractive potential of the surface we expect it to experience little energy change until reaching the detector; although there is also a chance of interactions with vapor-

phase surface molecules during this step. In contrast, we expect the gas species to undergo continuous energy change during the surface step of its trajectory as it undergoes collisions with liquid molecules. We therefore expect the gas species to have a wide range of energies while in contact with the liquid surface and remain at a relatively constant energy when outside the interactive radius of the liquid surface. We propose that an average scattering trajectory is best represented by different functions describing each of these steps independently.

We are primarily interested in examining the surface and scattering steps of our trajectories, as the incident step has been well described and is of little relative interest to us. These steps should be separable by the position of the gas species in the direction normal to the surface. Once the gas species has reached a position normal to the surface that places it outside the radius of the long-range attractive component of the surface potential it will have transitioned from the surface step to the scattering step. By examining the Gibbs dividing surface of our liquid, we can estimate the average position of our surface in the surface normal coordinate direction. The position of our liquid surface, combined with the known radius of our attractive gas-liquid interaction, enables us to estimate the position in the surface normal direction at which the transition from the surface step to the scattering step should occur on average. Timesteps at which the gas species remains below this plane are counted as part of the surface step distribution. For this distribution, we record the translational and rotational energy of our gas species every recording timestep. We expect the population of energies to be consistent with a Maxwell-Boltzmann distribution about the surface temperature if the gas species has

undergone sufficient collisions with the surface to thermalize to the surface temperature.[11, 13-14, 20, 23, 26] The scattering step should result in the gas species remaining at the energy with which it escaped the surface potential, unless it interacts with vapor-phase molecules subsequent to scattering from the surface. As we know the gas species must be moving away from the surface during the scattering step, we examine this step by comparing our gas species energy to its position normal to the surface by calculating the average translational and rotational energy of our gas relative to its position normal to the surface. We expect this will allow us to observe the energy change of the gas as it transitions from the surface step to the scattering step, i.e. desorbs from the surface. Additionally, this method should allow us to observe the effects of vapor pressure on the scattering step, as any energy change in our gas species after reaching a position beyond the cutoff radius of the surface potential must result from interactions with vapor-phase molecules.

While considerable evidence has been shown to support the hypothesis that gasses scatter from liquids by two distinct channels, the IS channel has generally been better described than the TD channel.[3, 11, 14, 26] We find the assumption that the final energies of species scattered by the TD channel should be thermalized to the surface temperature troubling, as this would indicate the gas species undergoes no change in energy as it leaves the liquid surface. Surface absorption and desorption are known to have associated enthalpy changes, which we would expect to affect our gas as it absorbs and desorbs from the surface. While there is typically no activation energy for physisorption, desorption from a surface requires overcoming the intermolecular forces binding the gas

species to the surface, which manifests as the activation energy of desorption.[32] The enthalpy of desorption should equal the activation energy of desorption less the energy lost by the gas species to the attractive surface potential while desorbing from the surface. We hope our average trajectory analysis method will allow us to both observe this enthalpy change and estimate its value.

Carbon dioxide was chosen as the initial incident gas for study for several reasons. In terms of pure physical chemistry, CO_2 is a non-dipolar linear triatomic molecule and should be a model comparable with other non-dipolar linear gases. Furthermore, prior efforts by our group had focused on the rotational relaxation of supercritical carbon dioxide[33] which has some similarities to the present work on gas-liquid scattering. Additionally, CO_2 is the second most important greenhouse gas after water vapor, thus making CO_2 studies important to environmental research.[6, 8] Studies involving atmospheric chemistry commonly involve CO_2, making this study relevant to atmospheric research based on the atmospheric interactions of CO_2 and water droplets.[34] There also have been several previous studies performed on CO_2 scattering from liquid surfaces, [13, 15, 23, 27, 35] thus allowing comparison between our present models and experimental results.

Liquid indium was chosen for this study for several reasons. Prior work by our group had used a Lennard-Jones model of liquid indium as a liquid[20] that was in reasonable agreement with experimental work on liquid metal surface scattering.[12, 31] Indium also has a finite vapor pressure, which allows us to determine how the presence of additional gas particles complicates scattering events. From a computational standpoint,

a simple Lennard-Jones system is relatively inexpensive to model, and in the case of liquid metals, reasonably accurate, although others have shown that the resulting surface is rougher than what would be found in the actual system.[31] Additionally, liquid indium has been experimentally shown to have little charge distribution about its surface, thus allowing the exclusion of electrostatic potentials that carry significant computational cost.[36] Getting statistically significant data here means that thousands of trajectories need to be run, and thus the low computational cost allows us to perform these studies in a timely fashion. Finally, our results should be generalizable to the case of the prototypical Lennard-Jones liquid by the principle of corresponding states, allowing comparison to numerous studies involving Lennard-Jones liquids.

Previous surface scattering studies undertaken by our group[20] and others[11, 13-15] have indicated that the most important variables to surface scattering are the incident beam energy, the incident beam angle, and the surface temperature. We examine our system over a range of initial conditions for each of these variables. In order to determine the effect of each variable, we hold two of these initial conditions constant while varying the third, thus enabling us to examine the effect of each variable independently from the others.

This chapter will present the methods used to simulate CO_2 scattering from a liquid indium surface. The results section will detail the effects of varying the incident CO_2 translational energy, incidence angle, and liquid surface temperature. Conclusions and possibilities for future work will then be presented.

II. Computational Methods

All simulations were performed using the DL_POLY code version 2.14,[37] with in-house modifications to support surface scattering and analysis of scattering results. The liquid indium surface used was modeled using a Lennard-Jones potential. The interactions of all species were described by equation 1:

$$V_{LJ} = 4\varepsilon[\left(\frac{\sigma}{r}\right)^{12} - \left(\frac{\sigma}{r}\right)^{6}] \quad (1)$$

Lennard Jones parameters were taken from literature sources for the In, C and O atoms.[38] Standard combination rules were applied in order to determine the C-In and O-In interaction parameters. The self-interaction ε and *r* parameters for C (0.233kJ/mol, 2.757Å), and O (0.669kJ/mol, 3.033Å) have substantially lower force constants than the self-interaction parameters of In (5.04kJ/mol, 2.81Å). Our Lennard Jones cutoff radius (7.02Å) was more than double the Lennard-Jones radius of any species pair.

Our liquid consisted of 864 indium atoms. These were initially pressurized and thermalized using the Nòse-Hoover thermostat/barostat at 1atm under cubic periodic boundary conditions for 10000 timesteps of exactly 6.7fs, integrated by the Verlet leapfrog algorithm under constant number pressure temperature (NPT) setting. The resulting simulation box was then allowed to expand to 50Å in the +z and –z directions, resulting in a simulation box of 50Å by 50Å by 100Å, with the liquid's center-of-mass centered at the origin. Subsequent to this expansion orthogonal periodic boundary

conditions were applied in all simulations. The expansion of the simulation cell resulted in the formation of surfaces with normal directions in the +z and –z directions. An additional simulation was run under constant number volume energy (NVE) to allow these surfaces to thermally equilibrate. The formation of surfaces resulted in the system cooling through both the introduction of surface tension and the vaporization of liquid-phase atoms. Subsequent to this equilibration, we ran an additional equilibration under constant number volume temperature (NVT) setting to further equilibrate our surface at its new temperature. Equilibrated liquid slabs were generated at 436K, 459K, 511K, and 560K. Snapshots of these surfaces were then taken every 1000 time steps after equilibration, creating multiple unique surfaces for use in scattering experiments. There were 92 separate surface snapshots used at each temperature. These methods were used by Dr. Tamas Szabo to generate the surfaces we use in this study during his dissertation work.[20] All of the simulations performed to generate these liquid surfaces were performed by him.

For each incident trajectory the center-of-mass of CO_2 was placed at 48Å in the +z direction over the average position of the liquid surface. The center-of-mass was given random x and y coordinates within the simulation box, and the CO_2 molecule was subsequently given a random orientation in relation to the surface by generating two random Euler angles and calculating the positions of each atom using the Euler rigid body relations for a linear body. In the event that the CO_2 molecule was within 3.5Å of a vapor-phase indium atom, it was given a new random position and orientation until it was at least 3.5Å from the position of any indium atoms. We performed this step to avoid

initially placing our gas species atoms within the repulsive radius of any gas-phase In atoms.

The vibrational degrees of freedom were frozen in the CO_2 molecule for all computations. We froze the vibrational degrees of freedom in order to isolate the effects of surface scattering on the translational and rotational degrees of freedom, as well as to simplify the separation of the internal energies of our CO_2 molecule. The energy of the lowest energy $v_0 \rightarrow v_1$ vibrational mode of CO_2 is approximately 46 kJ/mol, which would likely prove prohibitive to vibrational excitation under our initial conditions in the actual system. Several experimental scattering studies have also observed lower than expected vibrational energy in scattering CO_2 molecules even when CO_2 was given sufficient energy to excite its vibrational modes, giving further indication that vibrational effects are likely to be negligible for our range of initial conditions[15, 35].

At the start of each scattering trajectory, CO_2 was directed at the liquid surface at a fixed incident translational energy and incidence angle in the xz plane. The CO_2 molecule was sent to the surface with zero initial rotational energy in all trajectories performed. All runs were performed using the Verlet leapfrog algorithm at constant energy (constant number volume energy (NVE), i.e. microcanonical ensemble) with a timestep of exactly 0.6 fs. Each trajectory was run until the CO_2 molecule either scattered from the surface and reached an exit plane set at 48Å in the +z direction above the liquid surface, or until 200000 timesteps had passed. For each set of initial conditions, 2300 individual trajectories were taken, which resulted in exactly 25 trajectories scattered from each surface snapshot. After each trajectory, the translational

(center-of-mass) motion was separated from the rotational motion and the translational, rotational, and total kinetic energy were calculated and stored for subsequent analysis. A new surface snapshot was then loaded, and the CO_2 molecule was reset to a new position and orientation and subsequently directed at the new surface to begin a new trajectory.

In order to perform our average trajectory analysis, we must first separate each of our trajectories into independent steps. Additionally, we need to determine whether each trajectory has left the surface by the IS or TD scattering channel in order to independently analyze each scattering channel. Common methods for separating these channels are potentially problematic as discussed above. We posit that a better method for separating the IS and TD channel components of our trajectory distribution is to separate them based on their surface retention time (SRT). Insomuch as the channel by which our gas species scatters from the surface will be determined by the number of collisions our gas undergoes with the liquid, and this number of collisions is directly proportional to the SRT, we feel that this should be a good metric for separating the component channel distributions. While it is experimentally problematic to determine an exact SRT for any given trajectory, it is trivial to determine the SRT for any trajectory using MD.

In order to calculate our average gas scattering trajectory, as well as to separate the two scattering channels, we periodically record our gas species' translational and rotational energy and the z-coordinate of our gas species' center-of-mass position throughout each trajectory. We consider our gas species to have collided with the surface during the timestep in which its z velocity first changes direction from –z to +z. As we are focused on determining the average trajectory for species that scatter via the TD

channel, we wait 3000 timesteps after this initial collision to begin recording in order to avoid recording the energies of species in the incident step of their trajectory and the energies of species scattering via the IS channel. Subsequent to this initial delay, we record the energy of each of our translational degrees of freedom, the total rotational energy, and the z position of the center-of-mass for our gas species every 10 timesteps for the remainder of the trajectory. Subsequent to the conclusion of each trajectory we record the total number of timesteps during which our gas species was considered to be on the surface. We determined a cutoff height in the z direction below which our gas is considered to be on the surface based on the Gibbs dividing surface of our liquid. If our gas species was at a z position within one Lennard-Jones interactive radius of the midpoint of the asymptotic portion of our Gibbs surface, rounded to the nearest integer for programming convenience, during any recording timestep it was considered to be on the surface for that timestep. By this metric we consider our gas species to be on the surface if its center-of-mass position in the +z direction is less than or equal to 19Å, 20Å, 22Å, and 25Å with respect to the 436K, 459K, 511K, and 560K surfaces.

We use several techniques to analyze the recorded trajectory data in order to determine the average trajectory for the TD channel distribution and separate the final distribution of trajectories into its TD and IS channel components. We first look at the number of timesteps our gas species was retained on the surface for each trajectory. Gas species that had left the surface prior to the end of our 3000 timestep delay were considered to have scattered by the IS channel and were recorded as part of its distribution. The literature has given indication that there should be a substantial

decrease in surface retention time between the IS and TD distributions.[11, 13-14] Plotting a histogram of our surface time distributions should enable us to determine the point at which this decrease occurs, and therefore estimate a cutoff time separating our IS and TD channel distributions. For our simulations, this decrease typically occurred after 1000 recording timesteps, which is the equivalent of 10000 actual timesteps of our simulation. Any trajectory with a SRT shorter than 1000 recording timesteps was thus considered part of the IS channel distribution, while any trajectory with a longer SRT was considered to be part of the TD channel distribution. Any trajectory that failed to reach the exit plane prior to the end of our simulation time was considered trapped and not recorded as part of either distribution. These trajectories were discarded to avoid considering species remaining on the surface as part of our scattering distributions.

Subsequent to separating the TD and IS channel components of our trajectory distributions by their SRT we attempt to calculate an average trajectory for gas species scattering via the TD channel. As previously discussed, we consider the surface step and the scattering step separately in order to determine this average trajectory. We analyze the surface step by considering the total distribution of recorded energies at which the center-of-mass position of our gas species was at or below the +z direction cutoff for the surface, as discussed above, for all trajectories in the TD channel distribution. We create histograms for the translational and rotational energies of this distribution by binning each energy distribution from 0.5kJ/mol to 30kJ/mol with a 0.5kJ/mol step size. We subsequently divide the number of energies within each bin range by the total number of recorded energies to create a percentage bin occupancy histogram. If our gas species has

thermalized to the surface temperature during the surface step, we would expect the translational energy histogram distribution to conform to a Maxwell-Boltzmann distribution about the surface temperature (T_s), described by equation 2.

$$f_E(E) = 2\sqrt{\frac{E}{\pi}}\left(\frac{1}{k_B T}\right)^{3/2} e^{-E/k_B T} \tag{2}$$

In order to determine the average trajectory of our scattering step, we first need to determine the z-coordinate of the xy plane above which our gas species has moved beyond the surface potential radius, and therefore transitioned to the scattering step. In order to determine this coordinate, we examine the Gibbs dividing surface and the known potential cutoff radius, as discussed above, as well as our average trajectory positions in the z-coordinate direction. In order to analyze the scattering step of our gas species trajectories, we divide our simulation box into 0.5Å segments from 1Å to 48Å in our +z-coordinate direction. Each of these segments can be described as being bounded by two xy planes separated by 0.5Å in the z direction. We consider our gas species' to be within a given z segment if the z-coordinate of the gas species center-of-mass is between the xy plane's bounding the segment, with the lower planes z position being inclusive. We calculate the average energies of our gas species over these z segments by averaging the recorded energies of our gas at each recording timestep its center-of-mass z position was within a given segment. Thus, the average energy of the 1Å z segment represents the average energy of our species when its center-of-mass z-coordinate position was between 1Å and 1.5Å, etc. By plotting the number of steps our species was within each z segment against the segment's position we can determine the most probable position in the z

direction of our gas species, which we expect to occur near the midpoint of our Gibbs dividing surface. Additionally, we should be able to estimate the maximum depth our gas species penetrates the liquid surface by locating the point at which this population curve decays. We should also be able to determine the average position at which our gas leaves the surface from this plot. Our gas species should remain at relatively constant energy after leaving the surface, and therefore we expect to observe a relatively constant number of timesteps at each z segment above the surface cutoff. Thus, we should be able to determine when our species has left the surface by locating the linear portion of this plot. Finally, by averaging all of the individual energy averages for each z segment over all of our trajectories, we should be able to determine an average trajectory for our scattering step with respect to z-coordinate position, allowing us to observe the average energy change of our gas species as it scatters from the surface.

III. Results and Discussion

1.) Varying Incident Energy Results

In order to determine the effects of liquid surface scattering on the translational and rotational energies of CO_2 molecules, we first varied the incident molecule's initial energy. Simulations were performed using the 436 K liquid surface at a 55^0 incidence angle. The CO_2 molecule was directed at the liquid surface at fixed initial translational

energies of 50kJ/mol, 25kJ/mol, 12.5kJ/mol, and 6.25kJ/mol. The final translational and rotational energies of the scattering CO_2 molecule were then separated by removing the center-of-mass translational energy from the total energy of the CO_2 molecule, leaving only the rotational energy. These energy distributions were then separated into their IS and TD channel components by the methods discussed above. Average values for these final energies are displayed below in table 2-1.

Table 2-1. Average final CO_2 translational and rotational energy values, 436 K liquid In surface, 55^0 incidence angle, IS and TD channel distributions.

Incident Energy, kJ/mol	Average IS Translation Energy, kJ/mol	Average TD Translational Energy, kJ/mol	Average IS Rotational Energy, kJ/mol	Average TD Rotational Energy, kJ/mol
50 kJ/mol	**15.60±0.25**	**7.9±0.24**	**7.46±0.18**	**3.5±0.15**
25 kJ/mol	**10.34±0.18**	**8.1±0.18**	**4.49±0.12**	**3.53±0.12**
12.5 kJ/mol	**9.06±0.17**	**8.21±0.17**	**3.64±0.1**	**3.7±0.12**
6.25 kJ/mol	**7.82±0.15**	**8.29±0.17**	**3.22±.09**	**3.66±0.12**

We observe increasing average translational and rotational energy with respect to increasing incident energy for the IS channel distributions, a result which agrees well with the two channel theory and prior work by both our group[20] and others.[13-15, 27, 31] Our TD channel distribution translational energy averages are within 5% of one another despite an eightfold increase in energy from our lowest to our highest incident energy, showing that species scattering via the TD channel are unaffected by incident energy change. The TD channel rotational energy averages are similarly within 6% of one another, giving further indication that this distribution is unaffected by incident energy change. We take the relative closeness of our average energy values characterizing the TD channel distributions, coupled with the correlation between increasing incident

energy and increasing average final energy in our IS channel distribution, as evidence that our IS and TD components have been reasonably separated by their SRT.

The average energy characterizing the TD channel translational energy distribution is significantly higher than the average translational energy calculated from the equipartition theorem,

$$E = 3/2k_BT \quad (3)$$

Specifically, the average translation energy we find for the TD channel distribution is 8.2kJ /mol, which is approximately 40% higher than the average value calculated from the equipartition theorem at 436K, which is 5.43kJ/mol. By contrast, the rotational energy averages we find for our TD channel distributions are very similar to the average energy calculated from the equipartition theorem for two degrees of freedom,

$$E = k_BT \quad (4)$$

We find the average characterizing our TD channel rotational energy to be 3.59kJ/mol, which agrees well with the value calculated from the equipartition theorem at 436K, which is 3.62kJ/mol.

Our results at 6.25kJ/mol incident energy are of particular interest, as the scattered CO_2 molecule emerges with an average translational energy above both its incident energy and the average surface thermal energy in both the IS and TD channel distributions. This result has previously been observed at similar (6kJ/mol) incident energy in an experimental study of argon scattering from liquid indium by Tribe et al.[31]

This indicates to us that species scattered via the TD channel do not necessarily leave the surface at an energy characterized by the surface temperature as has been previously hypothesized.[11, 14] We use our average trajectory analysis method for the TD channel distributions as discussed above to discern the cause of this energy increase above the expected value for our average translational energies.

There are several possible explanations for the increase in our TD channel translational energy average compared with the expected value calculated from the equipartition theorem. It is possible our SRT method has not fully separated our IS and TD channel distributions, which could result in an increase in the average energy of the TD channel distribution as the IS channel distribution typically has a higher average energy than does the TD channel distribution. However, this effect would not explain our results at 6.25kJ/mol incident energy as we observe an energy increase above both the incident energy and the average surface thermal energy in both channels. We next consider the possibility that our gas species has not thermalized to the surface temperature prior to desorbing from the surface. We examine the surface step distribution of translational energies, generated as described above, in order to determine the distribution of gas specie's translational energies while our gas is on the liquid surface. These distributions are displayed for each of our incident energies below in figure 2-2, along with a Maxwell-Boltzmann distribution about 436K temperature calculated using equation 2.

Figure 2-2. Percent Histogram Bin Occupancy vs. CO_2 Translational Energy, 436 K liquid temperature, 55^0 incidence angle, Surface Step Distribution, TD channel.

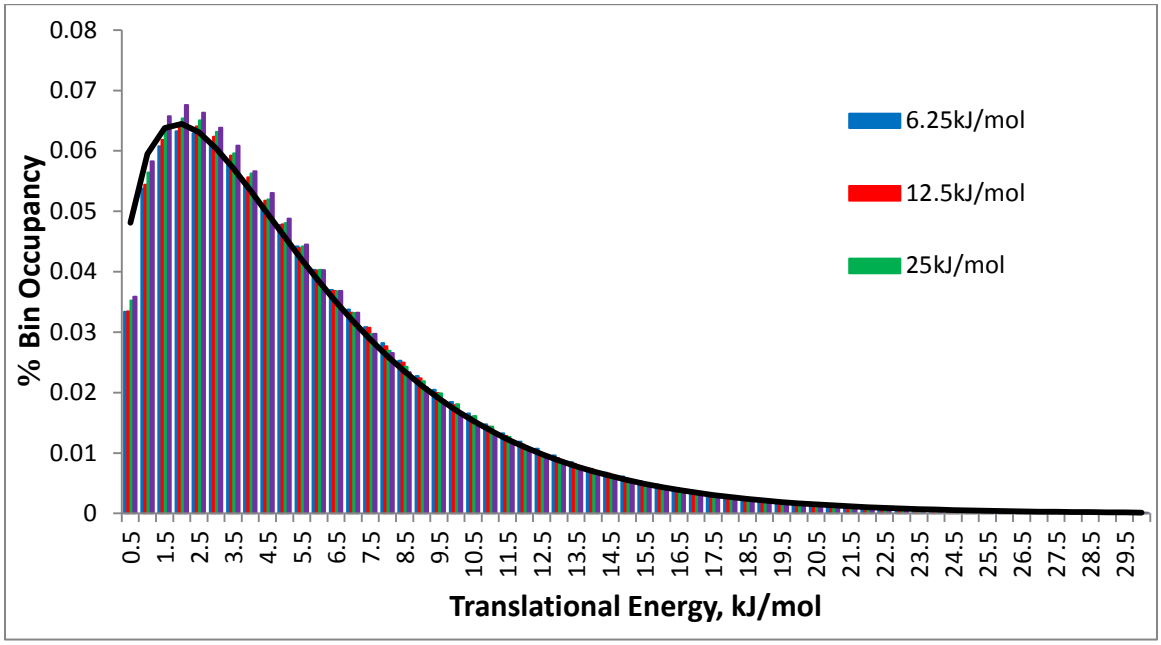

Our surface step translational energy distributions for species scattered via the TD channel clearly conform well to a Maxwell-Boltzmann distribution consistent with our surface temperature for all four of our incident energies as expected, indicating that our gas is well thermalized to the surface temperature prior to desorbing from the surface. We do note a slight increase above expected values from 1.5kJ/mol to 10.5kJ/mol in our bin range. This may be attributable to our recording method, as we continue to record the energies of our gas species as it leaves the surface as part of the surface step distribution until it reaches the distribution cutoff height. Species that leave the surface at low energies will particularly affect the results in this manner, as they will take longer to move past our surface step cutoff plane and therefore have more timesteps of their

scattering step recorded as part of the surface step distribution. Our calculated Maxwell-Boltzmann distribution at 436K temperature fits our surface step energy distributions well, with R^2 values of 0.987, 0.988, 0.991, and 0.990 for our 6.25kJ/mol, 12.5kJ/mol, 25kJ/mol, and 50kJ/mol incident energy surface step distributions, respectively. Our average translational and rotational energies for the surface step also agree well with the expected values calculated from the equipartition theorem as shown in Table 2, giving further evidence that our gas species is well thermalized to the surface temperature during the surface step of its trajectories.

Table 2-2. Average CO_2 translational and rotational energy values, 436 K liquid In surface, 55^0 incidence angle, TD channel, surface step distribution.

Incident Energy, kJ/mol	Average TD Translation Energy, kJ/mol	Expected Translational Energy, kJ/mol	Average TD Rotational Energy, kJ/mol	Expected Rotational Energy, kJ/mol
50 kJ/mol	**5.38±0.20**	**5.43**	**3.64±0.10**	**3.62**
25 kJ/mol	**5.49±0.16**	**5.43**	**3.67±0.09**	**3.62**
12.5 kJ/mol	**5.61±0.12**	**5.43**	**3.78±0.11**	**3.62**
6.25 kJ/mol	**5.68±0.11**	**5.43**	**3.77±0.1**	**3.62**

There remain two possible explanations for the energy increase we observe in our TD channel translational energy distributions. As discussed above, it is likely that the enthalpy of desorption (H_{Des}) will have some effect on our gas species as it leaves the liquid surface via the TD channel. Gas desorption is typically an endothermic process with respect to the gas,[39] making it likely that our gas will gain energy above the average thermal energy of the surface as it desorbs. The inclusion of vapor pressure effects in our study could also lead to an increase in the translational energy of our gas species. While our gas species may experience an energy change resulting from direct collisions with

gas-phase indium atoms, it is more likely the long-range attractive potential of vapor-phase specie's could yield an overall increase in our gas species energy, as its radius is significantly larger than the short range repulsive interaction radius. Indium atoms that vaporize from the surface typically remain above the surface potential cutoff height, as any vapor-phase atoms that enter the surface potential are likely to resorb to the surface. The density of vapor-phase indium atoms increases moving away from the surface, which may result in an attractive potential above the surface in the +z direction which could accelerate our gas species as it leaves the surface. We analyze the scattering step component of our TD channel distribution in order to determine if either or both of these effects are responsible for our observed translational energy increase above the expected value.

In order to examine the scattering step, we first need to determine the z position above which our gas species has left the surface potential. We estimate this cutoff to be 19Å from our Gibbs dividing surface as discussed above. We additionally examine the total number of timesteps our gas species center-of-mass within each z segment of our simulation box in order to get a clearer picture of our surface. A plot of the percent timestep occupancy at each z segment position is shown below in figure 2-3.

While the overall shape of these distributions agree well across our incident energy range, we see a substantial difference in the maximum peak height between our two lowest and highest incident energies. This may indicate that we still have some trajectories that scattered via the IS channel in our TD channel distribution.

Figure 2-3. Percent Time Occupancy vs. Gas center-of-mass z-coordinate, 436 K liquid temperature, 55^0 incidence angle, Scattering Step Distribution, TD channel.

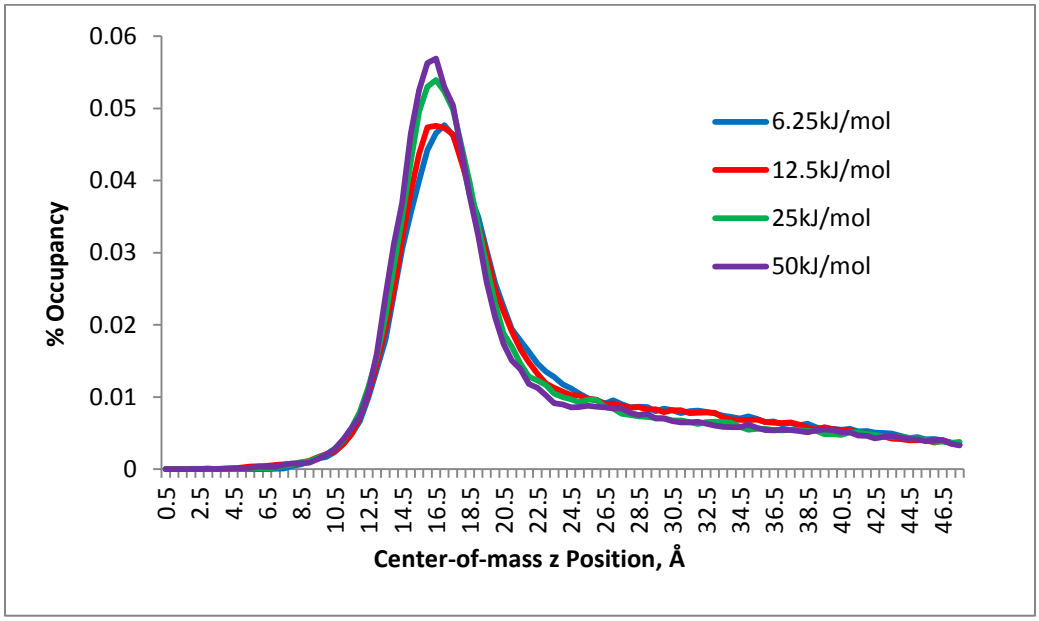

It is reasonable to assume that species that have negligible SRT have scattered via the IS channel and species with long SRT have scattered via the TD channel. However, there is a middle range in which it is problematic to determine through which channel a trajectory has scattered. Species that scatter with low velocities via the IS channel may take substantial time to reach the surface cutoff height and may therefore be counted as part of the TD channel distribution. Our results at lower incident energies are especially susceptible to this effect, as they are more likely to undergo inelastic collisions that result in lower scattering step velocities than our higher incident energies. Indeed, the final translational and rotational energy distributions of the TD and IS channels are very

similar at our two lowest incident energies. We display histograms of the final observed translational energies binned from 1kJ/mol to 30kJ/mol with a 1kJ/mol bin range for both distributions at 6.25kJ/mol incident energy below in figure 2-4 to illustrate this similarity.

Figure 2-4. Percent Histogram Bin Occupancy vs. Final CO_2 Translational Energy, 436 K liquid temperature, 55^0 incident CO_2 angle, IS and TD channel distributions.

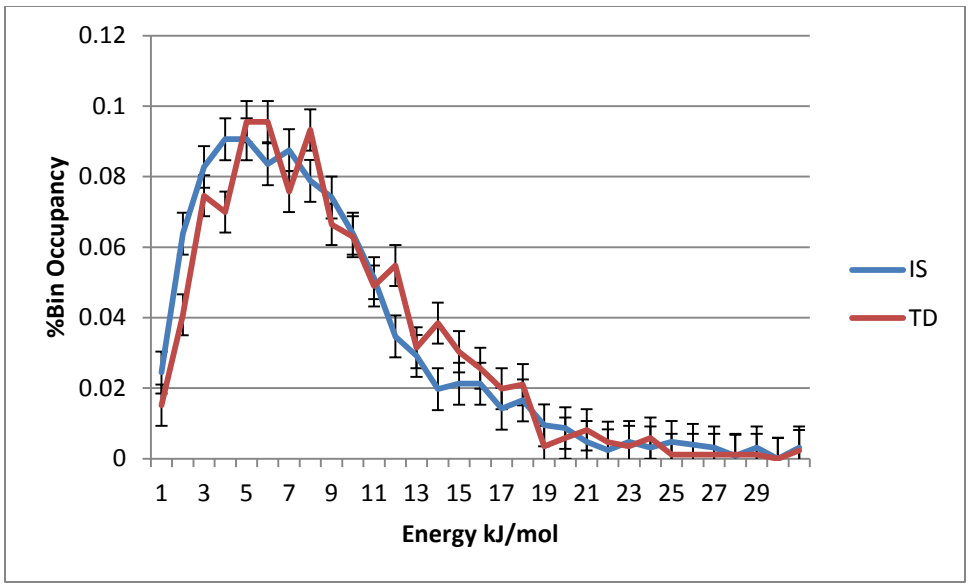

We observe from figure 2-2 that our maximal occupancy state occurs between 16Å and 18Å for all of our incident energies, a result which agrees well with the value of 17Å taken from the midpoint of our Gibbs dividing surface. There is a significant decrease in occupancy below 8.5Å, indicating that our gas species does not typically penetrate the surface below this point. As expected we observe a linear portion of the distributions which relates to the transition between the surface and scattering steps of our trajectories. Our distributions begin to flatten around 22.5Å and are linear by 25Å, which corresponds to the sum of the midpoint of our Gibbs surface and the simulation

cutoff radius of our Lennard-Jones potential. We therefore estimate that any gas species with a center-of-mass position above 25Å in the z-coordinate direction can be said to have transitioned from the surface step to the scattering step of its trajectory. Once our gas species has moved beyond the liquid surface cutoff at 25Å, any observed energy change should be solely attributable to interactions with vaporized surface species.

In order to determine whether the enthalpy of desorption or vapor pressure effects are responsible for the observed increase in translational energy compared with the expected value, we examine the average values of each directional component of our gas species' translational energy and the total rotational energy over each z segment length of our simulation box from 1Å to 48Å. Our previous results have indicated that gasses scattered via the TD channel are unaffected by incident energy, resulting in our energy averages agreeing well for the TD channel distributions at all of our incident energies. We also observe nearly identical distributions of states during the surface step across our incident energy range. These results indicate that the TD channel distributions for each of our incident energies can be considered part of one overall TD channel distribution. In order to maximize our statistics, we take the overall average over each z position segment for the total TD channel distribution regardless of incident energy. For z positions below the surface cutoff, we take the average over each z segment by dividing the total energy of our species at each z segment length over the total number of states within each z segment. While this method provides us with good average energy values for z segments below the surface cutoff, this method underestimates our energy for z segments beyond the surface cutoff. This effect results from the number of states in each z segment

directly correlating with velocity subsequent to our species leaving the surface. Insomuch as species with lower velocities will take longer to reach our exit plane, they will have more states counted at each z segment than gas species with higher velocities, resulting in trajectories with slower velocities being overweighted. In order to avoid overweighting our slower trajectories, we take the average over each z segment for each trajectory individually at z segments above 19Å in position, and then average these individual trajectory averages to obtain our final average energies at each z segment. We display our x, y, and z translational energy averages and our total rotational energy average versus z center-of-mass position below in figure 2-5.

Figure 2-5. Average CO_2 Energy vs. CO_2 center-of-mass z-coordinate, 436 K liquid temperature, 55^0 incidence angle, TD channel.

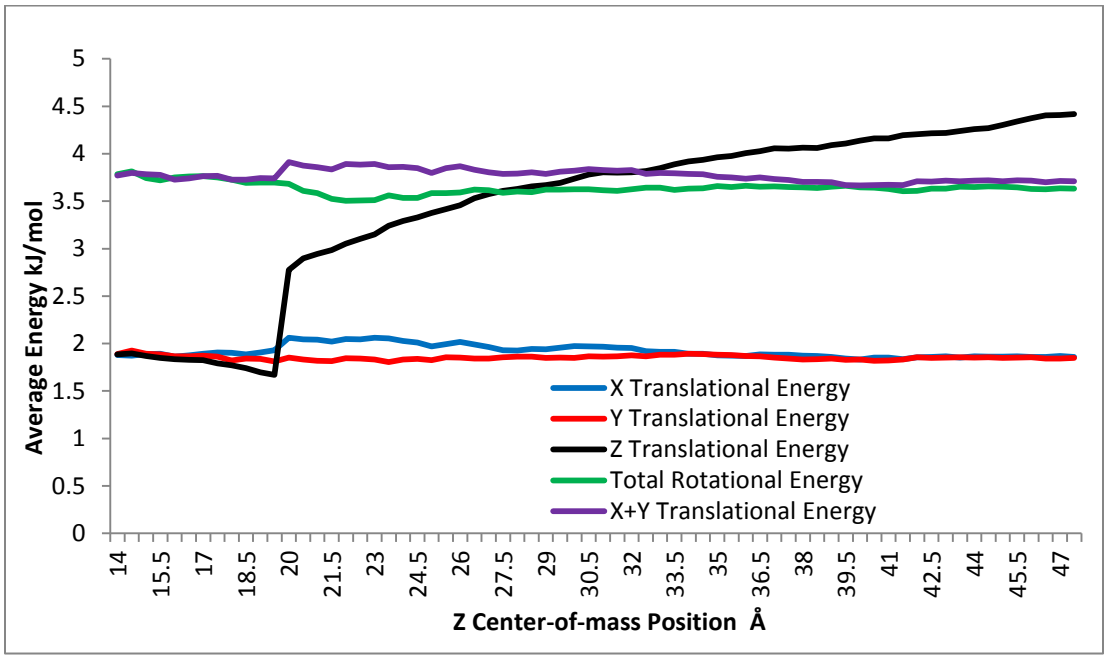

We observe our x and y translational energy components and our total rotational energy remain at relatively constant energy regardless of z-coordinate position. We note a slight increase in our x translational energy value as our gas species moves beyond the surface cutoff. This may indicate that we still have some trajectories scattered via the IS channel in our TD channel distributions, as our incident beam had translational energy only in the x and z directions, and species scattering via the IS channel retain some memory of their incident energies. Our x and y translational energy averages converge above 30Å, and are nearly indistinguishable from one another as the z position approaches the exit plane. Additionally, the sum of our average x and y translational energy averages is very close in value to our average total rotational energy. This result is unsurprising, as the sum of the averages of the x and y translational energies (3.7kJ/mol) and the average total rotational energy (3.63kJ/mol) agree well with the average value predicted by the equipartition theorem for two degrees of freedom at 436K (3.62kJ/mol), calculated by equation 4. We conclude that four of our five total CO_2 degrees of freedom remain well thermalized to the surface temperature subsequent to leaving the surface, and remain relatively unaffected by interactions with gas-phase indium atoms. By contrast, our z translational energy component shows substantial energy change with respect to the z center-of-mass position of our gas species, which we attribute to both the H_{Des} and interactions with vapor-phase indium atoms, as we will discuss in further detail below.

The prototypical Lennard-Jones liquid has been shown to result in a surface potential that is effectively one dimensional where vibrational effects can be ignored.[32]

The average density of the liquid surface remains relatively constant with respect to our x and y coordinate directions, which results in the plus and minus directional components of the long-range attractive potential being approximately equal, on average, with respect to our x and y coordinates. Thus, the long-range attractive potential terms effectively cancel each other out for the x and y coordinate directions, leaving a long-range attractive potential only in the z-coordinate direction. We display a diagram of the long-range attractive forces experienced by our gas species while it remains on the surface below in figure 2-6.

Figure 2-6. Diagram of long-range attractive forces acting on CO_2 while CO_2 is on the liquid surface

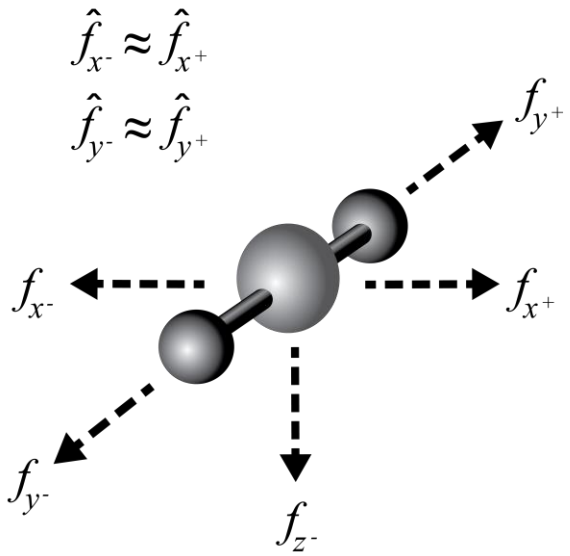

The density of our liquid varies substantially relative to z-coordinate position, resulting in a maximum potential below the average surface position that decays exponentially moving away from the surface in the +z direction. As there is no potential

to overcome in the x or y directions in order to leave the surface, the x and y translational energies are unaffected by the attractive surface potential subsequent to leaving the surface and thus remain thermalized to the surface temperature. The rotational energy is similarly unaffected by the z directional component of the long-range attractive potential, and thus remains thermalized to the surface temperature as well.

By contrast, our gas species must have sufficient translational energy in the +z direction to overcome the surface potential in order to escape from the surface. This results in an activation barrier to the desorption process. If the activation energy of desorption (E_{aDes}) is higher than our gas species' energy loss to the attractive surface potential subsequent to scattering from the surface we expect to observe a net positive energy change in our gas species as it desorbs from the surface. In terms of statistical mechanics, as temperature increases the percentage of energy states at or above E_{aDes} increases and desorption is increasingly favored if the E_{aDes} remains constant. We conclude that the observed increase at positions directly above the surface cutoff is due to the H_{Des}, and estimate its value to be 1.11 kJ/mol, by subtracting our average z translational energy at 21Å (2.94kJ/mol) from the average z translational energy value of the surface step (1.83kJ/mol). We chose this cutoff as we see a substantial increase in z translational energy from 19Å to 21Å, followed by a more gradual increase for the remainder of the average trajectory. We expect our desorbing species to experience a substantial gain in energy in order to overcome the surface potential, and thus we look for a large energy gain over a short distance to estimate the enthalpy of desorption. The value of H_{Des} we obtain by this method is relatively small compared with other phase

change enthalpies. This is unsurprising, as physisorption only occurs by weak intermolecular forces, and is typically only sustainable at temperatures <200K. Reported H_{Des} values in this temperature range are typically on the order of ~5-20kJ/mol.[32] It is therefore unsurprising to observe a small H_{Des} at 436K, as phase-change enthalpies typically decrease with increasing temperature, and our ambient temperature is more than double the normal temperature at which the H_{Des} is commonly experimentally quantified.

We observe a nearly continuous increase in our average z translational energy above the cutoff radius of the surface potential and concluded that this results from interactions with the long-range attractive potential of vaporized indium atoms. As there is no other possible interaction that could account for energy change in our gas species beyond the surface cutoff, we are left with interactions with vapor-phase indium as the only possible explanation of this energy change. As discussed above, these vaporized indium atoms will likely remain above the surface and exhibit an attractive force in the +z direction relative to our gas species as it leaves the surface. We would expect our gas species to eventually move to a position above these vapor-phase indium atoms in the actual system, and therefore experience an attractive force in the negative z direction; however, our simulation box size and the height of our detector cutoff plane preclude this from occurring in our simulations. We estimate the average increase in translational energy resulting from these gas phase interactions to be 1.5kJ/mol, calculated by subtracting the average z translation energy average at 21Å from the average at 47Å.

As a result of this observed translational energy increase, we find it problematic to fit our final observed translational energy distributions to a Maxwell-Boltzmann

distribution, as only two of our translational degrees of freedom remain thermalized to the surface temperature. It may be possible to fit our observed results to a combined 2D/1D Maxwell-Boltzmann distribution, but we have been unable to obtain good agreement between our results and such a distribution at present.

2.) Varying Incidence Angle Results

Our next study involved varying the incidence angle of the CO_2 molecule to determine the effect of incidence angle on our scattered gas species. We first halved the incidence angle to 22.5^0 and scattered CO_2 at all four previously used incident energies from the 436 K indium surface. Average values for all energy distributions are presented in table 2-3 for these trajectories.

Table 2-3. Average CO_2 translational and rotational energy values, 436 K liquid temperature, 22.5^0 incidence angle.

Incident Energy, kJ/mol	Average IS Translation Energy, kJ/mol	Average TD Translational Energy, kJ/mol	Average IS Rotational Energy, kJ/mol	Average TD Rotational Energy, kJ/mol
50 kJ/mol	**13.73±0.23**	**7.69±0.19**	**6.44±0.18**	**3.44±0.12**
25 kJ/mol	**9.91±0.19**	**7.70±0.16**	**4.36±0.12**	**3.62±0.12**
12.5 kJ/mol	**9.01±0.18**	**8.22±0.17**	**3.61±0.11**	**3.88±0.12**
6.25 kJ/mol	**8.22±0.16**	**8.207±0.17**	**3.36±0.10**	**3.95±0.11**

As in our computations at a 55^0 incidence angle, the TD channel distributions show similar average values for both translational and rotational energy. We note that there is a more substantial difference between our two highest and lowest incident energies than in our results at 55^0 incidence angle. This energy difference is possibly

attributable to our SRT method failing to fully separate our trajectories, as was the case in our 55^0 incidence angle study. It is also possible that the limited number of trajectories in the TD channel distributions have made our results more susceptible to statistical variance. The TD channel results also compare well with the average values obtained for the 55^0 incidence angle case, a finding which indicates that incidence angle has a negligible effect on the TD channel distribution. By contrast, we see significant differences in the IS channel average energies and distributions, particularly at higher incident energies. These distributions are displayed for the highest incident energies in figures 2-7 and 2-8.

Figure 2-7. Percent Histogram Bin Occupancy vs. CO_2 Translation Energy, 436 K liquid temperature, 22.5^0 and 55^0 incidence angles, IS channel distributions.

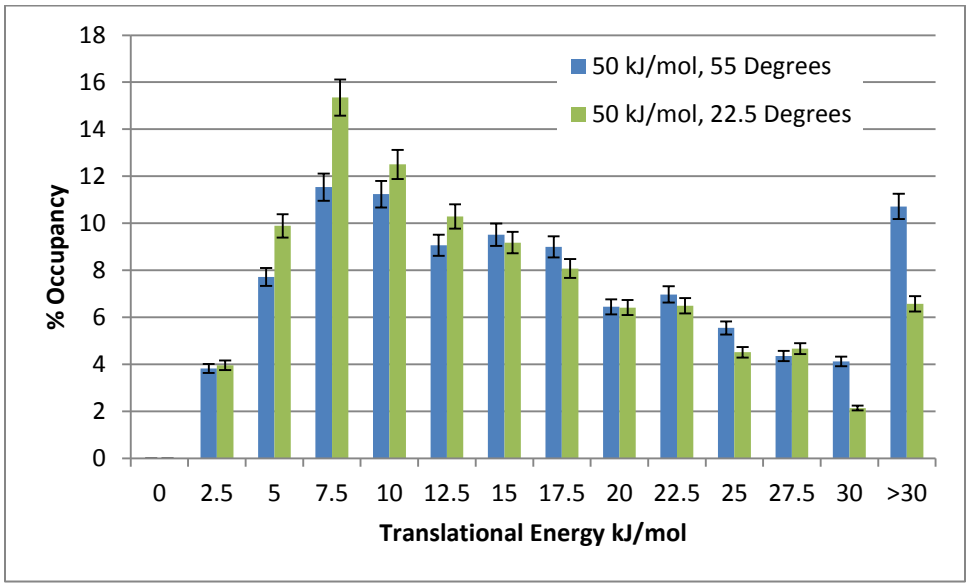

The translational energy distribution displayed in figure 2-7 shows a significant increase in the peaks around 5kJ/mol and 7.5 kJ/mol for the 22.5^0 incidence angle

scattering distribution, and a large decrease in the peak for values greater than 30kJ/mol compared with the 55^0 case. Given that far more of the incident energy is directed perpendicular to the surface in the 22.5^0 case (approximately 92% for the 22.5^0 case versus 57% for the 55^0 case), it is reasonable that the incident CO_2 molecule will donate more energy to the surface and scatter with less translational energy than in the 55^0 case. This presumption is well confirmed by the above results, and agrees well with several studies in the literature.[25, 31, 35]

Figure 2-8. Percent Histogram Bin Occupancy vs. CO_2 Rotational Energy, 436 K liquid temperature, 22.5^0 and 55^0 incidence angles, IS channel distributions.

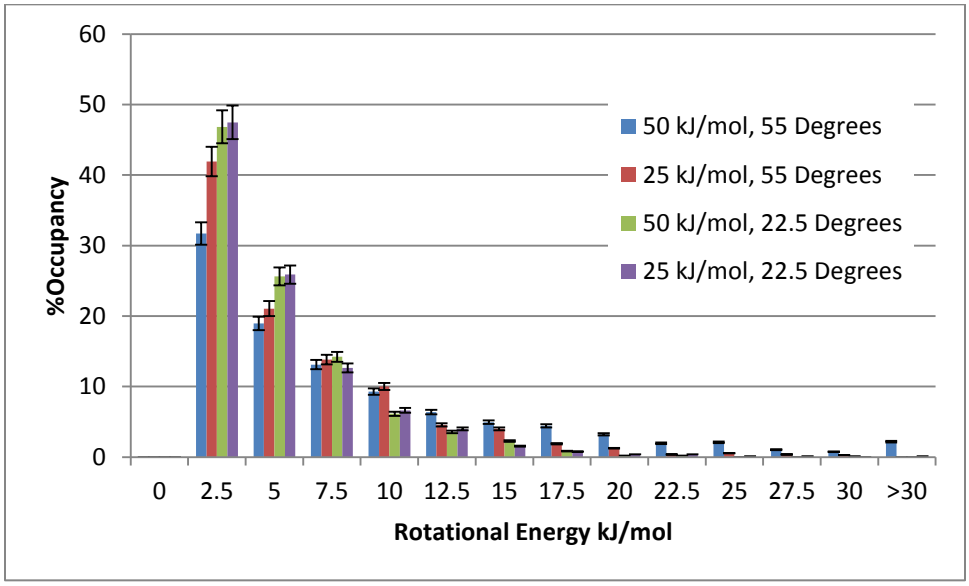

The scattering rotational distribution is narrower in the 22.5^0 incidence angle case, with more species being found at the lower scattering energies and fewer being found at the higher scattering energies than in the 55^0 case. Species scattered via the IS channel do not remain in contact with the surface long enough to become affected by the motion

of the liquid, resulting in their final energies being primarily influenced by the incident energy of the gas species. The initial few collisions between our gas species and the surface result in our gas losing some of its initial translational energy to the surface via inelastic collisions and converting another portion of its initial energy to rotational motion. Given that the initial collisions are the most important factor in determining the energies of species scattering via the IS channel, it is unsurprising to observe a corresponding decrease in rotational energy given the observed translational energy decrease compared to the values observed at 55^0 incidence angle. This assumption is well confirmed by the data as displayed above.

We observe that the IS and TD channel energy values again become increasingly similar as the incident energy approaches the average energy of the liquid surface. We plot histograms of the final translation energy distributions at 6.25kJ/mol incident energy for both the IS and TD channel distributions below in figure 2-9.

Figure 2-9. Percent Histogram Bin Occupancy vs. CO_2 Translation Energy, 436 K liquid temperature, 22.5^0 incidence angle, 6.25kJ/mol incident energy, IS and TD channel

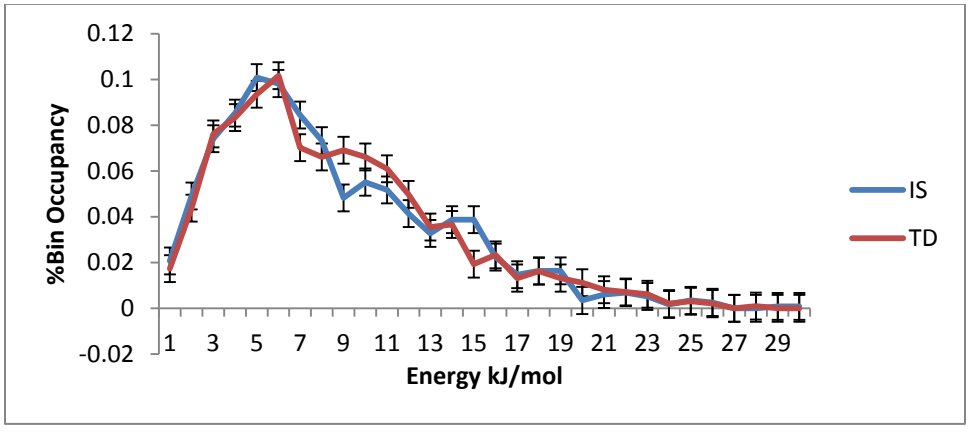

As in our previous study, we observe a very similar distribution of final energies in both channels at 6.25kJ/mol incident energy, giving us further evidence that these scattering channels become increasingly similar as the incident energy approaches the average energy of the liquid surface.

We examine the surface and scattering steps of our TD channel trajectories using the same methods as in our initial study in order to determine the average energy change of our gas species during each of these steps. We plot a histogram of the translational energies of gas species during the surface step of their trajectories below in figure 2-10.

Figure 2-10. Percent Histogram Bin Occupancy vs. CO_2 Translational Energy, 436 K liquid temperature, 22.5^0 incidence angle, Surface Step Distribution, TD channel.

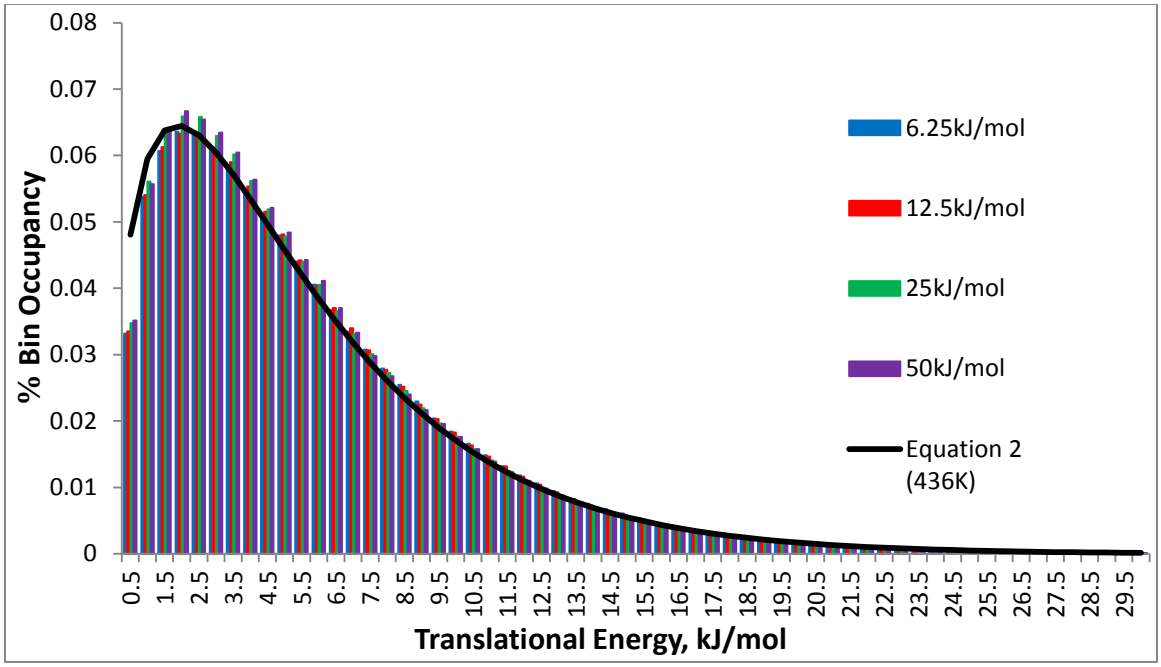

We observe that the surface step translational energy distributions at all of our incident energies conform well to a Maxwell-Boltzmann distribution about our surface temperature, with equation 2 fitting our distributions with R^2 values of 0.987, 0.988, 0.990, and 0.990 with respect to the 6.25kJ/mol, 12.5kJ/mol, 25kJ/mol, and 50kJ/mol incident energies. This result gives further indication that our TD distributions are well thermalized to the surface temperature during the surface step of our trajectories.

In order to observe the energy change in our species during the scattering step of its trajectory we examine the average energy over each z segment position as in our previous study. As the 436K temperature surfaces we use in this study are the same as those used in our study at 55^0 incidence angle, the surface characteristics should remain unchanged and our previous estimates for the cutoff heights should remain valid. We display a plot of our average energy at each z segment below in figure 2-11.

We observe that the average energies of four of our CO_2 molecule's degrees of freedom remain relatively constant regardless of z position. The average values of our x and y translational energy sum (3.71kJ/mol) and our total rotational energy (3.63kJ/mol) also agree well with the expected value calculated by equation 4 (3.62kJ/mol) at 436K temperature. We observe a substantial increase in our z translational energy component which we attribute to both the H_{Des} and interactions with vapor-phase indium atoms. We estimate the value of H_{Des} to be 1.01kJ/mol by subtracting the average surface value of our z translational energy from the average energy calculated at 21Å z position. This value of H_{Des} agrees reasonably well with the value estimated from our 55^0 incidence angle study (1.11kJ/mol). We conclude that the energy change beyond this position

results from interactions with vapor-phase indium atoms as described in the previous section. The plot in figure 2-11 is very similar in to the plot in figure 2-5 despite a 50% change in incidence angle, which provides us further indication that species that scatter via the TD channel remain unaffected by changes to their incidence angle.

Figure 2-11. Average CO_2 Energy vs. CO_2 center-of-mass z-coordinate, 436 K liquid temperature, 22.5^0 incidence angle, TD channel.

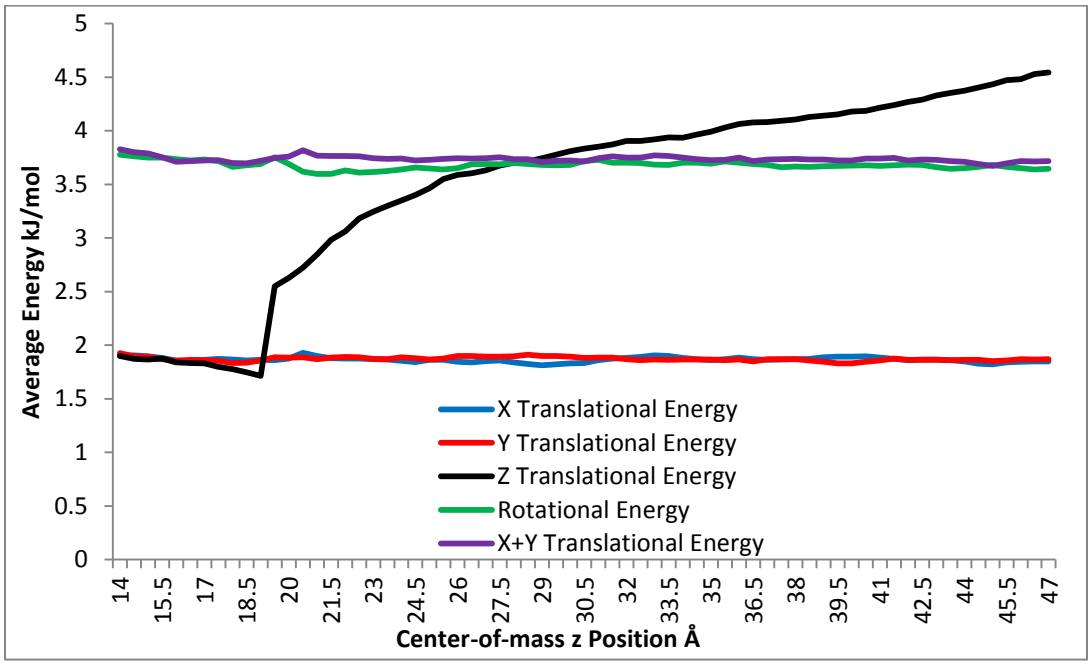

In order to more fully characterize the effects of scattering angle, we performed additional studies at 0^0 (normal) incidence angle. The average energy values for the IS and TD channel distributions at 0^0 incidence angle are displayed below in table 2-4.

Table 2-4. Average CO_2 translational and rotational energy values, 436 K liquid temperature, 0^0 incidence angle.

Incident Energy, kJ/mol	Average IS Translation Energy, kJ/mol	Average TD Translational Energy, kJ/mol	Average IS Rotational Energy, kJ/mol	Average TD Rotational Energy, kJ/mol
50 kJ/mol	**14.19±0.24**	**7.79±0.19**	**6.62±0.18**	**3.43±0.12**
25 kJ/mol	**10.42±0.19**	**8.12±0.17**	**4.47±0.13**	**3.47±0.11**
12.5 kJ/mol	**8.67±0.16**	**8.29±0.17**	**3.89±0.13**	**3.74±0.1**
6.25 kJ/mol	**8.11±0.17**	**8.51±0.17**	**3.53±0.11**	**3.79±0.11**

We again observe that our TD channel average energies agree reasonably well with each other, while our IS channel average energies increase with increasing incident energy. The results obtained at each of our incident energies show agreement within 5% of the average values obtained at 22.5^0 incidence angle for both the IS and TD channel distributions. Insomuch as there is only an 8% difference in the amount of energy directed perpendicular to the liquid surface in the two cases, this result is quite reasonable. This result indicates that the effect of varying the incidence angle decreases as we approach the normal angle to the surface. This trend has been observed in several other studies on gas-liquid scattering, indicating good agreement between our incidence angle results and the expected trends.[3, 14, 18, 31, 40]

We next examine the fraction of trajectories scattered by the TD channel for each of our initial conditions. The principle of microscopic reversibility states that the most favored state for a given process must also be the most favored state for the reverse process. We therefore expect our TD channel occupancy to be highest at initial conditions near the average state with which our gas species desorbs from the surface.

We determine the fraction of states scattered via the TD channel by calculating the fraction of gas species scattered via this channel every 50 trajectories and then averaging these fractions for every group of 50 trajectories, resulting in an average composed of 46 fractions for each set of initial conditions. This method was used over the simpler method of dividing the total number of species scattered via the TD channel by our total number of trajectories as it allows us to estimate the error in our results. The fraction of each set of trajectories scattered by the TD channel for each of our initial conditions is displayed below in table 2-5.

Table 2-5 TD channel fractional occupancy.

Incident Energy, kJ/mol	TD Channel Fraction, 436K 55^0 Incidence Angle	TD Channel Fraction, 436K 22.5^0 Incidence Angle	TD Channel Fraction, 436K 0^0 Incidence Angle
50 kJ/mol	**0.23±0.009**	**0.28±0.01**	**0.29±0.02**
25 kJ/mol	**0.36±0.02**	**0.39±.03**	**0.39±0.03**
12.5 kJ/mol	**0.39±0.03**	**0.44±0.04**	**0.45±0.04**
6.25 kJ/mol	**0.37±0.04**	**0.42±0.03**	**0.45±0.04**

We observe increasing TD channel occupancy with decreasing incidence angle. This result agrees well with other studies in the literature,[3, 14, 24, 31] as well as with the principle of microscopic reversibility. Others have shown angles close to the normal angle are favored for desorption;[3, 14, 24, 31] thus, we would expect absorption to be favored at similar angles. We have previously shown the z component of our translational energy to be substantially higher than the x or y components for species scattered via the TD channel, which gives further indication that angles closer to the surface normal are favored for desorption, and therefore absorption. Our TD channel occupancy increases

slightly from 6.25kJ/mol incident energy to 12.5kJ/mol incident energy, except in the 0^0 incidence angle case where both incident energies have equal occupancy values. The values at our lowest energies are also within the error of one another. We observe a decrease in the TD channel occupancy with increasing incident energy above 12.5kJ/mol, with a significant decline in occupancy occurring at 50kJ/mol incident energy. These results agree well with the trends reported for similar systems in the literature.[19, 25, 35] We estimate the average translational energy of our species subsequent to desorption to be 6.73kJ/mol by adding our estimated H_{Des} (1.11kJ/mol) to the average total translational energy of our species taken from our surface step distribution at 436K (5.62kJ/mol). This estimate attempts to mitigate the effects of vapor-phase interactions on our energy estimate, as these interactions primarily occur beyond the cutoff radius of our surface potential and therefore should not play a significant role in absorption or desorption. This estimate indicates that our most favorable energy for absorption to the surface, and thus scattering via the TD channel, should occur at approximately 6.73kJ/mol. Our results agree well with this estimate, as our maximum TD fraction occurs at the incident energies bounding this estimate. We conclude that scattering via the TD channel is most favored at low incident energies and incidence angles close to the surface normal, a result which agrees well with trends observed in several studies from the literature.[3, 14, 19, 25, 35]

.3.) Varying Surface Temperature Results

All of our previous studies were performed at 436K surface temperature. This temperature is only slightly above the melting point of liquid indium (429K), so we expect the surface at 436K to be relatively smooth with few vapor-phase indium atoms.

In order to determine the effects of temperature on our scattering computations, we performed additional studies on liquid indium equilibrated at temperatures of 459K, 511K, and 560K, with a 55^0 CO_2 incidence angle and the same series of incident energies considered previously. Average scattered energy values calculated for the 459K liquid surface case are displayed below in table 2-6.

Table 2-6. Average CO_2 translational and rotational energy values, 459 K liquid In surface, 55^0 incidence angle.

Incident Energy, kJ/mol	Average IS Translation Energy, kJ/mol	Average TD Translational Energy, kJ/mol	Average IS Rotational Energy, kJ/mol	Average TD Rotational Energy, kJ/mol
50 kJ/mol	**15.87±0.26**	**8.48±0.22**	**7.24±0.19**	**3.80±0.15**
25 kJ/mol	**10.55±0.18**	**8.18±0.19**	**4.65±0.13**	**4.01±0.13**
12.5 kJ/mol	**8.76±.022**	**8.91±0.16**	**3.89±0.1**	**3.89±0.11**
6.25 kJ/mol	**8.07±0.15**	**8.98±0.17**	**3.37±0.09**	**3.82±0.14**

Our average translational energy values for the TD channel distribution at 459K are higher than those obtained for the 436K liquid temperature. This result is reasonable, as we would expect an increase in surface temperature to yield a higher average value for the energies of species scattered via the TD channel. Our IS channel energy averages are also higher than those obtained for the 436K liquid temperature, excepting our results at 12.5kJ/mol incident energy which are slightly lower. As our results for 12.5kJ/mol incident energy at each temperature are within the standard error of one another, this observed decrease is likely not significant. We observe increasing incident energy corresponds to an increase in average final energy for the IS channel distribution, a trend which agrees well with our previous results.

We next examined the surface step of our TD channel trajectories in order to verify that our gas species had thermalized to the surface temperature as we expect in the case of species scattering via the TD channel. We display our surface step translational energy histograms, as well as a Maxwell-Boltzmann energy distribution about 459K calculated using equation 2, below in figure 2-12.

Figure 2-12. Percent Histogram Bin Occupancy vs. CO_2 Translational Energy, 55^0 Incidence angle, 459K temperature, surface step distribution, TD channel

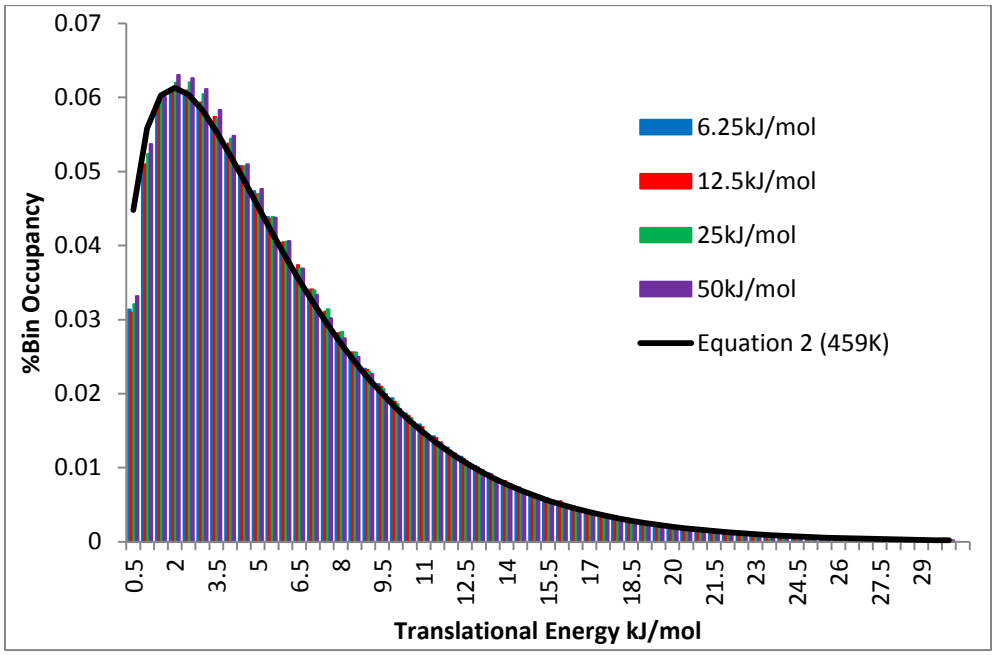

We find the surface step distributions conform well to a Maxwell-Boltzmann distribution about the surface temperature as we observed in our previous results. Our calculated Maxwell-Boltzmann distribution at 459K gives excellent agreement with our results, with R^2 values of 0.98, 0.98, 0.99, and 0.991 with respect to the 6.25kJ/mol, 12.5kJ/mol, 25kJ/mol, and 50kJ/mol incident energies. Furthermore, our average

translation and rotational energies for the surface step distribution (5.77kJ/mol and 3.9kJ/mol, respectively) agree well with the values expected from the equipartition theorem at 459K, which are 5.72kJ/mol and 3.8kJ/mol with respect to the translational and rotational energy. These results indicate that our gas species is well thermalized to the 459K liquid surface temperature during the surface step of its trajectories.

In order to examine the scattering step of our trajectory we first need to determine the average position at which the transition from the surface step to the scattering step occurs for our liquid surface at 459K. We plot the percent occupancy at each z segment in order to determine this transition point, as well as to observe the general characteristics of our surface at 459K. We display this plot below in figure 2-13.

Figure 2-13. Percent Time Occupancy vs. CO_2 center-of-mass z-coordinate, 459K liquid temperature, 55^0 incidence angle, Scattering Step Distribution, TD channel.

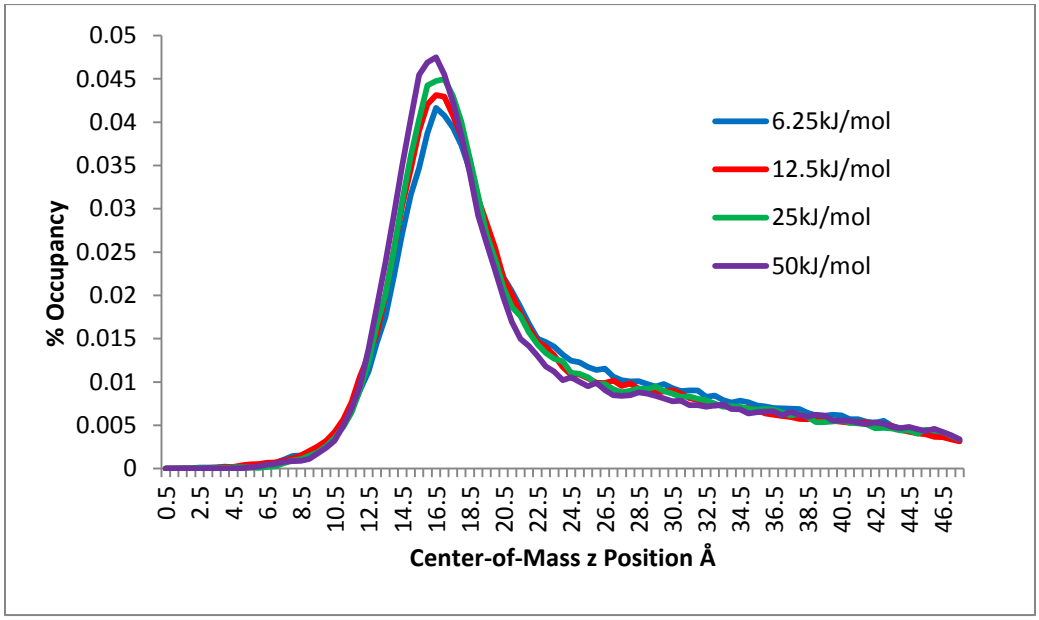

We observe that our distribution is slightly broader at 459K than at 436K, which is unsurprising as our liquid expands in the z direction with increasing temperature. We observe a maximum between 16Å and 18Å at each of our incident energies, which roughly correlates to the midpoint of our Gibbs dividing surface. Our distribution begins to become linear around 22.5Å and is relatively linear by 26Å indicating species above this position are likely to be in the scattering step of their trajectories.

We examine the scattering step of our trajectory in order to determine the energy change in our gas species as it scatters from the surface. We calculate the average translational and rotational energy at each z segment by the same methods used previously to examine this energy change. A plot of our average energies against z segment position is shown below in figure 2-14.

Our x and y translational energies and our total rotational energy remain relatively constant regardless of z position. We note a slight increase in x translational energy as our gas species scatters from the surface which is similar to our results at 436K at 55^0 incidence angle. This observed increase in the x translational energy component could indicate the presence of some trajectories scattered by the IS channel in our TD channel distribution as discussed above. We again see substantial increases to the z translational energy both as the gas leaves the surface and as the gas moves towards the exit plane. We conclude that these energy changes are caused by H_{Des} and interactions with vapor-phase indium atoms, respectively. We estimate the H_{Des} by subtracting our gas's average z translational energy on the surface from our average at 22Å and obtain a value of 1.13kJ/mol, which agrees well with our previous results. The sum of our x and y average

translational energies (3.91kJ/mol) and the total average rotational energy (3.82kJ/mol) also agrees well with the value predicted by the equipartition theorem (3.81kJ/mol), calculated by equation 4. These results give us further indication that our gas species' translational energy in the surface normal direction is the only degree of freedom of our gas species affected by leaving the surface.

Figure 2-14. Average CO_2 Energy vs. CO_2 center-of-mass z-coordinate, 459 K liquid temperature, 55^0 incidence angle, TD channel.

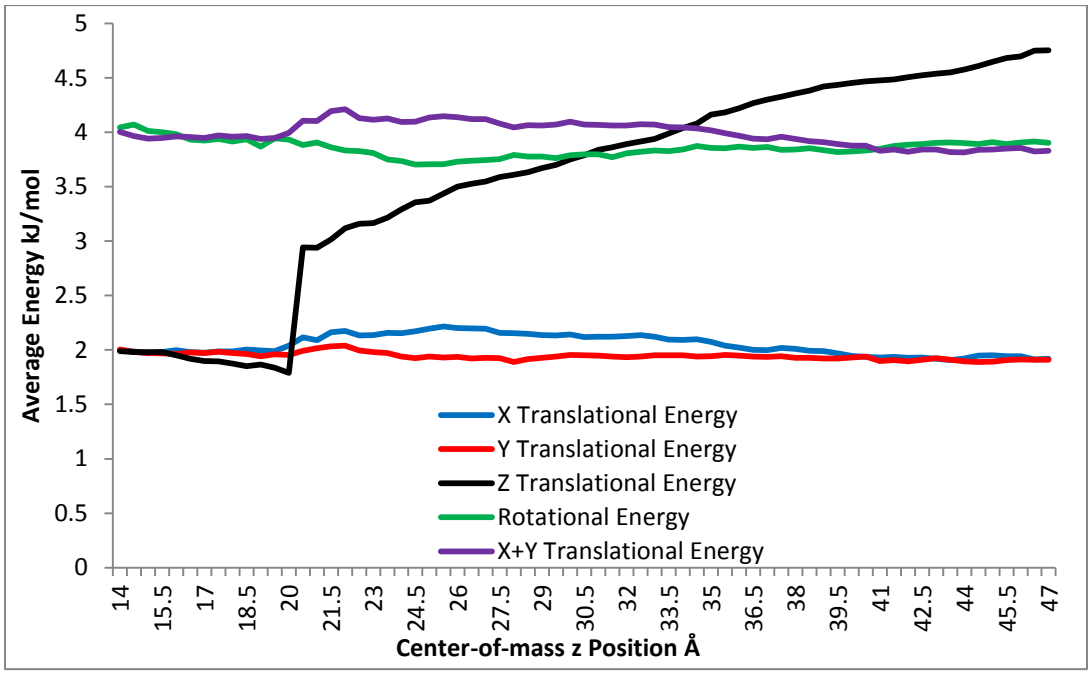

In simulations performed using the 511K liquid temperature we begin to observe a marked increase in the number of vapor-phase indium atoms. This increase is expected to have a significant effect on the scattered CO_2 energy results obtained from surfaces equilibrated at this temperature. The average distribution values at 511K are displayed in table 2-7.

Table 2-7. Average CO_2 translational and rotational energy values, 511K liquid surface, 55^0 incidence angle.

Incident Energy, kJ/mol	Average IS Translation Energy, kJ/mol	Average TD Translational Energy, kJ/mol	Average IS Rotational Energy, kJ/mol	Average TD Rotational Energy, kJ/mol
50 kJ/mol	**15.64±0.34**	**9.24±0.31**	**7.70±0.26**	**4.05±0.22**
25 kJ/mol	**11.5±0.21**	**8.85±0.21**	**5.35±0.15**	**4.31±0.15**
12.5 kJ/mol	**9.83±0.18**	**9.77±0.25**	**4.48±0.13**	**4.45±0.16**
6.25 kJ/mol	**8.54±0.15**	**9.99±0.26**	**3.77±0.10**	**4.45±0.18**

We observe an increase in the average energies of our IS channel distribution compared with our results at 459K and 436K surface temperature. The energies of this channel increase with increasing incident energy, a trend which agrees well with our previous results. Our TD channel energies agree well with one another except for our value at 25kJ/mol incident energy. This difference may be attributable to the limited statistics in the TD channel distribution at this liquid temperature, as fewer gas species scatter via the TD channel at this temperature compared with our lower liquid temperatures.

We examine the population of states at each z segment in order to determine the character of our surface, as well as to determine the threshold for transitions from the surface step to the scattering step for our trajectories. A plot of the occupancy at each z segment is displayed below in figure 2-15.

We observe a broader distribution at 511K compared with our results at 459K, which is unsurprising given the 52K increase in temperature. The most probable z position is found between 12Å and 20Å for all of our incident energies. We observe the linear portion of this plot begins around 23Å, with linearity at around 26Å. We also

observe that there is still relatively little penetration of the surface below 8.5Å. We use the positions of our plot's linear region to estimate our surface cutoff height in order to examine the scattering step of our trajectories.

Figure 2-15. Percent Time Occupancy vs. CO_2 center-of-mass z-coordinate, 511 K liquid temperature, 55^0 incidence angle, TD channel.

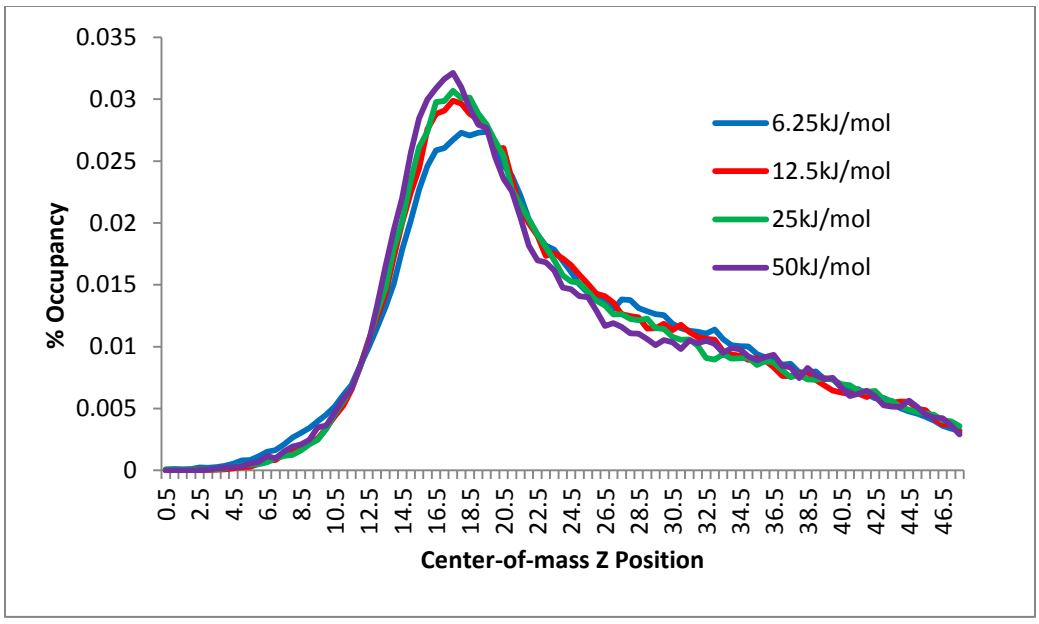

In order to examine the energy change of our gas species over the surface step and scattering step of our trajectories, we plot a histogram of the surface step translational energy distribution below in figure 2-16, and the average translational and rotational energies of our gas species against the center-of-mass z position in figure 2-17.

Figure 2-16. Percent Histogram Bin Occupancy vs. CO2 Translational Energy, 55^0 Incidence angle, 511K temperature, surface step distribution, TD channel

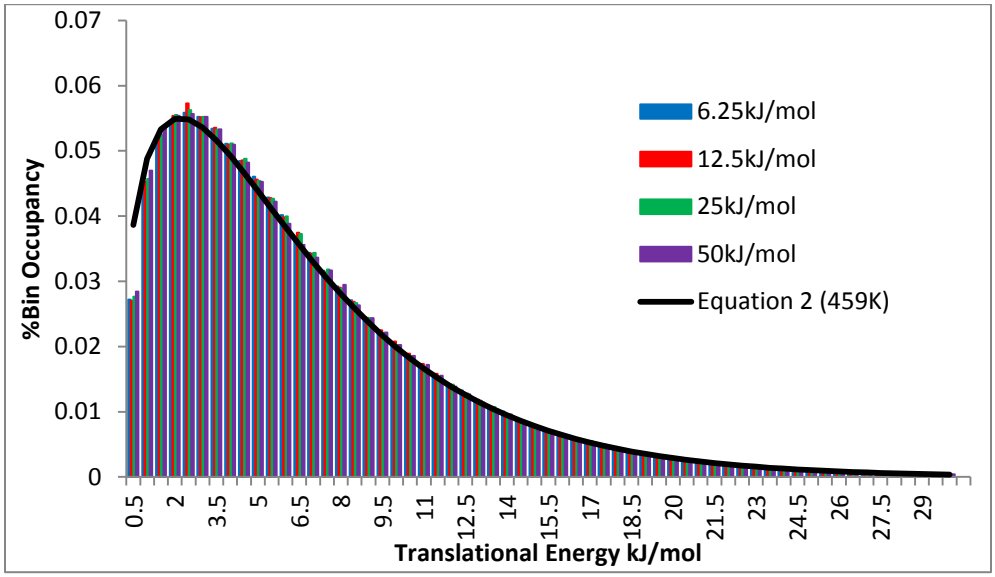

Figure 2-17. Average CO_2 Energy vs. CO_2 center-of-mass z-coordinate, 511K liquid temperature, 55^0 incidence angle, TD channel.

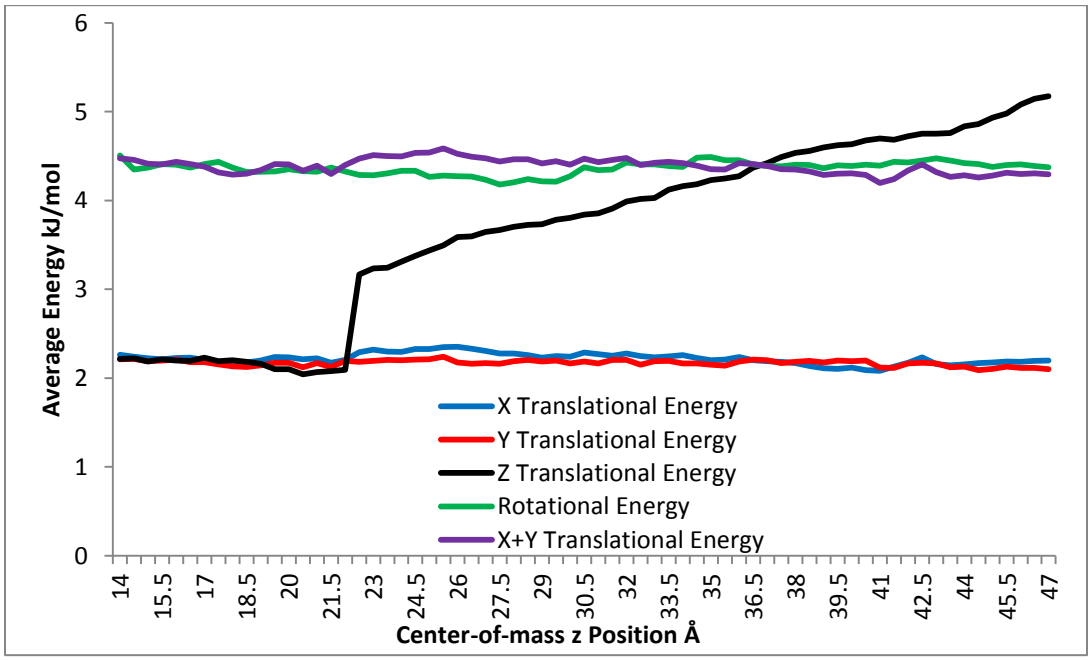

Our surface step distribution conforms well to a Maxwell-Boltzmann distribution about the surface temperature, with our average translational energy (6.49kJ/mol) and rotational energy (4.36kJ/mol) agreeing well with the expected values for translational energy (6.36kJ/mol) and rotational energy (4.24kJ/mol) as calculated by the equipartition theorem at 511K. Analysis of our scattering step distribution determines that our x and y translational energies and total rotational energy remain unaffected leaving the surface. We observe the effect of both H_{Des} and interactions with vapor-phase indium atoms on our z translational motion. We estimate the value of H_{Des} to be 1.02kJ/mol by subtracting our average z translational energy on the surface from our value at 23Å. This estimated value agrees well with our previous estimates, although it is slightly lower than some previous values. It is possible that this variance results from the relatively crude method we use to estimate H_{Des}. We observe that vapor-phase interactions increase our gas species' energy by approximately 2kJ/mol at this temperature, which is an approximately 25% increase compared to our previous final energy values. This result is readily explained by the increase in vapor pressure, and therefore vapor-phase indium atoms, at the 511K surface temperature compared with our lower temperature studies.

The 560 K liquid surface has by far the largest number of gas-phase indium atoms (i.e. the highest vapor pressure) of any of the surfaces we have studied. Given our results at 511K, it is likely that the effect of vapor-phase indium atoms will play a larger role in the overall energy transfer at 560K. The average energy values calculated for scattering from a liquid surface equilibrated at 560 K are displayed in table 2-8.

Table 2-8. Average CO_2 translational and rotational energy values, 560 K liquid In surface, 55^0 incidence angle.

Incident Energy, kJ/mol	Average IS Translation Energy, kJ/mol	Average TD Translational Energy, kJ/mol	Average IS Rotational Energy, kJ/mol	Average TD Rotational Energy, kJ/mol
50 kJ/mol	**16.55±0.49**	**10.05±0.26**	**8.77±0.61**	**4.53±0.18**
25 kJ/mol	**12.09±0.3**	**10.08±0.24**	**6.22±0.45**	**4.76±0.17**
12.5 kJ/mol	**11.01±0.4**	**11.14±0.29**	**5.31±0.31**	**4.94±0.18**
6.25 kJ/mol	**10.07±0.25**	**10.023±0.26**	**4.65±0.31**	**4.50±0.21**

Our average translational and rotational energies at 560K liquid temperature are the highest observed average energies for each of our incident energies in both the IS and TD channel distributions. Our IS channel distributions average translational and rotational energies increase with increasing incident energy, giving further indication that the final energies of species that scatter via the IS channel are substantially influenced by the initial conditions of our gas species. Our TD channel average energies agree reasonably with each other, excepting the result at 12.5kJ/mol incident energy which has a significantly higher average translational energy and rotational energy compared to the results at our other incident energies. We have relatively few data points for the TD channel at this temperature as we will discuss further below, which could result in this variance.

We next examine our population of states relative to z position to determine our cutoffs for the surface and scattering steps, as well as to observe the characteristics of the 560K liquid surface. We plot the percentage occupancy at each z segment below in figure 2-18.

Figure 2-18. Percent Time Occupancy vs. CO_2 center-of-mass z-coordinate, 560K liquid temperature, 55^0 incidence angle, Scattering Step Distribution, TD channel

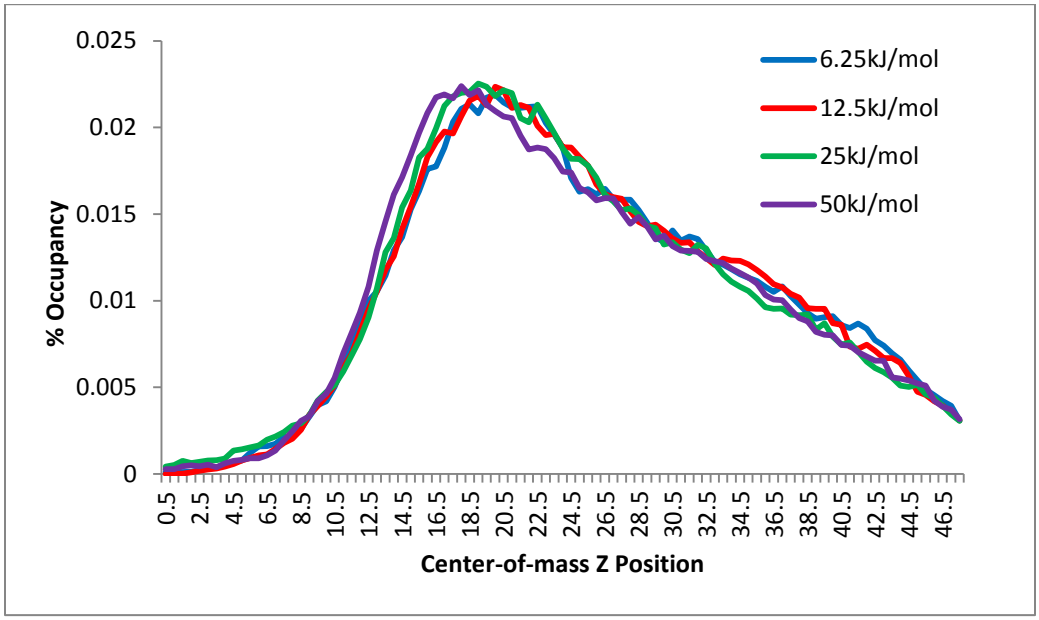

Our surface distribution is substantially broader here than at any of our lower temperatures, with a maximum population between 16Å and 25Å. The linear portion of our plot is difficult to distinguish here, as there is no asymptotic region prior to the plot becoming linear as there was at our lower temperatures. This result makes estimation of the cutoff between our surface and scattering steps problematic by this method, so we use our original estimate (25Å) for our results at this liquid temperature. We still observe relatively little penetration of the surface below 8.5Å, as was the case for all of our previous temperatures.

. In order to determine the change in our gas species' energies during the surface and scattering steps of our trajectory we plot histograms of the average surface step

translational energies and the average energies of all of our gas species' degrees of freedom relative to each z segment below in figures 2-19 and 2-20, respectively.

Figure 2-19. Percent Histogram Bin Occupancy vs. CO2 Translational Energy, 55^0 Incidence angle, 560K temperature, surface step distribution, TD channel

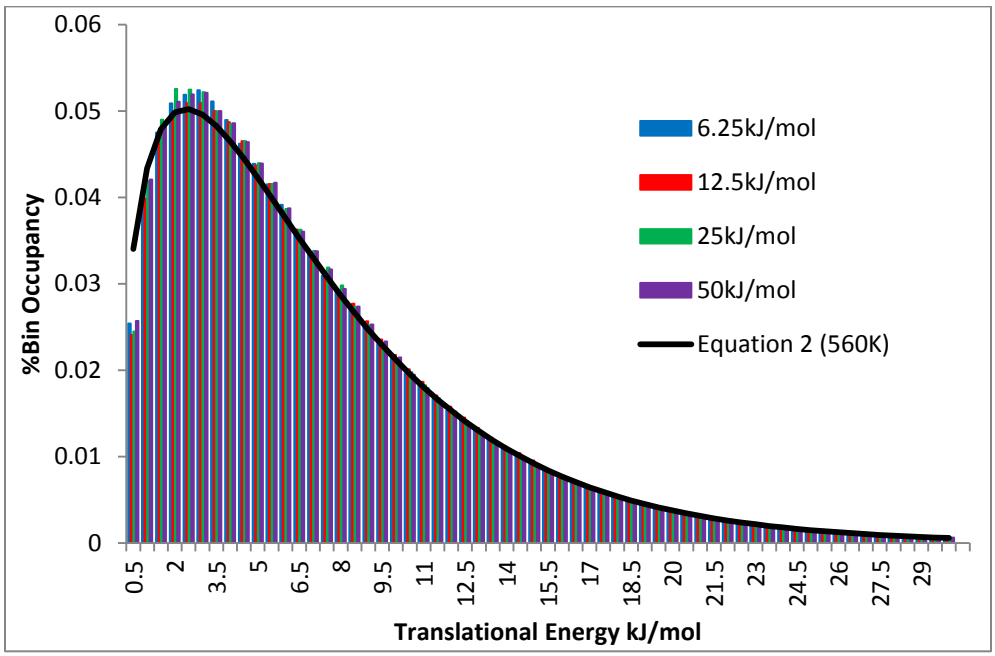

Our surface step distributions conform well to a Maxwell-Boltzmann distribution about the surface temperature, with our calculated distribution fitting our data with R^2 values of 0.98, 0.97, 0.98, and 0.99, with respect to the 6.25kJ/mol, 12.5kJ/mol, 25kJ/mol, and 50kJ/mol incident energies. Additionally, our average energy values for the surface step are 7.11kJ/mol and 4.77kJ/mol with respect to the translational and rotational energy, which agree well with the translational and rotational energy averages computed by the equipartition theorem at 560K, which are 6.97kJ/mol and 4.65kJ/mol, respectively. These results indicate that our gas species is well thermalized to the surface

temperature prior to desorbing from the surface, a trend which we have observed for the surface step at all of our initial temperatures.

Figure 2-20. Average CO_2 Energy vs. CO_2 center-of-mass z-coordinate, 560K liquid temperature, 55^0 incidence angle, TD channel.

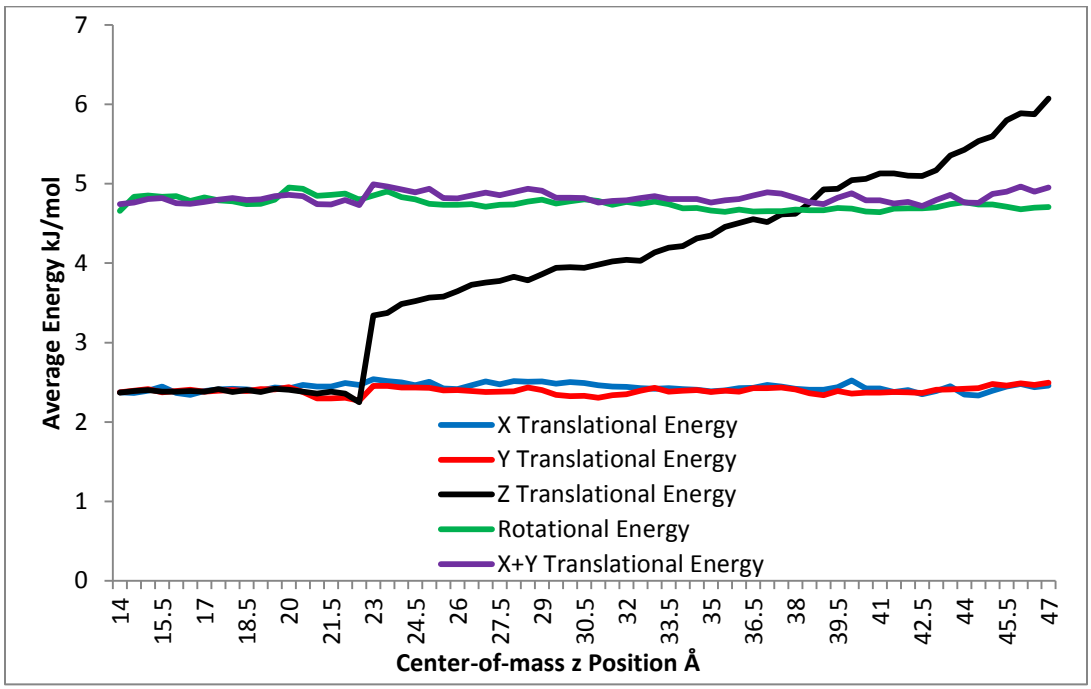

Our average energy plot in figure 2-20 indicates that our x and y translational energies and our total rotational energy remain relatively unchanged while leaving the surface as in our previous studies. We observe that the sum of the average x and y translational energies (4.96kJ/mol) agrees well with both the average total rotational energy (4.7kJ/mol) and the value expected by the equipartition theorem for two degrees of freedom at 560K (4.77kJ/mol). Our z translational energy increases significantly from 21Å to 23Å z position, which we attribute to the H_{Des}. We estimate the value of H_{Des} to

be 1.1kJ/mol by subtracting our average z translational energy on the surface (2.38kJ/mol) from our translational energy average at 23Å (3.48kJ/mol). This estimated value of H_{Des} agrees well with our previously estimated values. We observe a substantial increase in our z translational energy above 23Å, which results from interactions between our gas species and vapor-phase indium atoms. We estimate the average energy change caused by the interactions to be 2.52kJ/mol by subtracting our average z translational energy at 47Å from our average at 23Å. This energy change has increased approximately 25% in value compared to our results at 511K surface temperature. This result is expected, as there are substantially more vapor-phase indium atoms at 560K than at any of our previous surface temperatures.

By examining the fraction of species scattered via the TD channel at each temperature we can determine the fraction of our species that absorb to the surface for each of our initial temperatures. The fraction of TD trajectories for all four incident energies and all four liquid temperatures are displayed in table 2-9. These results were taken at 55^0 incidence angle for all of our initial temperatures and incident energies, and calculated by the methods described above.

Table 2-9. Fraction of trajectories scattered via the TD channel, 55^0 incidence angle

Initial Conditions	TD Fraction 436K	TD Fraction 459K	TD Fraction 511K	TD Fraction 560K
50 kJ/mol	**0.23±0.01**	**0.25±0.02**	**0.27±0.03**	**0.27±0.03**
25kJ/mol	**0.36±0.02**	**0.32±0.03**	**0.31±0.02**	**0.25±0.02**
12.5kJ/mol	**0.39±0.03**	**0.32±0.03**	**0.29±0.02**	**0.24±0.02**
6.25kJ/mol	**0.37±0.03**	**0.30±0.02**	**0.26±0.01**	**0.21±0.01**

We find increasing temperature corresponds with decreasing TD fraction at our three lowest incident energies. Our 50kJ/mol incident energy results display increasing TD channel fraction with increasing temperature, although these are within the standard error of one another which may indicate that this result is not significant. We also note that our two highest incident energies have the highest TD fraction at 560K. This variance from our lower temperature trend may result from collisions between our gas species and vapor-phase indium at the 560K temperature. As the number of vapor-phase indium atoms increases, the chances of a direct collision between our gas species and vapor-phase indium should also increase. It is possible that some of the species scattered via the IS channel scatter directly from vapor-phase indium, and thus scatter without ever reaching the surface. The chance of these direct gas-gas scattering events will increase with increasing liquid vapor pressure, and therefore with temperature. We would expect our lower incident energy results to be particularly affected by gas-gas collisions, as species that approach the surface slowly will have increased chances of colliding with vapor-phase atoms prior to reaching the surface. We also observe fewer trajectories scattered via the TD channel at our higher surface temperatures, which results in the TD channel distributions becoming more susceptible to statistical variance as our temperature increases.

We lastly examine the kinetics of the scattering step for our TD channel distributions. We use our recorded SRT for our gas species in order to estimate the rate constant of desorption (k_{Des}). The literature leads us to expect the rate equation for desorption to be first order.[32, 39] This assumption is also reasonable in the context of our

results, as we have shown substantial evidence that desorption is solely dependent upon our gas species z translational energy component. First-order rate constants are independent of concentration units, thus we should be able to estimate our rate constant by determining the percentage of our TD channel species that remain on the surface after any given time interval. We make use of the integrated rate law for a first-order reaction, shown in equation 5, in order to estimate our rate constant.

$$\ln[A] = -kt + \ln[A_0] \tag{5}$$

In order to estimate our concentration for use in equation 5, we examine the SRT of our species. As we can estimate the number of states leaving the surface at any point based on the SRT values, we can determine the percentage of our trajectories that remain on the surface at any time by subtracting the fraction of species that have left the surface between the initial time and the time length of interest from an initial concentration. We took our initial concentration to be 1 for simplicity, as this eliminates the $\ln[A_0]$ term from equation 5. We then plot the natural log of the percentage of species remaining on the surface against time to determine our rate constants. We display these plots below for all of our temperatures in figure 2-21.

Our data conforms well to equation 5 at all of our surface temperatures, giving good indication that the observed desorption occurs by a first-order process. Equation 5 fits our data with R^2 values of 0.99 for all of our surface temperatures, indicating excellent agreement with the first-order rate law.

Figure 2-21. Natural logarithm of the fraction of species remaining on the surface vs. Time

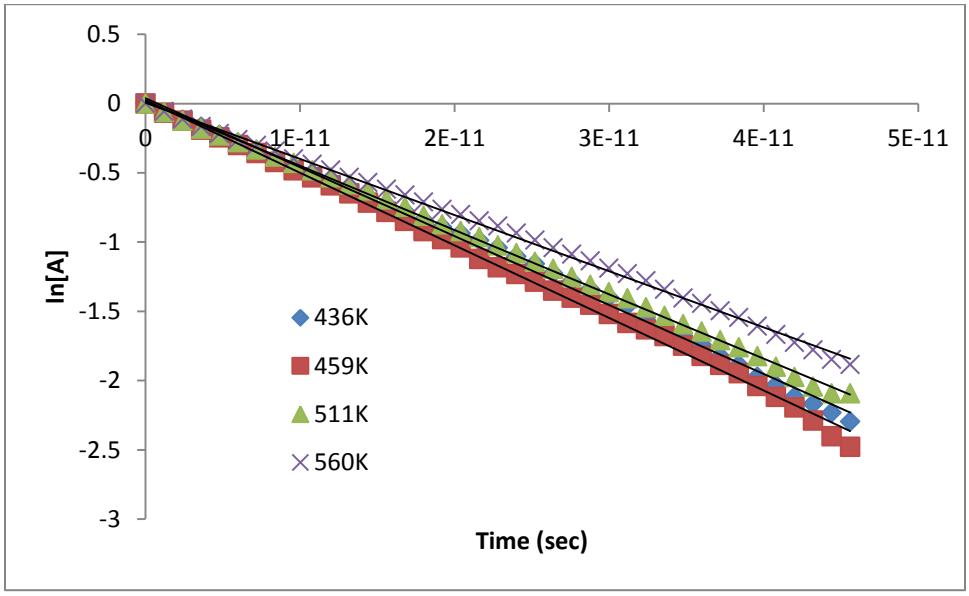

We estimate the value of k_{Des} from the slope of these plots, giving k_{Des} values of $4.70E\pm0.04x10^{10}s^{-1}$, $5.08\pm0.02x10^{10}s^{-1}$, $4.53\pm0.02x10^{10}s^{-1}$, and $3.69\pm0.02x10^{10}s^{-1}$ with respect to our 436K, 459K, 511K, and 560K liquid surfaces. These results are surprising, as we would expect to see an increasing rate with respect to temperature if our E_{aDes} is constant per the Arrhenius equation. While we do note a significant increase in rate from our 436K surface temperature to our 459K surface temperature, we observe significantly lower rate constants at our two highest surface temperatures compared with our two lowest temperatures. We consider changes in the nature of our surface at higher temperatures to be the most likely cause of the decrease in rate constant at higher temperatures. We plot the time population histogram for each of our temperatures below in figure 2-22 to illustrate these changes in our surfaces.

Figure 2-22. Percent Time Occupancy vs. CO_2 center-of-mass z-coordinate position, TD channel distributions.

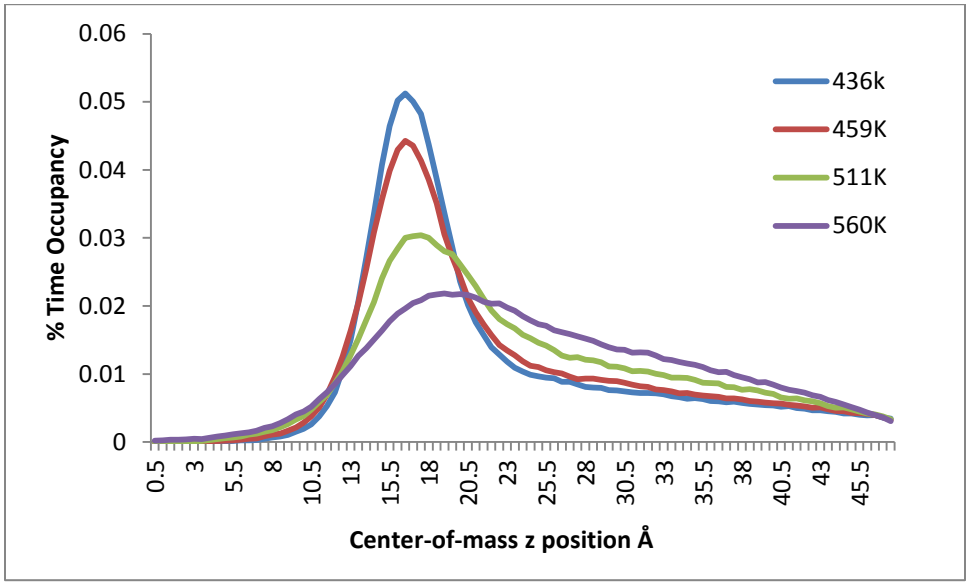

While our 436K and 459K surfaces are relatively similar, we observe substantial surface broadening at our two highest temperatures. As our surface temperature increases we expect our surfaces to become rougher, as illustrated by the figure above. We have previously indicated that long-range attractive surface potential in the z direction is the barrier to desorption. The height of this barrier should be directly proportional to the density of our surface in the z direction. At our lower surface temperatures the surface density in the z direction remains relatively constant and we would expect to see a relatively smooth application of the surface potential to our gas species. By contrast, our higher temperature surfaces have much greater local variance in z density, and therefore in potential applied to our gas species. It is therefore likely that as our temperature increases we find areas of increased z density that favor trapping and

areas of low z density that favor inelastic scattering. These results give further indication that direct gas-gas collisions are responsible for our decrease in TD fraction at higher incident energies, as the observed decrease in the desorption rate constant at higher temperatures indicates that absorption should be increasingly favored at higher temperatures. Several literature studies have also reported increased TD channel fractions at higher liquid temperatures and attributed this effect to the increase in surface roughness at higher surface temperatures.[14, 27, 31, 41] We conclude that absorption becomes increasingly favored with increasing surface temperature; however, the chance of our gas species reaching the surface declines with increasing temperature resulting from direct collisions with vapor-phase indium.

IV. Conclusions

For every set of trajectories run in the present study we observe a wide range of scattered molecule translational and rotational energies. We find that we are able to divide each distribution of trajectories into IS and TD channel components by examining our gas species SRT. We find this method gives us reasonable separation of these channels, although there are some indications in our results that these channels may not be fully separated. We observe that our TD channel average energies typically agree well with each other regardless of our gas species incident energy or incidence angle, while our IS channel average energies increase corresponding with increasing energy and

incidence angle. We also observe that our TD channel rotational energy averages are typically close in value to the average energy expected from the equipartition theorem at each of our surface temperatures. These results agree well with previous work by both our group and others.[3, 12, 14, 20, 23, 35, 41]

We find that our TD channel average translational energies are significantly higher than the values expected from the equipartition theorem for all of our initial conditions. We take this as evidence that gas species scattering via the TD channel do not remain thermalized to the surface temperature after leaving the surface as has been previously hypothesized.[11] We examine the distribution of our gas species' energies during the surface and scattering steps of its trajectories in order to determine the cause of this energy change. We find that there are two factors accounting for our observed energy change: 1.) the enthalpy of desorption ($H_{Des)}$ and 2.) interactions between our gas species and vapor-phase indium atoms. We estimate the value of H_{Des} from our results to be approximately 1.1kJ/mol. We find increasing energy change in our gas species resulting from interactions with vapor-phase indium atoms as our liquid temperature, and therefore vapor pressure, increases. We note that our species cannot move beyond this vapor-phase layer resulting from our simulation box constraints and our detector plane. We expect to observe a decrease in energy resulting from long-range interactions if our gas species was able to move above the vapor-phase indium layer. We find that four of the five total degrees of freedom of our gas species remain well thermalized to the surface temperature for gas species scattered via the TD channel in all of our results, which we attribute to the one-dimensional nature of the Lennard-Jones surface potential.

We examine the fraction of species scattered by each of our scattering channels and find that scattering via the TD channel is increasingly favored at lower incident energy and angles close to the surface normal. These trends agree well with the observed trends in several experimental[3, 12-13, 15] and computational[16-20] studies from the literature, and also agree well with the principle of microscopic reversibility. We estimate the rate constants of desorption using our SRT, and find lower rate constants at our highest two surface temperatures than at our two lowest surface temperatures. We attribute this decrease compared with the trend expected from the Arrhenius equation to the increased roughness of our surface at higher temperatures resulting in increased energy barriers to desorption. We observe a lower fraction of species scattered via the TD channel at higher temperatures, which we attribute to an increased chance of direct scattering resulting from direct gas-gas collisions at higher temperatures.

V. Possibilities for Future Studies

There are several possibilities for further studies that would extend the present work. We observe the effect of both H_{Des} and vapor-phase interactions on our gas species, but we are not able to fully distinguish between these effects. Performing a study using our current methods on a liquid with infinitesimal vapor pressure at ambient temperature would eliminate the effect of vapor-phase interactions and allow us to focus on the estimation of H_{Des}, which should allow us a much more accurate estimate of its value.

Our average trajectory method could also be further refined. While we are able to estimate the value of H_{Des} using our current method, we are not able to estimate the value of either E_{aDes} or our surface binding energy from our present results. Refining our methods to determine the exact collision which causes our gas species to leave the surface and then tracking its energy change as it leaves the surface might allow us to estimate both the E_{aDes} (from the gas species' energy subsequent to this initial collision) and the surface binding energy (from the subsequent energy loss to the surface). We are also unable to determine if species scattered via the IS channel reached the surface using our present methods. Tracking whether our gas species reached the surface would allow us to better determine the effect of direct gas-gas collisions on our IS channel distribution.

We have noted negligible change in the rotational energy of our gas species as it leaves the surface via the TD channel. This result has been observed in several other experimental[15, 35] and computational[18-19] scattering studies performed on linear gas molecules. By replacing our CO_2 molecule with a species of a nonlinear geometry we could determine if this effect remains for species with other geometries. Using a gas species with lower vibrational energy modes than CO_2 would also potentially allow us to determine the effects of desorption from the surface on vibrational energy.

Our present model has examined only weak Van der Waals attractive forces to describe intermolecular interactions. We would be interested to examine a liquid with distributed electrostatic charge about its surface, as these interactions could significantly increase the barriers to desorption. Furthermore, it is possible that a distribution of

surface charges could alter the surface potential sufficiently in directions other than the surface normal to affect additional degrees of freedom of the gas species. It is possible surface charge could cause fewer degrees of freedom to remain thermalized to the surface temperature subsequent to the gas species desorbing from the surface.

Chapter 3

Introduction: Room Temperature Ionic Liquids

Liquid solvents are arguably the single most important group of substances to the field of chemistry. The vast majority of chemical reactions take place in liquid media, and thus liquid solvents are used in the bulk of chemical research performed in both academia and industry.[42] There are numerous different types of solvents used commercially and academically; however, many of them have significant drawbacks. Commonly used solvents are toxic (halogenated hydrocarbons),[43] carcinogenic (benzene, acetonitrile),[44] flammable (concentrated ethanol, nearly every organic solvent), caustic (nitric acid, sulfuric acid), or potentially explosive (ethers). Furthermore, most commonly used solvents have finite vapor pressures, making them problematic due to the potential for both inhalation and evaporation. Solvent evaporation is particularly problematic when working with solutions that need to be maintained at low ambient pressures, as solvents will rapidly evaporate or, if they have sufficiently low boiling points at low pressures, boil away. Research into new solvents is ongoing, and recently attention has turned to the use of ionic liquids as solvents.[45]

Ionic liquids have multiple properties that make them ideal solvents. First and foremost, they have infinitesimal vapor pressures, making them ideal for use under low pressure conditions.[46] This property also makes them safer to handle, as they have very

low associated inhalation risks. Furthermore, because they are nonvolatile, they are far easier to contain, and therefore they pose far less risk to the environment than most common solvents. Additionally, their low vapor pressure makes them reusable as solvents, as they do not evaporate over time, and thus their use can be highly cost effective. Chemically, they are able to dissolve a wide range of species. Some ionic liquids have the ability to dissolve both polar and nonpolar compounds, thereby allowing for the possibility of bringing multiple species into solution that were previously either very difficult or impossible to dissolve simultaneously.[45, 47]

A common misconception is that ionic liquids are a relatively new discovery. The ability to melt common metallic salts into liquids has long been known,[48] and near-room-temperature ionic liquids were reported as early as the late nineteenth century. True room temperature ionic liquids have been reported as early as 1982.[49] However, only recently has research into ionic liquids truly been performed in depth. Early ionic liquids had two major drawbacks to their potential uses in chemistry: they tended to be strongly coordinating and moisture sensitive. Because they remained strongly coordinated, they were far too viscous to be used as solvents, and because they attracted moisture, they would rapidly lose the properties that make them useful. Recently, a wide range of weakly coordinating ionic liquids that are not moisture sensitive have been discovered, along with numerous applications for these ionic liquids.[45, 47]

In conjunction with the recent increase in research on ionic liquids, multiple applications have been found in chemical, biological, and industrial processes. In addition to their used as solvents in chemistry, ionic liquids have proved excellent media

for gas absorption and storage, particularly in the case of CO_2.[50-51] This behavior also makes ionic liquids potentially useful to environmental preservation by using them to scrub CO_2 from the atmosphere. Ionic liquids have also been used heavily in battery research, as they are more conductive than water and have a far lower vapor pressure, making them ideal salt bridges in solid metal batteries because they dry out slower and conduct better than water.[52-54]

Room-temperature ionic liquids (RTILs) have several properties which make them highly interesting. Most RTILs are composed of a large carbocation, with the anion being everything from a simple halogen ion to a complex carboanion. Recently, ammonium has been examined as a possible cation for ionic liquids, as it is relatively common and stable.[55] One of the effects observed in ionic liquids due to their binary nature is a distinctive layering effect, where the cations and anions tend to separate out into layers oriented parallel to the surface. Which species makes up the top layer of the solution depends upon the ionic liquid, with cations having large hydrophobic tails typically making up the uppermost layer. These liquids also tend to be thermally stable at relatively high temperatures (up to 640 K on short time scales). Because of their high boiling points and low vapor pressures, they have great potential for use as solvents in high temperature reactions.[45, 47]

Despite the suitability of RTILs for use as solvents, a relatively small number of reactions have been performed using RTILs as solvents. One of the major drawbacks to the use of RTILs as reaction solvents is their high viscosity, which limits reaction rates in comparison with more conventional lower-viscosity solvents by slowing the encounter

rate of the reacting species. While there is a good deal of literature on the diffusive characteristics of RTILs themselves deriving from both experiment[56-59] and theory,[2, 60-62] relatively little work has been performed on the diffusion of species dissolved by RTILs. The majority of these studies have focused on the applications of RTILs for gas storage, and are performed at pressures well above standard conditions.[56, 63-65] While these experiments yield an understanding of the behavior of ionic liquids under high pressure conditions, they do little to determine the effects of various factors on diffusion through RTILs at more common experimental pressures. By examining the effects of mass, temperature, and polarity on the diffusion of gases through RTILs under standard pressure conditions, we hope to give a clearer picture of the behavior of dissolved species in bulk RTILs.

Chapter 4

Gas Diffusion in Room -Temperature Ionic Liquids

I. Introduction

Recent experiments on gas diffusivity through room-temperature ionic liquids (RTIL) have primarily focused on the suitability of RTILs for gas storage purposes. These experiments typically use high pressure (typically, 25+ atm) to force large quantities of gas molecules into a RTIL, and then determine the number of gas molecules absorbed by the liquid and the diffusion rate of the gas.[56, 63-65] While these studies are excellent for looking at RTILs for storage purposes, they do little to illuminate the behavior of gases diffusing through bulk ionic liquids under standard conditions. By creating a large pressure gradient across the liquid surface, these studies give the diffusive process a driving force described by Fick's laws of diffusion, which is a quite different behavior from what we would expect to see in a liquid at standard conditions, which should more closely conform to the Brownian diffusion model described by Einstein.

One of the potential limiting factors in the use of RTILs as solvents is the high viscosities typical of ionic liquids, limiting the speeds at which gases or solvated molecules can move through them and therefore limiting the reaction rate.[45] By studying the effects of several variables on gas diffusion through RTILs, we hope to understand what effects various factors have on the diffusion rate of dissolved species. We hope these studies will give us a clearer picture of the effects of mass, temperature, and polarity on diffusion through bulk RTILs.

Based on the recommendations of Dr. Gary Baker, we chose1-butyl-3-methylimidazolium (bmim)-PF_6 as the RTIL for our study. We note that bmim-PF_6 is one of the most highly studied ionic liquids in literature, and thus we have multiple sources of comparison for our results as well as force field parameters for use in our study.[46, 66-72] Additionally, bmim-PF_6 is able to dissolve both polar and nonpolar compounds, an ability that makes it a very versatile solvent, and allows us to examine the effects of polarity on diffusion. Finally, bmim-PF_6 is only weakly coordinating, and thus there should be sufficient motion from both the cations and anions to allow diffusion.

The various gases used in our study were chosen for several reasons. We chose to examine CO_2 for two primary reasons. First, there are several studies in the literature on the absorption and diffusion of CO_2 by RTILs, [50, 65, 73-75] providing us sources for comparison of results. Second, CO_2 is the most prevalent contaminant gas in liquid reactions, resulting from its prevalence in the atmosphere as well as its increased reactivity with common solvents (particularly water) compared with other atmospheric gases. Thus, we will be examining the effect of a gas likely to play a role in reactions

performed in RTILs. We lastly chose to examine methane and a range of fluorocarbons from CH_3F to CF_4. These species were chosen insomuch as they have a range of dipole moments and masses, allowing us to examine the effects of both properties on diffusion. There has additionally been an experimental study performed on the diffusion of fluorocarbons in bmim-PF_6,[64] giving us experimental results for possible comparison.

We also chose to examine the effects of temperature on diffusion rates. Our calculations were performed at initial temperatures ranging from 300K to 500K with a 50K step size. We chose this temperature range in order to start near room temperature, have a constant increase in temperature, and end near the upper threshold of the thermal stability of bmim-PF_6. Furthermore, the densities and liquid diffusion constants at these temperatures are available from the literature, providing us a good frame of reference for judging the accuracy of our model.[2]

II. Computational Methods

All of our simulations were performed using DL_POLY v2.18[37] with in-house modifications to support mean squared displacement (MSD) and velocity autocorrelation function (VACF) analyses. Specifically, we modified the source code to output the unfolded center-of-mass coordinates (i.e. those obtained prior to the application of periodic boundary conditions) and center-of-mass velocities for each of our species every

50 simulation timesteps. The intramolecular interactions were described as the sum of the bond stretching, bending and dihedral torsion parameters as shown in equation 1.

$$V_{im} = V_{Bend} + V_{Stretch} + V_{Dihedral} \quad (1)$$

The bond stretches were described by harmonic potentials,

$$U_r = 1/2k(r - r_0)^2 \quad (2)$$

where k is the force constant, r_0 is the equilibrium bond length and r is the bond length of interest. The bond bends were also described by harmonic potentials,

$$U_\theta = k/2(\theta - \theta_0)^2 \quad (3)$$

where k is the force constant, θ_0 is the equilibrium bond angle, and θ is the angle of interest. Lastly, the dihedral torsions were modeled with a triple cosine potential of the form

$$U_\varphi = A_1/2(1 + \cos(\varphi)) + A_2/2(1 - \cos(\varphi)) + A_3/2(1 + \cos(\varphi)) \quad (4)$$

Here φ is the relevant dihedral angle and A_1, A_2, and A_3 are the Fourier scaling coefficients. The intermolecular forces were modeled by a combination of a Lennard-Jones potential shown in equation 5, and a Columbic potential shown in equation 6. The Ewald sum method was used to calculate the electrostatic interactions with a precision of 10^{-6}kJ. Our Lennard Jones cutoff radius was 8.02Å for all of our simulations.

$$V_{LJ} = 4\varepsilon[\left(\frac{\sigma}{r}\right)^{12} - \left(\frac{\sigma}{r}\right)^{6}] \quad (5)$$

$$U(r_{ij}) = \left(\frac{1}{4\pi\epsilon_0}\right) q_i q_j / r_{ij} \quad (6)$$

Our parameters for this study came from a variety of sources as there is not, to our knowledge, a full force field for bmim-PF6 cited in the literature. For our liquid and every diffusing gas, the partial charges were calculated ab initio using Gaussian 03.[76] All calculations were performed at the HF-631G(d) level (Hartree-Fock). Each molecule was initially optimized to determine the equilibrium structure, with a subsequent runs performed to get the RESP charges, as these have been shown in our group's prior research[77] to be markedly more accurate than the Mulliken charges Gaussian calculates by default. For the ionic liquid, the cation and anion were initially optimized individually, with a subsequent optimization performed on the cation-anion pair to determine the best starting configuration. After optimization, each of our species were analyzed using the ANTECHAMBER[78] program to determine the best set of atomic partial charges. Subsequently, each molecule was loaded into AMBER's XLEAP[79] routine in order to get the intramolecular force constants. For all of our molecules, the bending and stretching parameters were extracted from the general Amber force field (*gaff*)[80] using the XLEAP routine available in AmberTools.[79]

All of our intramolecular parameters for diffusing gas molecules were taken from the *gaff*.[80] For the bmim ion, our stretching parameters were taken from *gaff* whereas our bending and dihedral parameters were taken from literature sources. The bending force constants and dihedral parameters describing the hydrocarbon tail of bmim were taken from Lopes et al.[1]; the dihedral parameters describing the imazodide ring were taken

from Alavi et al.[81] For consistency, the Lennard-Jones parameters for C, H, N, P and F were also taken from Lopes et al.[1] The Lennard-Jones parameters for O were taken from literature sources,[38] and all other Lennard-Jones parameters were calculated using standard combination rules. The PF_6^- ion had its internal degrees of freedom frozen to simplify calculations. All of our computations were performed using the SHAKE algorithm to constrain bond stretches involving hydrogen with a tolerance of 10^{-6}.

In order to generate our liquid, the optimized cation-anion pair configuration was replicated onto a 4x4x5 grid in a box of large enough volume to contain them. The cation-anion pair at the origin was then removed and replaced with our diffusing gas molecule. This initial configuration was subsequently compressed by running a short equilibration of 10000 timesteps of 0.6 fs using the Nòse-Hoover thermostat-barostat with a pressure of 1000 atms at a temperature of 300 K under cubic periodic boundary conditions in order to yield a cubic simulation box. This initial step was taken as attempts at initial pressurization to 1.0 atm using our initial configuration failed to converge to the intended pressure in a timely fashion. Once this simulation was complete, we took the final configuration for use in generating our thermalized and pressurized liquid. The liquid was subsequently thermalized and pressurized using the Nòse-Hoover thermostat-barostat at the temperature specific to the computation and a pressure of 1.0 atmosphere for 1000000 timesteps of 0.6 fs. These pressurization steps were integrated using the Verlet leapfrog algorithm under constant number pressure temperature (NPT) setting. The density of the ionic liquid was then calculated in order to verify that the liquid was properly equilibrated, with results typically being within ± 2%

of the experimental density values at each temperature examined.[2] In order to ensure good thermalization to our intended temperature, we subsequently thermalized each of our starting configurations using the Nòse-Hoover thermostat for 1000000 timesteps of 0.6 fs integrated using the Verlet leapfrog algorithm under constant number volume temperature (NVT) setting. The final configuration of each of these thermalization runs was taken for use as a starting configuration for our diffusive studies. Additional starting configurations were generated by extending the thermalization runs by an additional 200000 timesteps of 0.6 fs to ensure a new configuration. Six additional starting configurations were generated for each set of initial conditions. Subsequently, we performed a constant number volume energy (NVE) simulation using the Verlet Leapfrog algorithm for 2000000 timesteps of .6 fs for each starting configuration from which we extracted our diffusive results.

In order to determine our diffusion constants, we initially used mean square displacement methods as developed by Einstein in his work on Brownian motion.[82] Our general results were calculated using the Einstein relation shown in equation 6.

$$< (x_t - x_{ti})^2 > + < (y_t - y_{ti})^2 > + < (z_t - z_{ti})^2 >= 6D\Delta t \qquad (6)$$

Here Δx, Δy, and Δz represent the average change in the corresponding center-of-mass coordinate for the given change in time interval, with the sum representing the total mean square displacement (MSD). D is the diffusion coefficient and 6 is a numerical constant for the dimensionality (representing six possible directions of motion). By plotting the sum of the average squared displacements versus the change in time, we are able to

obtain a plot with a slope equal to 6D, from which we can readily extract the diffusion coefficients.

In order for this method to be effective, our algorithm must use time averages. Each MSD value was calculated over a constant average of exactly 35000 different coordinate changes. For each time interval examined, we chose an initial time 50 timesteps ahead of the previous initial time, and averaged the MSD over a constant number of values. This procedure implies that the maximum time change we examined was 5000 steps of the total simulation time; however, this strategy is supported by previous studies appearing in the literature.[1-2] We plot the MSD of the center-of-mass coordinates of the molecule in order to remove any effect of vibrational or rotational motion. Both the cation and the anion MSD values were averaged over all 79 molecules in order to get the best possible results. We subsequently averaged the MSD results of each of our 7 initial configurations to obtain a final MSD plot in order to estimate the diffusion constant.

Each MSD value was then plotted versus its time in order to determine the diffusion coefficient. These determinations were based on the most linear part of the MSD plot, noting that the initial region involves ballistic motion of the diffusing molecules prior to undergoing collisions and over long changes in time the data becomes less linear. This observed decrease in linearity at longer times has been attributed to the high viscosity of ionic liquids.[1-2] While this procedure describes a somewhat crude method of determining diffusion coefficients, it has been proven reasonably accurate.[1-2] One potential problem with using MSD analysis in this particular system is that it

assumes all molecules in the system are undergoing a random displacement walk. While this assumption is valid for simple models such as Lennard-Jones liquids, it may not prove to be the case for complex RTILs. This assumption is particularly problematic in the case of the diffusing gas molecules, insomuch as they have a tendency to become trapped over short time lengths. This will be discussed further in the results section.

While our MSD results had plots with clear linear portions for our cation and anion species, the MSD plots of our diffusing gas sometimes lacked the continuous linear region necessary for the estimation of the diffusion constant. This effect is likely attributable to the lower number of gas species in our system from which to take statistics compared to our cation and anion, as well as the possibility of our gas species diffusing selectively over short time lengths. In order to better determine the diffusion constant of our gas species, we use the Green-Kubo relations to determine our diffusion constant using the velocity autocorrelation function (VACF) described by equation 7.

$$D_0 = 1/3 \int_0^\infty (v_i(t_0) * v_i(t))\Delta t \quad (7)$$

Here the 1/3 term accounts for three dimensions, and the velocity terms account for the change in correlation between our velocity at an initial time and the velocity after a given time interval. In order to estimate the diffusion coefficient, it is necessary to integrate this equation to the infinite time limit. Our resulting autocorrelation function is not easily fitted to a functional form that allows for indefinite integration, nor does it converge to a constant value as it has a significant long time tail. We instead examine the running

numeric integral of our VACF, which has been shown to be well described by equation 8.[83-84]

$$f(t) = Ae^{-Bt} + C \tag{8}$$

where

$$f(t) = \int_0^t (v_i(t_0) * v_i(t)\,)\,\Delta t \tag{9}$$

Taking the infinite limit of equation 8 yields

$$\lim_{t\to\infty} f(t) \cong \lim_{t\to\infty} A\,e^{-Bt} + C \cong C \tag{10}$$

Substituting equation 10 into equation 7 results in equation 11,

$$D_0 = C/3 \tag{11}$$

from which we can estimate our diffusion coefficient. By fitting the running numerical integral of our calculated VACF function to equation 8 we are able to estimate the diffusion constant for our gas species. Similarly to our MSD calculations, we average all of our starting configuration results to obtain an overall VACF function for each set of initial conditions in order to get the best possible statistics for our VACF analyses.

III. Results and Discussion

In order to validate our force field, we first calculated the densities of our RTIL in order to compare them to experimentally known values. Our density values were calculated by simply dividing the mass of the ionic liquid by its volume as computed by our cell lengths after barometric and thermal equilibration. These density values were averaged over all computations performed for a given temperature in order to yield the best possible results, as well as to provide us with a means of estimating error. The average density values are displayed, along with the experimental values and error calculations, in table 4-1.

Table 4-1. Average density values for bmim-PF_6 from our computations compared to experimental values from Lopes et al.[1]

Liquid Temperature	Calculated Density g/cm^3	Experimental Density g/cm^3	% Error
300 K	**1.35±0.03**	**1.36**	**1.27**
350 K	**1.29±0.03**	**1.32**	**2.19**
400 K	**1.26±0.03**	**1.28**	**1.11**
450 K	**1.21±0.03**	**1.23**	**2.34**
500K	**1.17±0.06**	**1.19**	**1.77**

Our density values agree reasonably well with experiment, with all values within 2.5% of the observed densities. Our model does tend to underestimate the density values consistently, however. Some of this underestimation may be attributable to the presence of our diffusing gas molecules, which could potentially expand the volume and reduce the density of the system. The simulated and experimental densities are plotted against temperature in figure 4-1.

Figure 4-1. bmim PF_6 Density vs. Temperature, calculated and experimental values

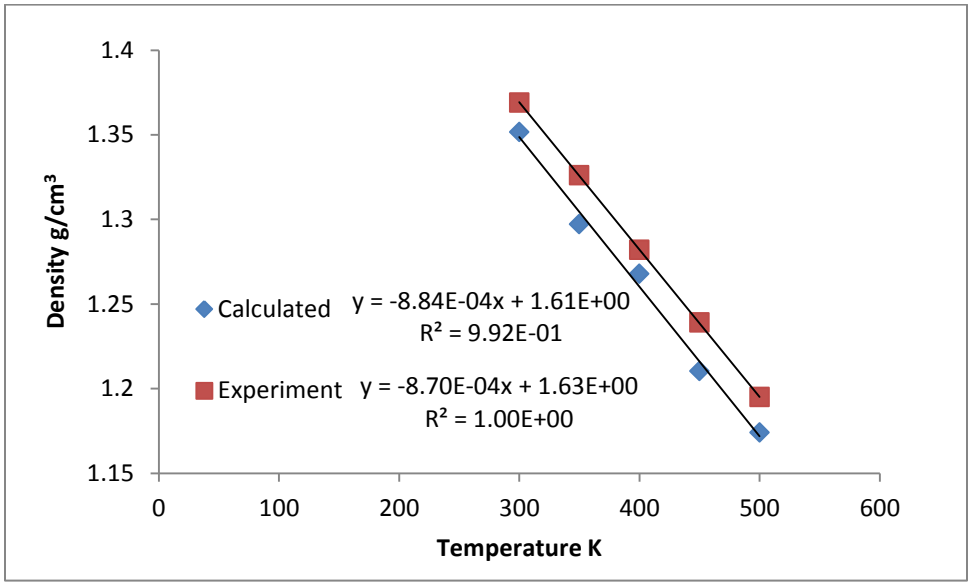

The calculated and experimental data can be fit to a linear equation with R^2 values of 0.99, and 1.0 respectively, giving indication of excellent linearity in the density profiles. Our calculated densities also agree well with other theoretical work, [1-2] indicating our model is giving us a reasonable approximation of the bulk properties of the liquid.

The layering effect of ionic liquids has long been observed, and for our model to fit the physical properties of the bulk liquid adequately it must exhibit this behavior. We could potentially observe layering in any of our coordinate directions, as our simulations lack any surfaces or external forces for use as a directional reference frame. We examine the density profiles of the center-of-mass of our cation and anion species in order to determine if there is an observable layering effect in any of our coordinate directions. We have recorded the center-of-mass positions of all of our species every 50 simulation timesteps for our MSD analyses, and we use this data to estimate the density of each

species in each coordinate direction by binning the center-of-mass positions of our species over 1Å intervals in each coordinate direction. We bin these positions over the entire trajectory in order to ensure the best possible statistics. We then divide each bin range by the total number of states to calculate a percentage bin occupancy histogram of our density in each direction. We display a histogram of the z center-of-mass coordinate for our 300K temperature liquid below in figure 4-2.

Figure 4-2. Histogram Bin Occupancy vs. Center-of-mass z position, 300K initial temperature

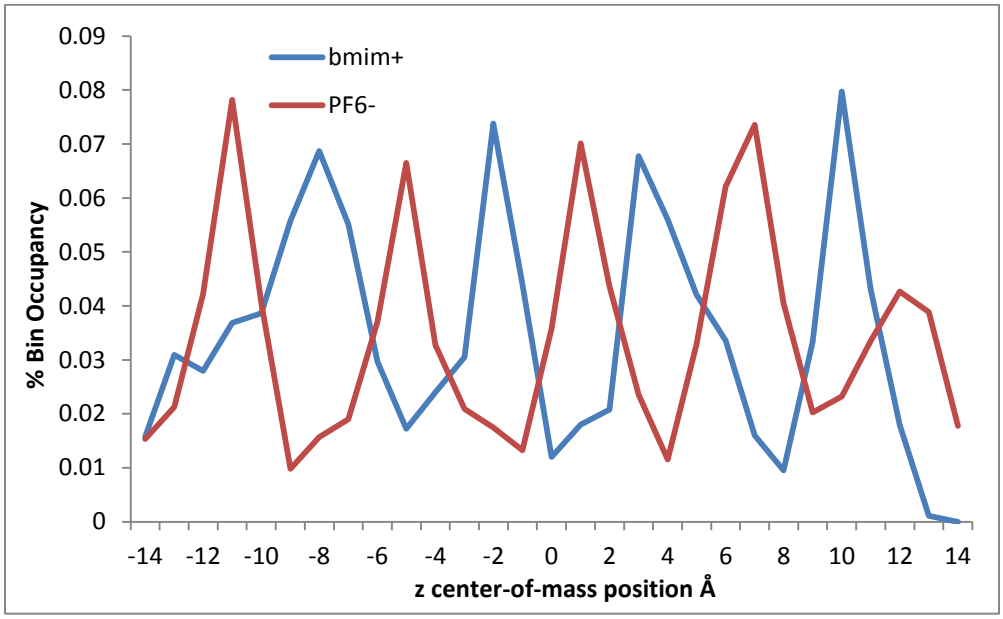

We find an observable center-of-mass layering effect in the z-coordinate direction in all of our simulations. This observed coordinate preference for layering likely results from our initial configuration prior to pressurization, which was the same in all of our simulations. We observe that maximum peaks for one species roughly correlate to

minima for the other, a result indicating that our layers are well separated with respect the z direction. We do note several points on our distribution in which the cation and anion appear to have similar occupancies. This effect may result from our histogram binning, in which case this overlap could simply correspond to a change in layers occurring within the same bin range. The anion species has been shown to be capable of diffusing across layers, [66-70] thus it would be unsurprising to occasionally find some anions at positions within our cation layers as they diffuse through. We also note some roughness around the maximum and minimum z-coordinates which likely results from our periodic boundary conditions being applied about these points. These results agree well with other experimental and theoretical studies of bmim-PF_6 in the literature.[66-71]

In order to further validate our force field, we calculate the diffusion coefficients at each temperature for both the anion and the cation in order to compare our calculated coefficients with literature sources. In order to ensure the most accurate statistics, we took the averaged diffusion constant values calculated for each starting configuration at each temperature. These were calculated by plotting the MSD versus time interval according to the Einstein relation shown in equation 6. We display some of these plots bellow in figures 4-3 and 4-4.

Figure 4-3. MSD (in cm^2) vs. Time Interval, 300 K liquid temperature, methane diffusing gas

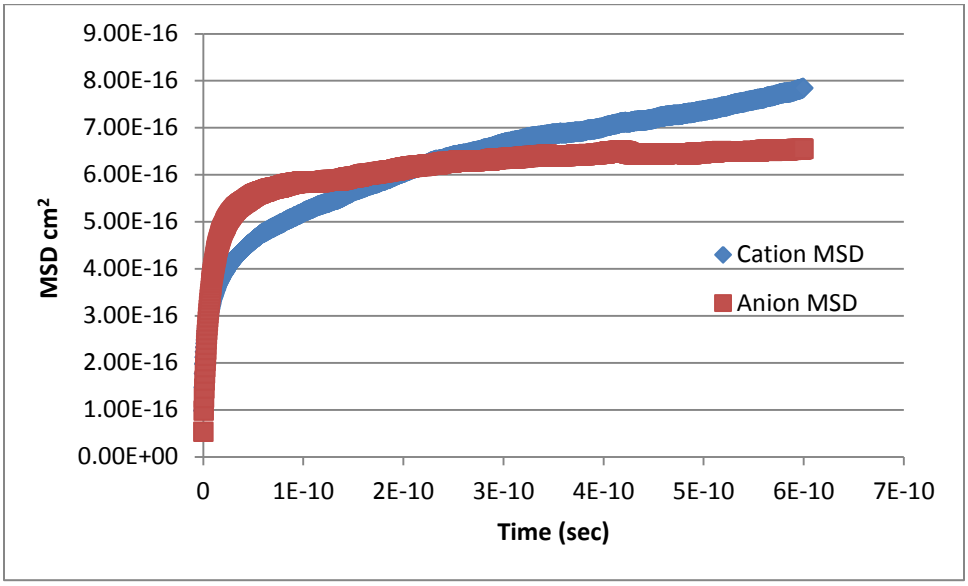

Figure 4-4. MSD in cm^2 vs. Time Interval in seconds, 500 K liquid temperature, methane diffusing gas

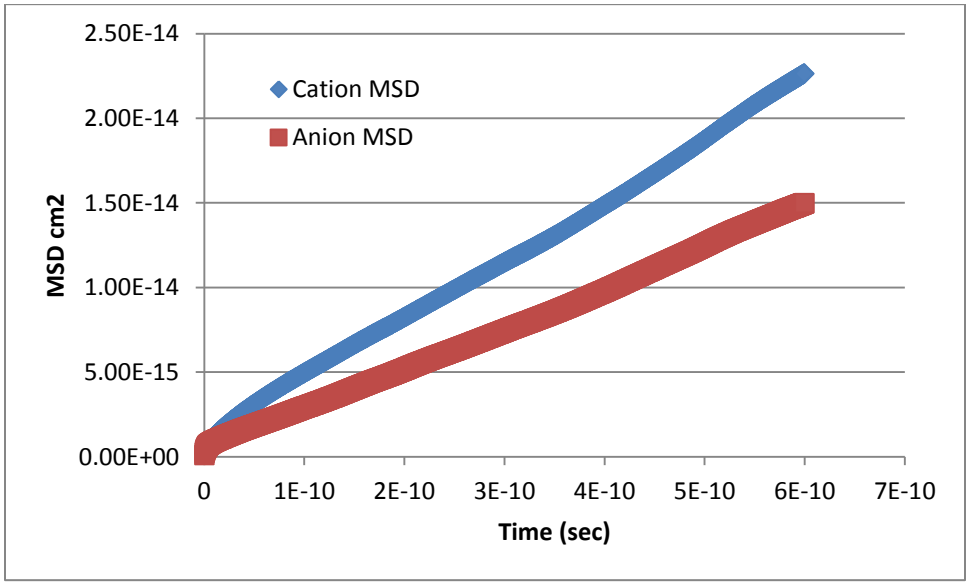

These plots exhibit characteristic MSD behavior, indicating good agreement with the assumption of Brownian random walk motion. We see a much shorter ballistic region at 500K than 300K, a result which we would expect due to the higher average particle velocities at higher temperatures. It is clear from these plots that the cation diffuses at a faster rate than does the anion, which has been well documented in the literature.[66-70] In order to further verify that our data gives a good fit to random walk motion, we plot the x, y, and z components of the MSD in order to determine whether there is any preferential direction of motion. In a true random walk situation, we would expect to see good convergence of all three components. We display this data in figures 4-5 and 4-6.

Figure 4-5. MSD vs. Time Interval, x, y, z components, 300 K liquid temperature, methane diffusing gas

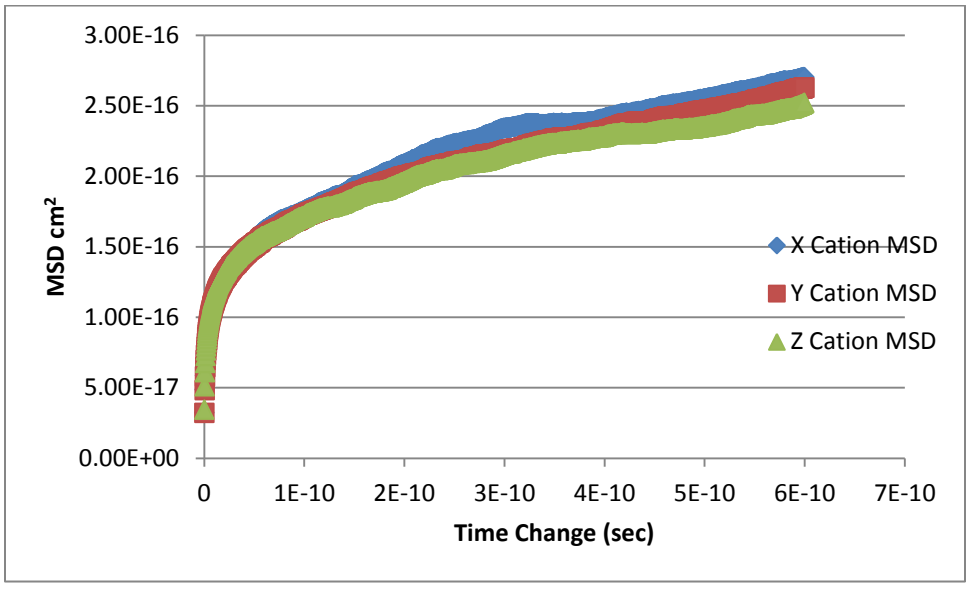

Figure 4-6. MSD vs. Time Interval, x, y, z components, 500 K liquid temperature, methane diffusing gas

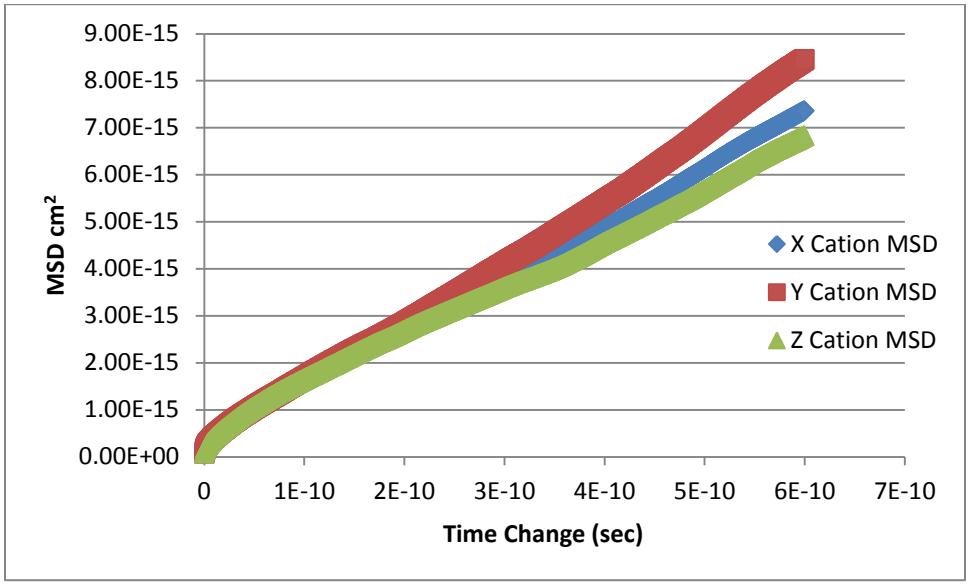

We observe lower MSD values for our z-coordinate that for x and y at both temperatures. This result is unsurprising given the layered nature of our liquid in the z direction, and agrees well with the known behavior of the $bmim^+$ ion. We also note significant differences in our x and y MSD, particularly at 500K. Several literature sources have indicated that $bmim^+$ preferentially diffuses in the direction of the axis of the butyl tail through the imidazole ring.[66, 68, 83-84] This preferential diffusion can be attributed to the geometry of the $bmim^+$ ion. Diffusion in the directions of the plane of the imidazole ring requires less free space than diffusion in the direction perpendicular to the plane of the imidazole ring and is therefore favored. Similarly, less free space is required for diffusion in directions parallel to the alkyl chain than in directions perpendicular to it. The combination of these geometric factors leads to diffusion being

favored in directions parallel to the plane of the imidazole ring in the direction of the alkyl chain tail. This preferential diffusion could account for the observed discrepancy in the x and y MSD, as whichever direction is closest to the preferred diffusive direction of the $bmim^+$ species on average should have the highest diffusion coefficient. We therefore conclude that our cation does not undergo a true three dimensional random walk. What we observe is a separate random walk for each coordinate direction, with differing diffusion coefficients in each direction. As each direction is well described by the Einstein method, we can use the sum MSD to obtain a three dimensional diffusion constant for quantitative analysis, with the understanding that this coefficient does not represent equal diffusion in all directions.

In order to obtain the most accurate MSD statistics at each temperature we averaged the MSD values for each of our trajectories at each set of initial conditions to obtain an average MSD distribution. We then fit the linear portion of the resulting MSD curve to obtain the diffusion constants for both the cation and the anion by equation 6. Our typical MSD plots for the cation and anion species yielded very linear plots with typical R^2 values of 0.990 or greater. A sample plot using this method is displayed below in figure 4-7. We averaged the calculated slope of the MSD plot of each of our initial configurations at each set of initial conditions, and obtained a final D_0 value by averaging these resulting slope values over our 7 starting configurations, with the error in our D_0 values represented by the error in this average.

Figure 4-7. MSD vs. Time interval, 300 K liquid temperature, cation distribution

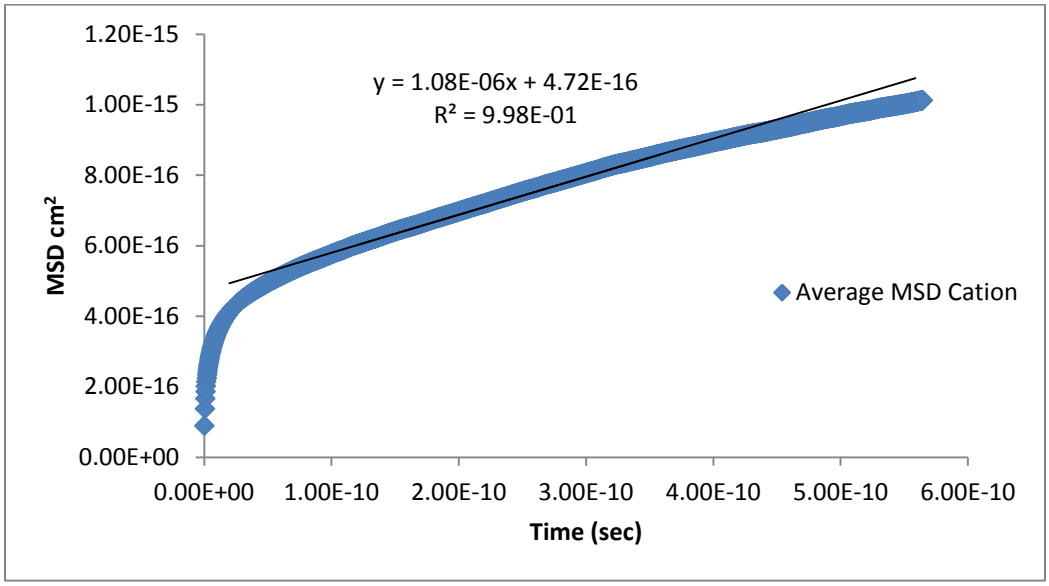

In order to verify our parameters, we compare our diffusion coefficients to experimental studies in table 4-2. We find that we are generally within a factor of 2 or 3 of experimental results at all temperatures, an agreement which is very reasonable given the small size of our model. We also find we obtain diffusion constants in reasonable agreement with several theoretical studies in the literature.[66, 68, 70] We see an increase in diffusion constant with increasing temperature, in accordance with predicted trends. We also observe the cation diffusing more rapidly than the anion, a trend which also agrees well with literature results.[2, 66, 68] We do tend to observe slightly lower values for the anion by percentage of the cation's diffusion constant than do some other studies.[66-69] This effect may be attributable to our partial charges and Lennard-Jones parameters for fluorine compared with those used by other computational studies. We in general tend to underestimate the diffusion constants for both species except at 300K; a tendency which

is consistent with the results of other theoretical studies that have shown that molecular dynamics underestimates diffusion coefficients in the case of RTILs.[2, 83-84]

Table 4-2. Diffusion constants for cation and anion species, 10^{-6} cm^2/sec, with comparison literature values from Bhargava et al.[2]

Liquid Temperature	Calculated D_{Cation}	Calculated D_{Anion}	Experimental D_{Cation}	Experimental D_{Anion}
300 K	0.17±.04	0.066±.02	0.08	0.059
350 K	0.36±.06	0.14±.03	0.642	0.514
400 K	1.07±.15	0.52±.09	2.09	1.786
450 K	1.80±.32	1.76±.29	4.47	4.013
500K	4.62±.53	3.41±.34	7.60	7.079

These results indicate that our force field gives us a reasonable approximation of the bulk properties of the bmim-PF_6 liquid.

We now turn our attention to the gases diffusing through the liquid. We initially attempted to determine the diffusion coefficients of our gas species using the same MSD methods we used to determine the rate constants of the cation and anion species. We found that the MSD plots for our gas species did not always have linear portions for use in estimating the diffusion coefficient. This lack of linearity likely resulted from trapping of the gas species, as we will discuss in further detail below. We instead use the velocity auto correlation function methods described above to determine our gas species' diffusion coefficients. In order to verify our VACF method, we first use the VACF method to examine the cation and anion species and compare our values to those calculated using the MSD method. We display these values below in table 4-3.

Table 4-3. Diffusion constants for cation and anion species calculated using VACF, 10^{-6} cm^2/sec, with comparison literature values

Liquid Temperature	Calculated D_{Cation}	Calculated D_{Anion}	Experimental D_{Cation}	Experimental D_{Anion}
300 K	0.03±0.02	0.02±0.009	0.08	0.059
350 K	0.133±0.21	0.07±0.03	.642	.514
400 K	0.616±0.23	0.33±0.11	2.09	1.786
450 K	1.60±0.46	1.34±0.32	4.47	4.013
500K	3.09±0.73	2.01±0.43	7.60	7.079

We find that our VACF results agree reasonably with our MSD results, although we consistently underestimate the diffusion constants compare to both our MSD D_0 values and the experimental values. The VACFs of ionic liquids have been noted to require substantially longer times to converge compared to the MSD,[2, 83-84] which could account for the observed difference in our D_0 values. We also find our error to be higher for our VACF analysis. We display a plot of our normalized VACF at each of our temperatures below in figure 4-8.

We can use the plot in figure 4-8 to estimate the average collision time for both of our species by the point at which the VACF first become negative. We find that the cation species has a shorter average collision time than the anion species for all of our temperatures giving further indication that our cation species diffuses faster than does our anion species. We also note increasing collision time corresponding with increased temperature. Our anion VACF functions appear as a single damped oscillation as we would expect for a liquid. By contrast, we observe two oscillations in the VACF function

of our cation species. We take this result as further evidence that our $bmim^+$ ion diffuses by more than one mode.[83-84]

Figure 4-8. Normalized Cation and Anion VACF vs. Time interval

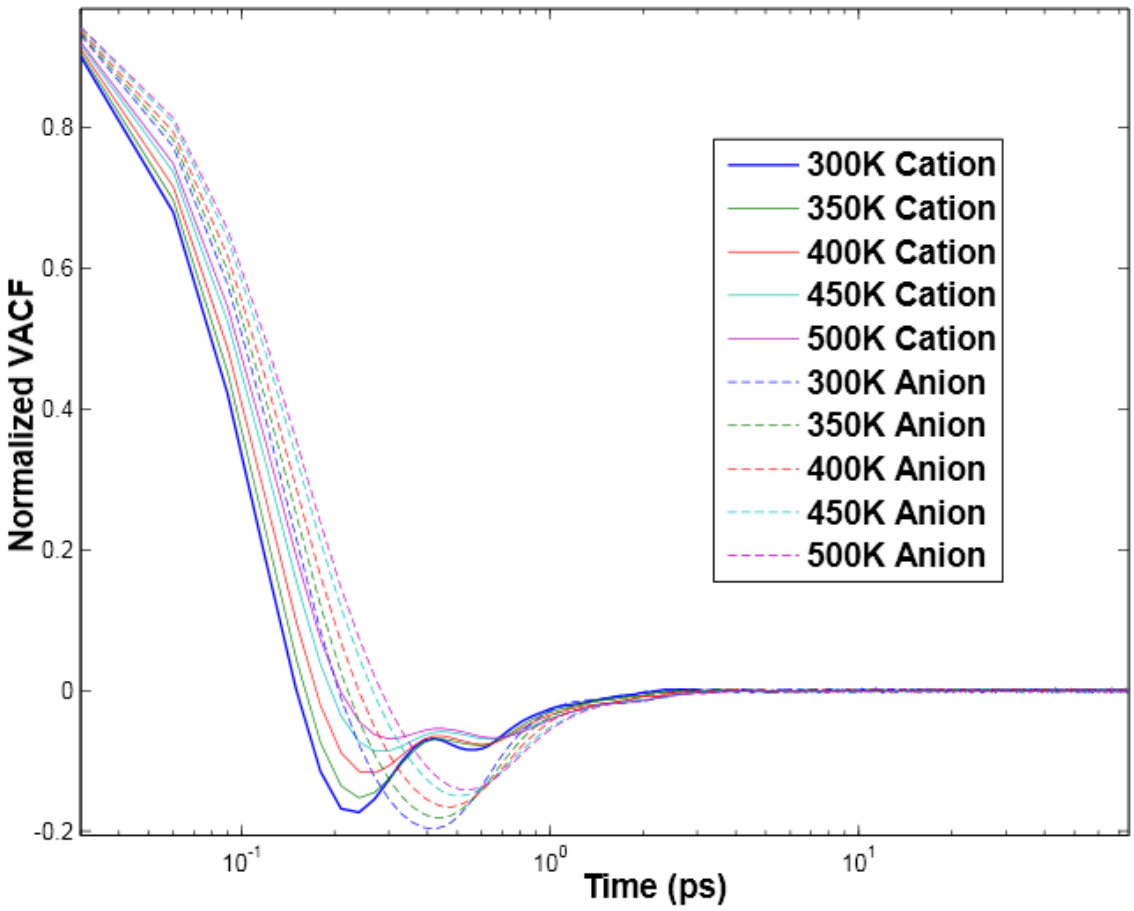

We next examine the VACF results for our diffusing gas species at each of our initial temperatures. We display a plot of the VACF of methane against time for our four highest temperatures below in figure 4-9.

Figure 4-9. Methane VACF vs. Time interval

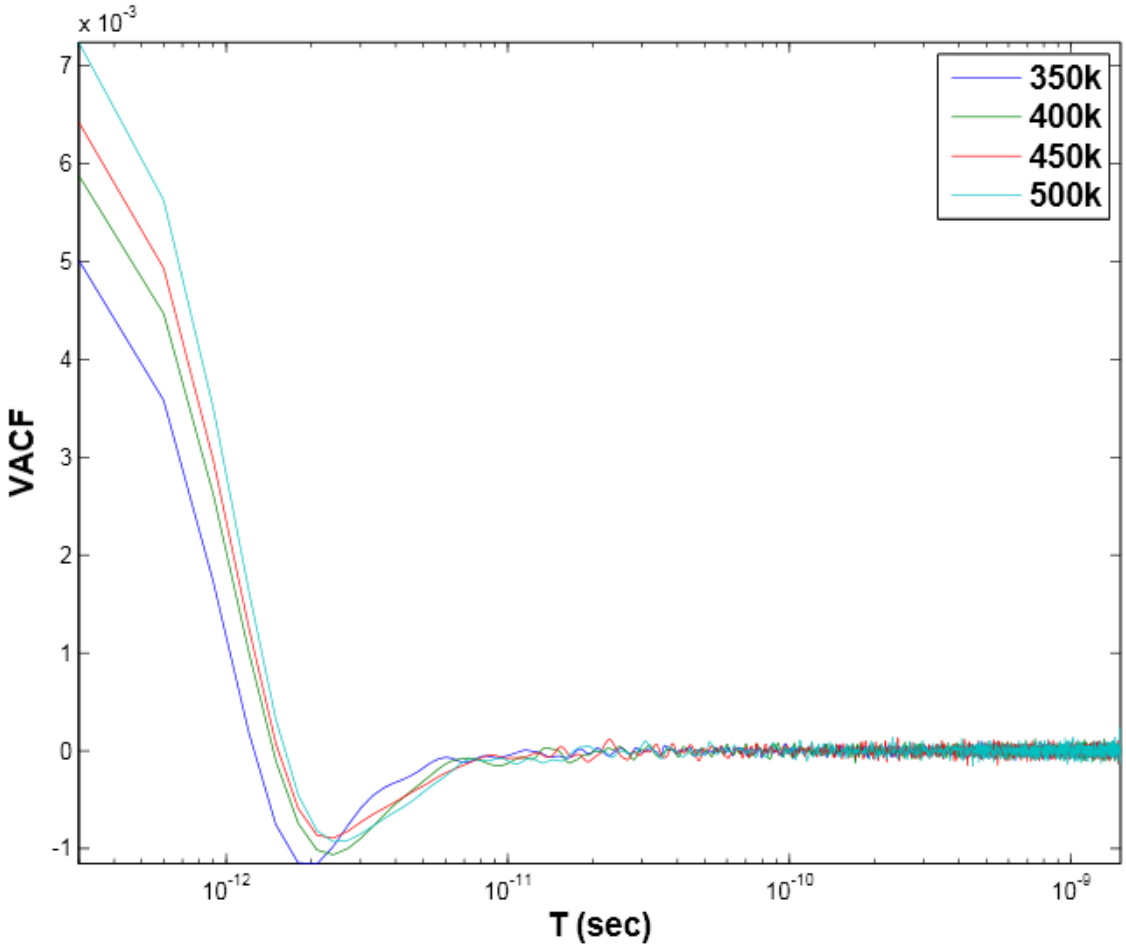

We observe a single damped oscillation in the VACF function for methane similar to our anion VACF functions. Increasing temperature corresponds with decreasing collision time as we expect. We note that our VACF at 350K is significantly lower than our VACF at higher temperatures. This decrease in VACF likely results from an increase in the probability of trapping, which we will discuss in further detail below. We observe similar VACF for all of our diffusing gas species. We also note the presence of a significant long time tail in our VACF, indicating our VACF may not have converged for

our gas species. This result necessitates the use of curve fitting to determine our gas species D_0 from our VACF results.[83-84]

In order to use the VACF to estimate our diffusion constant, we fit the running numeric integral of the VACF to equation 8 using the MATLAB R2012a curve fitting toolbox[85], with the error in our diffusion coefficient taken as the calculated fitting error of the C term of equation 8. We obtained R^2 values between 0.95 and 0.75 from fitting equation 8 to our VACF data. We display a plot of the running numeric integral of our VACF against time interval below in figure 4-10 for methane at 300K, with the best fit of equation 8 to the data displayed to illustrate this technique.

Figure 4-10. Running Numeric Integral of Methane VACF vs. Time interval, 300K

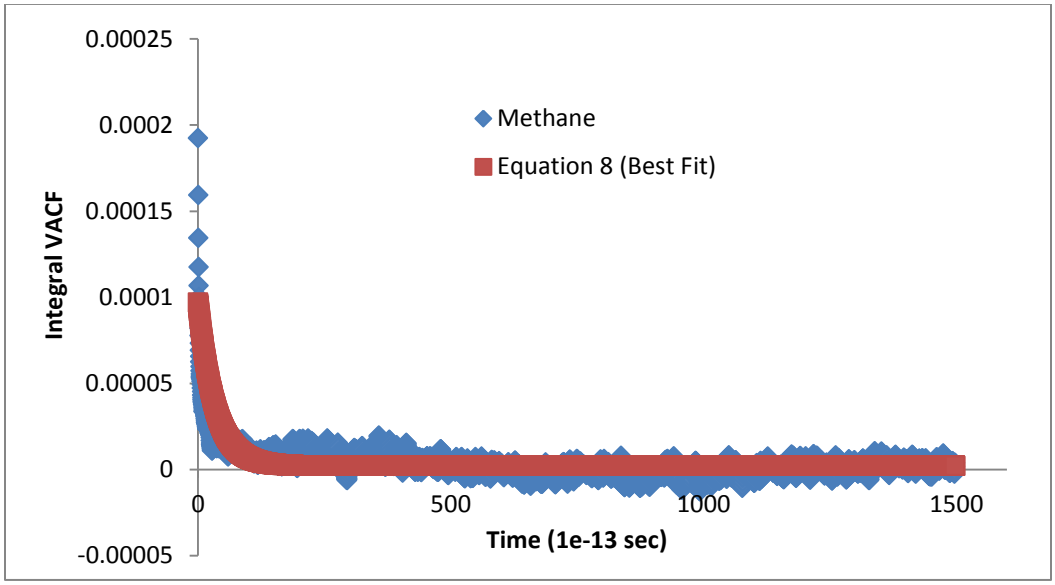

We observe a reasonable fit to our data from equation 8 (R^2 value 0.86); however, we observe relatively high error in our diffusion coefficient estimate ($8.65\pm2.12\times10^{-7}$

cm^2/sec) from this fit. We note that the running integral of the VACF is negative at numerous points on our curve. This negativity in the VACF integral has been shown to indicate short time trapping, [83-84] giving us further evidence that our gas species can become trapped on short timescales. We display our calculated diffusion coefficients for each gas species below in table 4-4. Gas species with substantial negative regions in the VACF running integral are marked with an asterisk is the table to indicate the possible influence of trapping on their diffusion coefficients.

Table 4-4. Calculated Diffusion constants for gas species, 10^{-6} cm^2/sec, Trapped results marked with asterisk

Gas Species	D_0 300K	D_0 350K	D_0 400K	D_0 450K	D_0 500K
CH_4	0.865±0.21*	5.06±1.5	18.7±4.2	138.3±27.2	150.2±32.3
CH_3F	1.6±0.32*	5.13±1.6	17.3±4.1	34.0±6.8	68.1±12.1
CO_2	2.24±0.71*	2.33±0.82*	29.1±6.7	48.8±8.1	69.7±12.4
CH_2F_2	8.93±2.2	6.04±1.8	19.8±5.1	37.6±7.2	77.7±12.5
CHF_3	3.15±0.92	9.48±2.3	15.8±3.8	39.3±7.1	66.7±.10.2
CF_4	0.64±0.18*	4.67±1.2	10.8±3.1	28.6±5.3	65.5±11.4

For each of our diffusing gas species we observe increasing D_0 with increasing temperature as we would expect, excepting our results for CH_2F_2 which see D_0 decrease from 300K to 350K. Our lower temperature diffusion results appear to be particularly affected by short time effects such as trapping which could account for this decrease. At our lowest temperatures we also observe significant evidence of trapping, as half of our gas species show substantial negative regions to their VACF integrals at 300K, and CO_2 continues to show evidence of trapping at 350K. We also note that all of our species have some negative points on their VACF integral curves at 300K and 350K, indicating

that trapping is common at these temperatures, with some of our results particularly affected by trapping at these temperatures. Our gas species' diffusion constants at these temperatures appear to be affected more by short time trapping than by either mass or dipole moment.

In order to determine if there is an observable trend in our diffusion coefficients relating to our gas species' mass or dipole moment we plot our D_0 values against gas species; mass and dipole moment below in figures 4-11 and 4-12, respectively.

Figure 4-11. Diffusion constant, $10^{-6}cm^2/sec$ vs. Gas Species Mass

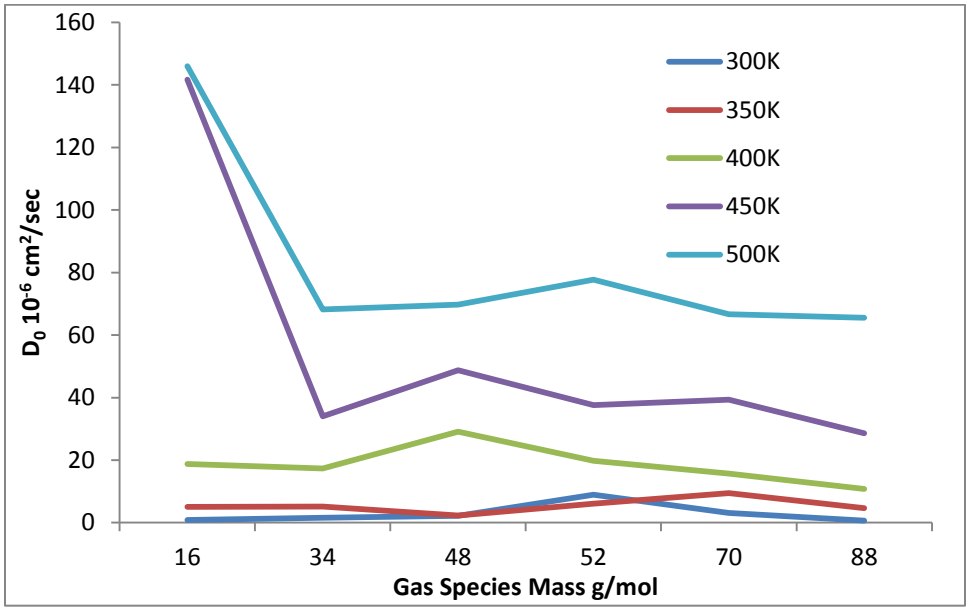

Figure 4-12. Diffusion constant, $10^{-6}cm^2/sec$ vs. Gas Species Dipole moment

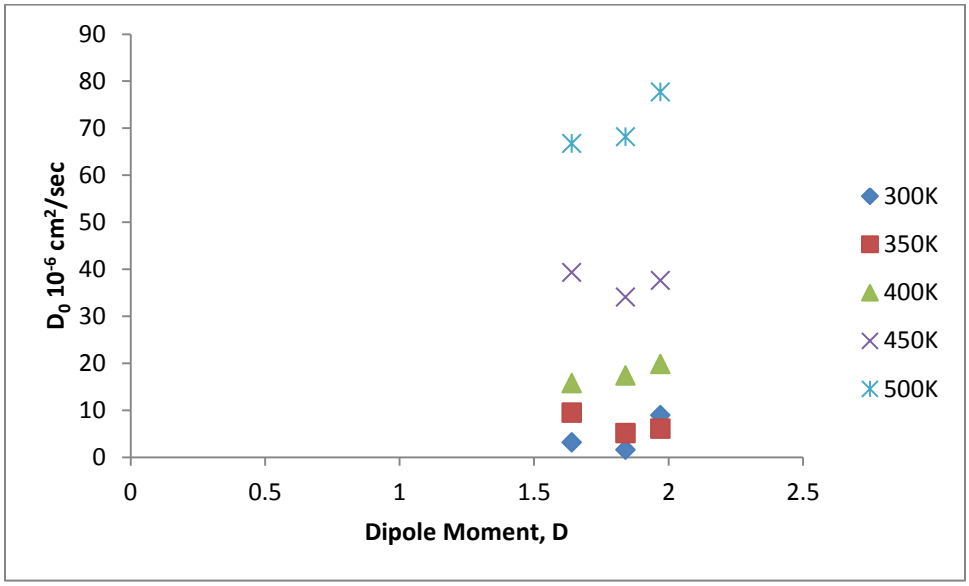

We note a slight trend of higher diffusion coefficients correlating to lower mass, but this is not consistent throughout our results as the three most massive gasses show some fluctuation in our mass curve and CO_2 consistently diffuses faster than CH_3F at higher temperatures. Our dipole moment plot shows our most dipolar species, CH_2F_2, (dipole moment 1.98D) typically diffuses faster than CH_3F (dipole moment 1.84D). We observe CHF_3 diffuses faster than CH_3F over most of our temperature range despite having twice the mass of CH_3F. We note that CH_3F was one of our trapped species at lower temperatures, which could account for its reduced diffusivity compared to heavier species. It is also important to consider the possibility that our Lennard-Jones parameters are affecting our results, as the F-F self-interaction force constant and interactive radius (0.25 and 3.12) are larger than those for the H-H self-interaction (0.12 and 2.5) and therefore our species with higher numbers of fluorine atoms may experience additional

Van der Waals forces as well as electrostatics. We are unable to definitively observe a direct correlation between diffusivity and mass or dipole moment, although we do have some indication that heavier species diffuse at low rates on average. We feel that local trapping effects are substantially affecting our results, particularly at lower temperatures, and therefore we may be underestimating the diffusion coefficients of certain species that were trapped on our timescale above what we would expect in the actual system. As we are only able to obtain averages over one molecule as a result of our pressure, we find that we may not have enough statistics for any underlying trends to be definitively qualified.

IV. Conclusions

We find that our model of bmim-PF_6 is reasonably accurate in replicating the bulk properties of the ionic liquid, including the density, the layering effect, and the diffusion constants of both the cation and the anion. Our calculated diffusion constants for the $bmim^+$ and PF_6^- ions are within a factor of two or three of experimental results from the literature,[2] and agree reasonably with several other computational studies.[66-70, 84] We typically underestimate the values of our diffusion coefficient compared to the experimental values, a result which has been observed in other MD studies of ionic liquids.[66-70, 83-84] We observe a general trend of increased liquid diffusion rate and decreased density with increasing temperature, which also agrees well with literature

results.[1-2] Our cation displays evidence of multiple diffusive modes, which we attribute to the geometry of the $bmim^+$ cation.[66, 68, 83-84]

For our diffusing gas particles, we find that on the relatively short timescales over which we perform our experiments, local trapping effects can significantly alter the diffusion coefficient, particularly on short time scales. Our CH_4 species has one of the lowest diffusion coefficients at 300K despite being our lightest gas species. Our VACF integral curves display substantial evidence of trapping represented by extended negative regions for several of our species. We conclude that short time trapping is primarily responsible for our observed behavior at lower temperatures. At higher temperatures methane consistently diffuses faster than our other gas species; however, there are no definite correlations between mass or dipole moment and diffusion coefficient apparent from our results. Our methods for estimating these diffusion coefficients are rough, especially in the case of VACF, and we observe significant error in both our MSD and VACF analyses.

We have found it problematic to definitively correlate our diffusion results to a general trend describing diffusion in relation to mass or dipole moment. This result is partially explained by local trapping; however, we may not have enough statistics to determine any trends with certainty. As our pressure conditions only allow for the examination of a single gas species by these methods, our gas diffusion results are particularly susceptible to statistical variance. As these computations carry a substantial cost, it may be impractical to use the MSD and VACF method to examine low pressure gasses diffusing through liquids.

V. Possibilities for Future Studies

Taking additional data to improve our statistics for MSD and VACF could substantially improve this study. As we are only able to examine one gas species per trajectory run, and we observe short time events having substantial impact on our results, more statistics should lead to better estimates of our gas species' diffusion coefficients. We find much better fits to our MSD and VACF plots for our cation and anion species than our gas species, as we have 79 times the amount of data. We note that the number of simulations necessary to fully examine these diffusion rates may be prohibitive to examining low pressure gas diffusion.

While we have managed to characterize one RTIL, these are numerous other possible combinations of cations and anions. We could attempt to determine diffusion through various different anion and cation species. Specifically, it would be useful to look at faster diffusing cations and anions in order to attempt to create a lower viscosity solvent that was still able to dissolve multiple different kinds of molecules as well as have near infinitesimal vapor pressure. We could examine combinations of anions that are known to be faster diffusing, such as halogen ions, and cations with varying length hydrocarbon tails such as pmim, smim, and emim, which will have different diffusion rates from bmim.

It is possible that using additional gas species could enable us to better determine trends relating to mass and dipole moment. Examining another six gases would give us

more reference points on our mass and dipole plots and might enable us to better determine an average trend. Examining additional atmospheric gases such as N_2, O_2, and water would allow us to examine the effects of gasses more commonly encountered in a laboratory setting than fluorinated alkanes.

APPENDIX A

Simulation of CO_2 Scattering Using DL_POLY v. 2.14

Modifications to DL_POLY 2.14 code:

In order to facilitate simulations of surface scattering we have added several subroutines to the DL_POLY 2.14 code. We modified DL_POLY 2.14 to set our gas species at a random initial position and orientation relative to the surface, fix its incident energy and angle relative to the liquid surface, and load our liquid surface snapshots for each trajectory run. We additionally modified DL_POLY 2.14 to calculate both the translational and rotational energy of our gas species every 10 timesteps, and record these values as well as the z center-of-mass coordinate of our gas species to facilitate average trajectory analysis. A list of our modified and added DL_POLY 2.14 files is shown below.

Modified DL_POLY routines: dlpoly.f; dl_params.inc; systemp.f; traject.u.f; vscaleg.f error.f; makefile; quatqnch.f; quench.f; simdef.f; sysdef.f

Added DL_POLY routines:

rotresult.f – Routine to calculate final CO_2 translational and rotational energy

posread.f – Routine to load new surface snapshot for each scattering trajectory

scatter.f – Routine to randomize CO_2 initial position and set incident CO_2 energy and CO_2 incidence angle.

recenter.f – Routine to recenter the bulk liquids center-of-mass in the z direction to the origin

reset.f – Calls above routines to start new simulation trajectory

Our modification to DL_POLY are available through the Adams Research Group. For further information, please contact Dr. John E. Adams, 125 Chemistry, University of Missouri-Columbia, Columbia, MO 65211; email: AdamsJE@missouri.edu

Sample DL_POLY input files:

CONFIG – File containing initial coordinates, velocities, and forces for all species

```
Lattice file generated by FILE_MAKER utility
         2          3     10000    0.6700000000E-02
       28.3800000000        0.0000000000        0.0000000000
        0.0000000000       28.3800000000        0.0000000000
        0.0000000000        0.0000000000      100.0000000000
O               1
     0.000000000        -1.170000000         48.00000000
     0.000000000         0.000000000         0.000000000
     0.000000000         0.000000000         0.000000000
O               2
     0.000000000         1.170000000         48.00000000
     0.000000000         0.000000000         0.000000000
     0.000000000         0.000000000         0.000000000
C               3
     0.000000000         0.000000000         48.00000000
     0.000000000         0.000000000         0.000000000
     0.000000000         0.000000000         0.000000000
In              4
    -4.312874177        -11.91480649         4.688999633
   -0.8916189498        0.6339304688        0.4639006117E-01
    -1509.489856         787.1667132        -1526.453356
In              5
     12.98042307         3.050710720         8.615255999
    -3.116169774        -1.362340991        0.6984951346
     250.7028726         381.0348773        -2715.923720
```

CONTROL – File to control simulation settings

```
CONTROL file generated by DL_POLY/java utility

temperature      459.00
pressure         0.0000
ensemble nve

steps            200000
equilibration         0
multiple step         1
print              1000
stack              1000
stats            100000

timestep         0.0006
cutoff           7.0250
delr width       1.0000
rvdw cutoff      7.0250
no electrostatics
shake tolerance  1.0E-5
quaternion tolerance  1.0E-5

detector         49.0000
cycle            2300
scatter          50.000000
scatangle        55.000000


job time              100000000.0
close time            1000.000


finish
```

FIELD – File to set the interaction parameters for all species

```
Simulation of Liquid indium,
UNITS kJ
Scatter 3
MOLECULES 2
Carbon Dioxide   (incoming particle)
nummols 1
atoms 3
 O       16.00000     0.000000    2
 C       12.01100     0.000000    1
rigid 1
3    1    2    3
finish
Indium
nummols 864
atoms 1
 In      114.82       0.0         1
finish
vdw 6
In      In      lj     5.04525     2.810
In      C       lj     1.08632     2.784
In      O       lj     1.83774     2.922
C       C       lj     0.23390     2.757
C       O       lj     0.39570     2.892
O       O       lj     0.66940     3.033
close


# CO2 parameters
#ref Johnathan G. Harris and Kwong H. Yung
#  J. Phys. Chem. 1995, 99, 12021-12024
#charges omitted
```

APPENDIX B

Simulations of Gas Diffusion using DL_POLYv 2.18

Modifications to DL_POLY 2.18 code:

In order to support our MSD and VACF analysis, we modified the main dl_poly.f file to output the center-of-mass positions and velocities for each of our species every 50 timesteps. In the case of the center-of-mass positions, we output the unfolded coordinates (ie prior to the application of periodic boundary conditions). This was accomplished by adding the length of the cell to the current position of a given species for every time it has diffused across the boundary condition. These modifications are also available through the Adams Group.

Sample DL_POLY files:

CONFIG – File containing initial positions, forces, and velocities. We show a section of a CONFIG file for one anion, one cation, and one gas species below.

```
Lattice file generated by FILE_MAKER utility
         2         1   1000000    0.6000000000E-03
       30.5122098670        0.0000000000        0.0000000000
        0.0000000000       30.5122098670        0.0000000000
        0.0000000000        0.0000000000       30.5122098670
P               1
     13.25280421         12.91676409         12.23280072
    0.4340907999       -0.1425962010       -2.552513656
    -1125.181922         215.4236636         926.5740313
F               2
     13.55861805         14.46374904         12.14794402
```

```
    -1.888660367        0.3340988280        -2.233026988
     245.9894983        -2947.966829         19.23853639
F               3
     14.77377763         12.55028271         12.04135950
     1.015767469         2.187406040        -2.391564427
    -1679.443274         1665.605675         473.4169245
F               4
     13.39467590         12.91491905         13.80401711
    0.2035378876       -0.2067882529        -2.531771449
    -344.5648860        -1257.132071        -2084.998514
F               5
     12.87086322         11.33645997         12.26031620
     2.815656735       -0.7240551555        -2.889208789
     1838.005575         1335.540798        -1128.857869
F               6
     11.67079808         13.23601721         12.37296425
   -0.6867418467E-01     -2.555649798        -2.730893903
     1242.999382        -431.3170010        -825.6776644
F               7
     13.03773304         12.87081720         10.62171887
    0.7427115059       -0.1818444951        -2.592593605

    -306.0723175        -254.2532358         969.5428813
```

.....

```
N             554
     14.84330010        -14.40183643         8.842222462
     2.827523607         5.622363095        0.5219676689
    -16333.86926        -14551.91322        -3190.738165
C             555
    -15.12068488         15.20646921         7.794617109
    -5.069049908        0.8284493596        -1.175831555
    -6367.773600        -3558.300309        -7100.221152
H             556
     14.68170421         15.15697923         6.902619419
    -16.15938097        -27.94098310       -0.7903104051
     8513.088441         449.6226733         11385.38271
H             557
    -14.14063128        -14.92388219         7.367369347
     54.37366193         10.30585643         10.74946310
    -2469.679562         937.0559928         2730.292085
C             558
    -14.86792959         13.74356216         8.292639760
     1.023771320         5.934440187         5.000734623
    -5541.053585        -5914.656415        -11430.79217
H             559
     14.70177081         13.22780754         8.597755335
     7.774303647         16.13795029        -8.820530869
```

```
     6604.157310         6559.789008        -2070.770667
H              560
    -14.21219293         13.71158395         9.119223721
    -9.259250350         10.43364889         1.851463223
     4041.200401         3263.481868         9015.589191
C              561
    -14.18944882         12.83518046         7.192869558
     2.860965263        -6.723815447       -0.2774237416
    -5458.666536         10459.37520         3912.601679
H              562
    -15.01438550         12.62282100         6.546047495
    -2.535366636         20.02410492         33.75558034
     770.4062067        -107.7007082        -3571.092235
H              563
    -13.39316387         13.39663029         6.610589950
     4.310309937         15.73391830         23.03134561
    -6916.252445        -7316.533523         7114.299617
C              564
    -13.76655358         11.49356415         7.793984907
    -1.472903324         2.367569483        -7.746166567
    -592.4459500         2317.923909        -9901.986170
H              565
    -13.24860229         10.90366892         7.013877745
     6.324978107        -37.78397186         9.753995213
    -3374.950753        -1589.281793         3599.579136
H              566
    -13.08540427         11.66613659         8.573689942
     23.05247576         17.92154777        -13.58470967
     12280.67598         2797.865021         8142.163490
H              567
    -14.54684257         10.96329885         8.313453563
     3.601197613         16.30198452        -21.13539138
    -3220.981934        -1899.828798        -5420.719902
C              568
     13.57286605        -14.52703465         9.503523399
     3.174875614         2.467419063        0.2635648704
     17960.16438         7477.425497         6698.679299
C              569
    -14.98408887        -13.44385536         9.518172429
     3.324761764        -3.487137681        -5.171025549
     13501.05880         3951.357419        -2269.613940
H              570
    -13.99083208        -13.26923000         9.142727516
    -6.380700742        -18.79279522         9.713924445
    -1928.557979         1671.795607         2393.400010
C              571
     14.61151061        -12.62435679         9.985980541
    -8.450482464        -4.468197679         2.911044655
    -14700.45470         1763.413961         11743.52241
```

```
N              572
     13.69165649        -13.57251885         10.56609294
    0.6936549641        -6.730675284        -1.755135267
     824.4374969         5723.162869        -22786.13402
H              573
     14.61744717        -11.49550990         10.06123314
     3.379246376         11.74092319        -9.594624882
    -150.8334293        -11835.05992         202.0758331
H              574
     12.89680954         15.11871928         9.457021614
     16.05065793        -9.353338677        -8.033211866
     3365.067558         5288.719040         442.2387175
C              575
     12.52903590        -13.26555258         11.39736213
     8.557476510         3.803568859        -1.141192843
    -1361.129199        -5855.992370         6150.790743
H              576
     11.93631797        -14.17808908         11.59970390
    -13.60849291         1.662341205        -14.30299488
     1319.280833         3831.782974        -1321.252774
H              577
     12.79596312        -12.90963401         12.37083133
    -7.765684472         4.733247511        -1.344619664
     2390.972594         887.0302228         2385.100969
H              578
     11.83407209        -12.53641946         11.01871019
    -3.012072326        -14.33131346        -12.17244935
    -218.6302338         985.6579408        -3843.813127
```

.....

```
C              2529
     6.701793319        -3.338106162         3.885189495
     4.025521736         15.95448184         5.882858869
     6127.437529        -11555.73427        -9421.362374
H              2530
     7.227664151        -3.922394699         4.648190261
    -6.131420248        -9.819147239        -4.093971265
     593.6238619         978.5430413        -108.0411364
H              2531
     6.778749427        -3.789269854         2.865811540
     5.766605185        -12.82890309        -19.35153923
    -3788.962189        -5648.047281         3276.078794
F              2532
     5.477252012        -3.082699772         4.230503360
   -0.3661206927        -2.346548089       -0.1308119081
    -12718.53359        -2490.119690         4870.350163
F              2533
     7.197245234        -2.188509350         3.677471779
```

```
     2.704284258        -8.200884175        -3.732019371
     12026.95529         16591.69099         1997.404710
```

CONTROL - File to control simulation settings

```
CONTROL file generated by DL_POLY/java utility

temperature      300.00
pressure         0.0010
ensemble nve

steps           2000000
equilibration         0
multiple step         1
print               400
stack              1000
stats            100000

timestep         0.0006
cutoff           8.0250
delr width       1.0000
rvdw cutoff      8.0250
ewald precision  1.0E-5

shake tolerance  1.0E-5
quaternion tolerance  1.0E-5


job time              100000000.0
close time            1000.000


finish
```

FIELD - File to set the interaction parameters for all species

```
DL_POLY BMIM_PF6
units kJ
molecules  3
PF6
nummols 79
atoms 7
    P       30.97300   1.1060000    1    0    1
    F       18.99800  -0.3510000    1    0    1
    F       18.99800  -0.3510000    1    0    1
    F       18.99800  -0.3510000    1    0    1
    F       18.99800  -0.3510000    1    0    1
    F       18.99800  -0.3510000    1    0    1
    F       18.99800  -0.3510000    1    0    1
rigid 1
7    1    2    3    4    5    6    7
finish
BMIM
nummols  79
atoms  25
    N       14.00674   0.0468150    1    0    1
    C       12.01100  -0.0704020    1    0    1
    H        1.00794   0.0995620    1    0    1
    H        1.00794   0.1104960    1    0    1
    C       12.01100   0.0053960    1    0    1
    H        1.00794   0.0168940    1    0    1
    H        1.00794   0.0351660    1    0    1
    C       12.01100   0.0634800    1    0    1
    H        1.00794   0.0227080    1    0    1
    H        1.00794   0.0085970    1    0    1
    C       12.01100  -0.1912050    1    0    1
    H        1.00794   0.0776220    1    0    1
    H        1.00794   0.0398480    1    0    1
    H        1.00794   0.0545080    1    0    1
    C       12.01100   0.0014410    1    0    1
    C       12.01100  -0.2096480    1    0    1
    H        1.00794   0.2645640    1    0    1
    C       12.01100  -0.1851140    1    0    1
    N       14.00674   0.1586070    1    0    1
    H        1.00794   0.2490800    1    0    1
    H        1.00794   0.2278730    1    0    1
    C       12.01100  -0.3409750    1    0    1
    H        1.00794   0.1647140    1    0    1
    H        1.00794   0.1763070    1    0    1
    H        1.00794   0.1736650    1    0    1
bonds 25
harm   1   2     2800.1      1.456
harm   19  22    2800.1      1.456
```

```
harm   18  16    4943.6      1.324
harm   18  19    3440.1      1.391
harm   1   16    3440.1      1.391
harm   1   15    3440.1      1.391
harm   15  19    3440.1      1.391
harm   15  21    2991.5      1.078
harm   18  20    2991.5      1.078
harm   16  17    2991.5      1.078
harm   2   5     2536.3      1.535
harm   5   8     2536.3      1.535
harm   11  8     2536.3      1.535
harm   22  23    2917.1      1.084
harm   22  24    2917.1      1.084
harm   22  25    2917.1      1.084
harm   2   3     2810.8      1.093
harm   2   4     2810.8      1.093
harm   5   6     2810.8      1.093
harm   5   7     2810.8      1.093
harm   8   9     2810.8      1.093
harm   8   10    2810.8      1.093
harm   11  12    2822.5      1.092
harm   11  13    2822.5      1.092
harm   11  14    2822.5      1.092
angles 45
harm   18  19  15   292.600     107.9
harm   16  1   15   292.600     107.9
harm   18  19  22   292.600     126.8
harm   16  1   2    292.600     126.8
harm   15  19  22   292.600     125.6
harm   15  1   2    292.600     125.6
harm   19  15  21   143.600     125.1
harm   1   15  21   143.600     125.1
harm   1   15  19   292.600     109.3
harm   1   16  18   292.600     107.8
harm   19  18  16   292.600     107.8
harm   1   16  17   146.300     122.0
harm   19  18  20   146.300     122.0
harm   18  16  17   146.300     130.9
harm   16  18  20   146.300     130.9
harm   19  22  23   313.200     110.7
harm   19  22  24   313.200     110.7
harm   19  22  25   313.200     110.7
harm   1   2   3    313.200     110.7
harm   1   2   4    313.200     110.7
harm   2   5   6    313.200     110.7
harm   2   5   7    313.200     110.7
harm   5   8   9    313.200     110.7
harm   5   8   10   313.200     110.7
harm   5   2   3    313.200     110.7
```

```
harm    5    2    4     313.200      110.7
harm    8    5    6     313.200      110.7
harm    8    5    7     313.200      110.7
harm    11   8    9     313.200      110.7
harm    11   8    10    313.200      110.7
harm    8    11   12    313.200      110.7
harm    8    11   13    313.200      110.7
harm    8    11   14    313.200      110.7
harm    1    2    5     418.400      111.5
harm    2    5    8     418.400      111.5
harm    5    8    11    418.400      111.5
harm    4    2    3     276.100      107.8
harm    7    5    6     276.100      107.8
harm    9    8    10    276.100      107.8
harm    25   22   23    276.100      107.8
harm    25   22   24    276.100      107.8
harm    24   22   23    276.100      107.8
harm    13   11   12    276.100      107.8
harm    13   11   14    276.100      107.8
harm    14   11   12    276.100      107.8
dihedrals 35
cos3    22   19   15   21   0.0      19.46   0.0    0.0000   0.00
cos3    18   19   15   21   0.0      19.46   0.0    0.0000   0.00
cos3    2    1    15   21   0.0      19.46   0.0    0.0000   0.00
cos3    16   1    15   21   0.0      19.46   0.0    0.0000   0.00
cos3    20   18   16   17   0.0      44.98   0.0    0.0000   0.00
cos3    20   18   16   1    0.0      44.98   0.0    0.0000   0.00
cos3    19   18   16   17   0.0      44.98   0.0    0.0000   0.00
cos3    20   18   19   22   0.0      12.55   0.0    0.0000   0.00
cos3    20   18   19   15   0.0      12.55   0.0    0.0000   0.00
cos3    16   18   19   22   0.0      12.55   0.0    0.0000   0.00
cos3    16   18   19   15   0.0      12.55   0.0    0.0000   0.00
cos3    17   16   1    2    0.0      12.55   0.0    0.0000   0.00
cos3    17   16   1    15   0.0      12.55   0.0    0.0000   0.00
cos3    18   16   1    2    0.0      12.55   0.0    0.0000   0.00
cos3    18   16   1    15   0.0      12.55   0.0    0.0000   0.00
cos3    16   1    2    3    0.0      0.0     0.55   0.0000   0.00
cos3    16   1    2    4    0.0      0.0     0.55   0.0000   0.00
cos3    18   19   22   23   0.0      0.0     0.55   0.0000   0.00
cos3    18   19   22   24   0.0      0.0     0.55   0.0000   0.00
cos3    18   19   22   25   0.0      0.0     0.55   0.0000   0.00
cos3    16   1    2    5   -5.76     4.43    0.877  0.0000   0.00
cos3    15   1    2    5   -3.23     0.0     0.0    0.0000   0.00
cos3    4    2    5    7    0.0      8.37    0.0    0.0000   0.00
cos3    4    2    5    6    0.0      8.37    0.0    0.0000   0.00
cos3    3    2    5    7    0.0      8.37    0.0    0.0000   0.00
cos3    3    2    5    6    0.0      8.37    0.0    0.0000   0.00
cos3    7    5    8    9    0.0      8.37    0.0    0.0000   0.00
cos3    7    5    8    10   0.0      8.37    0.0    0.0000   0.00
```

```
cos3    6    5    8    9    0.0     8.37    0.0    0.0000   0.00
cos3    6    5    8    10   0.0     8.37    0.0    0.0000   0.00
cos3    10   8    11   12   0.0     8.37    0.0    0.0000   0.00
cos3    10   8    11   13   0.0     8.37    0.0    0.0000   0.00
cos3    9    8    11   12   0.0     8.37    0.0    0.0000   0.00
cos3    9    8    11   13   0.0     8.37    0.0    0.0000   0.00
cos3    9    8    11   14   0.0     8.37    0.0    0.0000   0.00
finish
Methane
nummols 1
atoms 5
    C       12.01100  0.42622000    1
    H        1.00794  0.03690000    1
    H        1.00794  0.03690000    1
    F       18.99800 -0.25001000    1
    F       18.99800 -0.25001000    1
bonds 4
harm   1   2     2808.12     1.0930
harm   1   3     2808.12     1.0930
harm   1   4     3091.37     1.3440
harm   1   5     3091.37     1.3440
angles 6
harm   2   1   3    326.040     109.2
harm   2   1   4    429.360     108.5
harm   2   1   5    429.360     108.5
harm   3   1   4    429.360     108.5
harm   3   1   5    429.360     108.5
harm   4   1   5    595.232     107.1
finish
vdw 15
C       C          lj  0.27614     3.50
H       H          lj  0.12552     2.50
N       N          lj  0.71128     3.25
P       P          lj  0.83680     3.74
F       F          lj  0.25520     3.12
C       H          lj  0.18617     2.95
C       N          lj  0.44318     3.37
C       P          lj  0.48070     3.61
C       F          lj  0.26546     3.30
H       N          lj  0.29879     2.85
H       P          lj  0.32409     3.06
H       F          lj  0.17897     2.79
N       P          lj  0.77149     3.49
N       F          lj  0.42605     3.18
P       F          lj  0.46211     3.41

close
```

```
# Partial Charges and structure and bmim bonds
# from Ab initio Calcs by Adams group.
# bmim bends and dihedrals, and all lj from
# Lopes et all J Phys Chem B 2004
# imidazole ring dihedrals from Alavi et all
# where not listed lj generated by standard combination
# PF6 parameters from Lopes et al
# J Phys Chem B 2004
# CFnHn Bonds taken from gaff

# LJ parms from above refs
```

References Cited:

1. Canongia Lopes, J. N.; Deschamps, J.; Pádua, A. A. H., Modeling Ionic Liquids Using a Systematic All-Atom Force Field. *Journal of Physical Chemistry B* **2004,** *108* (6), 2038-2047.

2. Bhargava, B. L.; Balasubramanian, S., Refined potential model for atomistic simulations of ionic liquid [bmim] [P F6]. *Journal of Chemical Physics* **2007,** *127* (11).

3. Nathanson, G. M.; Davidovits, P.; Worsnop, D. R.; Kolb, C. E., Dynamics and kinetics at the gas-liquid interface. *The Journal of Physical Chemistry®* **1996,** *100* (31), 13007-13020.

4. Agarwal, A. K., Biofuels (alcohols and biodiesel) applications as fuels for internal combustion engines. *Progress in Energy and Combustion Science* **2007,** *33* (3), 233-271.

5. Cerci, Y., Performance evaluation of a single-flash geothermal power plant in Denizli, Turkey. *Energy* **2003,** *28* (1), 27-35.

6. Doney, S. C.; Fabry, V. J.; Feely, R. A.; Kleypas, J. A., Ocean acidification: The other CO2 problem. *Annual Review of Marine Science* **2009,** *1*, 169-192.

7. Farquhar, G. D.; von Caemmerer, S.; Berry, J. A., A biochemical model of photosynthetic CO2 assimilation in leaves of C3 species. *Planta* **1980,** *149* (1), 78-90.

8. Feely, R. A.; Sabine, C. L.; Lee, K.; Berelson, W.; Kleypas, J.; Fabry, V. J.; Millero, F. J., Impact of anthropogenic CO2 on the CaCO3 system in the oceans. *Science* **2004,** *305* (5682), 362-366.

9. Phillips, C. S. G., II(B). Organic and biochemical: The chromatography of gases and vapours. *Discussions of the Faraday Society* **1949,** *7*, 241-248.

10. Redhead, P. A., Thermal desorption of gases. *Vacuum* **1962,** *12* (4), 203-211.

11. Nathanson, G. M., Molecular beam studies of gas-liquid interfaces. In *Annual Review of Physical Chemistry*, 2004; Vol. 55, pp 231-255.

12. Bosio, S. B. M.; Hase, W. L., Energy transfer in rare gas collisions with self-assembled monolayers. *Journal of Chemical Physics* **1997,** *107* (22), 9677-9686.

13. Lu, J. W.; Alexander, W. A.; Morris, J. R., Gas-surface energy exchange and thermal accommodation of CO2 and Ar in collisions with methyl, hydroxyl, and perfluorinated self-assembled monolayers. *Physical Chemistry Chemical Physics* **2010,** *12* (39), 12533-12543.

14. Behr, P.; Scharfenort, U.; Zellner, R., Collisions of noble gases with supercooled sulfuric acid-water solutions. *Physical Chemistry Chemical Physics* **2009,** *11* (33), 7292-7302.

15. Perkins Jr, B. G.; Häber, T.; Nesbitt, D. J., Quantum state-resolved energy transfer dynamics at gas-liquid interfaces: IR laser studies of CO2 scattering from perfluorinated liquids. *Journal of Physical Chemistry B* **2005,** *109* (34), 16396-16405.

16. Chase, D.; Manning, M.; Morgan, J. A.; Nathanson, G. M.; Gerber, R. B., Argon scattering from liquid indium: Simulations with embedded atom potentials and experiment. *Journal of Chemical Physics* **2000,** *113* (20), 9279-9287.

17. Lu, J. W.; Day, B. S.; Fiegland, L. R.; Davis, E. D.; Alexander, W. A.; Troya, D.; Morris, J. R., Interfacial energy exchange and reaction dynamics in collisions of gases on model organic surfaces. *Progress in Surface Science* **2012,** *87* (9-12), 221-252.

18. Perkins Jr, B. G.; Nesbitt, D. J., Toward three-dimensional quantum state-resolved collision dynamics at the gas-liquid interface: Theoretical investigation of incident angle. *Journal of Physical Chemistry A* **2009,** *113* (16), 4613-4625.

19. Reinhold, J.; Veltzke, T.; Wells, B.; Schneider, J.; Meierhofer, F.; Colombi Ciacchi, L.; Chaffee, A.; Thöming, J., Molecular dynamics simulations on scattering of single Ar, N2, and CO2 molecules on realistic surfaces. *Computers and Fluids* **2014,** *97*, 31-39.

20. Szabo, T. J.; Siavosh-Haghighi, A.; Adams, J. E., Energy transfer at a gas-liquid interface: Kinematics in a prototypical system. *Journal of Physical Chemistry B* **2006,** *110* (3), 1319-1325.

21. Hayes, W. W.; Manson, J. R., Rare gas collisions with molten metal surfaces. *The Journal of Chemical Physics* **2007,** *127* (16), 164714.

22. Lipkin, N.; Gerber, R. B.; Moiseyev, N.; Nathanson, G. M., Atom scattering studies of liquid structure and dynamics: Collisions of Xe with a model of squalane. *The Journal of Chemical Physics* **1994,** *100* (11), 8408-8417.

23. Perkins Jr, B. G.; Nesbitt, D. J., Quantum state-resolved CO2 collisions at the gas - liquid interface: Surface temperature-dependent scattering dynamics. *Journal of Physical Chemistry B* **2008,** *112* (2), 507-519.

24. Saecker, M. E.; Govoni, S. T.; Kowalski, D. V.; King, M. E.; Nathanson, G. M., Molecular Beam Scattering from Liquid Surfaces. *Science* **1991,** *252* (5011), 1421-1424.

25. Perkins Jr, B. G.; Nesbitt, D. J., Stereodynamics in state-resolved scattering at the gas-liquid interface. *Proceedings of the National Academy of Sciences of the United States of America* **2008,** *105* (35), 12684-12689.

26. Phillips, L. F.; Nesbitt, D. J., A 'hot-spot' model for impulsive scattering at the gas-liquid interface. *Chemical Physics Letters* **2012,** *546*, 53-57.

27. Perkins Jr, B. G.; Nesbitt, D. J., Correlated angular and quantum state-resolved CO2 scattering dynamics at the gas-liquid interface. *Journal of Physical Chemistry A* **2008,** *112* (39), 9324-9335.

28. Mallat, T.; Baiker, A., Oxidation of alcohols with molecular oxygen on solid catalysts. *Chemical Reviews* **2004,** *104* (6), 3037-3058.

29. Somorjai, G. A.; Park, J. Y., Concepts, instruments, and model systems that enabled the rapid evolution of surface science. *Surface Science* **2009,** *603* (10-12), 1293-1300.

30. Alexander, W. A.; Zhang, J.; Murray, V. J.; Nathanson, G. M.; Minton, T. K., Kinematics and dynamics of atomic-beam scattering on liquid and self-assembled monolayer surfaces. *Faraday Discussions* **2012,** *157* (0), 355-374.

31. Tribe, L.; Manning, M.; Morgan, J. A.; Stephens, M. D.; Ronk, W. R.; Treptow, E.; Nathanson, G. M.; Skinner, J. L., Argon scattering off the surface of liquid indium: Exit angle and energy dependence. *Journal of Physical Chemistry B* **1998,** *102* (1), 206-211.

32. Kolasinski, K. W., *Surface science : foundations of catalysis and nanoscience*. Wiley: Chichester ; New York, 2002; p xx, 305 p.

33. Adams, J. E.; Siavosh-Haghighi, A., Rotational relaxation in supercritical CO2. *Journal of Physical Chemistry B* **2002,** *106* (33), 7973-7980.

34. Wigley, T. M. L.; Richels, R.; Edmonds, J. A., Economic and environmental choices in the stabilization of atmospheric CO2 concentrations. *Nature* **1996,** *379* (6562), 240-243.

35. Lu, J. W.; Morris, J. R., Gas-surface scattering dynamics of CO 2, NO 2, and O 3 in collisions with model organic surfaces. *Journal of Physical Chemistry A* **2011,** *115* (23), 6194-6201.

36. Tostmann, H.; DiMasi, E.; Pershan, P. S.; Ocko, B. M.; Shpyrko, O. G.; Deutsch, M., Surface structure of liquid metals and the effect of capillary waves: X-ray studies on liquid indium. *Physical Review B - Condensed Matter and Materials Physics* **1999,** *59* (2), 783-791.

37. Todorov, I. T.; Smith, W.; Trachenko, K.; Dove, M. T., DL_POLY_3: New dimensions in molecular dynamics simulations via massive parallelism. *Journal of Materials Chemistry* **2006,** *16* (20), 1911-1918.

38. Harris, J. G.; Yung, K. H., Carbon Dioxide's Liquid-Vapor Coexistence Curve And Critical Properties as Predicted by a Simple Molecular Model. *The Journal of Physical Chemistry* **1995,** *99* (31), 12021-12024.

39. Keller, J. U.; Staudt, R., *Gas Adsorption Equilibria: Experimental Methods and Adsorptive Isotherms*. Springer US: 2006.

40. Perkins Jr, B. G.; Nesbitt, D. J., High resolution Dopplerimetry of correlated angular and quantum state-resolved CO2 scattering dynamics at the gas-liquid interface. *Physical Chemistry Chemical Physics* **2010,** *12* (42), 14294-14308.

41. Phillips, L. F., Processes at the gas-liquid interface. *International Reviews in Physical Chemistry* **2011,** *30* (3), 301-333.

42. Center, W. M. N. I. W. M. R., *Green Solvents for Chemistry : Perspectives and Practice: Perspectives and Practice*. Oxford University Press, USA: 2003.

43. Van Den Berg, M.; Birnbaum, L.; Bosveld, A. T. C.; Brunström, B.; Cook, P.; Feeley, M.; Giesy, J. P.; Hanberg, A.; Hasegawa, R.; Kennedy, S. W.; Kubiak, T.; Larsen, J. C.; Van Leeuwen, F. X. R.; Liem, A. K. D.; Nolt, C.; Peterson, R. E.; Poellinger, L.; Safe, S.; Schrenk, D.; Tillitt, D.; Tysklind, M.; Younes, M.; Wærn, F.; Zacharewski, T., Toxic equivalency factors (TEFs) for PCBs, PCDDs, PCDFs for humans and wildlife. *Environmental Health Perspectives* **1998,** *106* (12), 775-792.

44. Mastrangelo, G.; Fadda, E.; Marzia, V., Polycyclic aromatic hydrocarbons and cancer in man. *Environmental Health Perspectives* **1996,** *104* (11), 1166-1170.

45. Welton, T., Room-Temperature Ionic Liquids. Solvents for Synthesis and Catalysis. *Chemical Reviews* **1999,** *99* (8), 2071-2083.

46. Buzzeo, M. C.; Hardacre, C.; Compton, R. G., Use of room temperature ionic liquids in gas sensor design. *Analytical Chemistry* **2004,** *76* (15), 4583-4588.

47. Dupont, J.; De Souza, R. F.; Suarez, P. A. Z., Ionic liquid (molten salt) phase organometallic catalysis. *Chemical Reviews* **2002,** *102* (10), 3667-3692.

48. Mackenzie, J. D., The physical chemistry of simple molten glasses. *Chemical Reviews* **1956,** *56* (3), 455-470.

49. Wilkes, J. S.; Levisky, J. A.; Wilson, R. A.; Hussey, C. L., Dialkylimidazolium chloroaluminate melts: A new class of room-temperature ionic liquids for electrochemistry, spectroscopy, and synthesis. *Inorganic Chemistry* **1982,** *21* (3), 1263-1264.

50. Bates, E. D.; Mayton, R. D.; Ntai, I.; Davis Jr, J. H., CO2 capture by a task-specific ionic liquid. *Journal of the American Chemical Society* **2002,** *124* (6), 926-927.

51. Camper, D.; Bara, J. E.; Gin, D. L.; Noble, R. D., Room-temperature ionic liquid-amine solutions: Tunable solvents for efficient and reversible capture of CO2. *Industrial and Engineering Chemistry Research* **2008,** *47* (21), 8496-8498.

52. Galiński, M.; Lewandowski, A.; Stepniak, I., Ionic liquids as electrolytes. *Electrochimica Acta* **2006,** *51* (26), 5567-5580.

53. Lewandowski, A.; Świderska-Mocek, A., Ionic liquids as electrolytes for Li-ion batteries-An overview of electrochemical studies. *Journal of Power Sources* **2009,** *194* (2), 601-609.

54. Sakaebe, H.; Matsumoto, H.; Tatsumi, K., Application of room temperature ionic liquids to Li batteries. *Electrochimica Acta* **2007,** *53* (3 SPEC. ISS.), 1048-1054.

55. Hallett, J. P.; Welton, T., Room-temperature ionic liquids: Solvents for synthesis and catalysis. 2. *Chemical Reviews* **2011,** *111* (5), 3508-3576.

56. Morgan, D.; Ferguson, L.; Scovazzo, P., Diffusivities of gases in room-temperature ionic Liquids: Data and correlations obtained using a lag-time technique. *Industrial and Engineering Chemistry Research* **2005,** *44* (13), 4815-4823.

57. Hayamizu, K.; Aihara, Y.; Nakagawa, H.; Nukuda, T.; Price, W. S., Ionic conduction and ion diffusion in binary room-temperature ionic liquids composed of [emim][BF4] and LiBF4. *Journal of Physical Chemistry B* **2004,** *108* (50), 19527-19532.

58. Tokuda, H.; Hayamizu, K.; Ishii, K.; Susan, M. A. B. H.; Watanabe, M., Physicochemical properties and structures of room temperature ionic liquids. 1. Variation of anionic species. *Journal of Physical Chemistry B* **2004,** *108* (42), 16593-16600.

59. Tokuda, H.; Hayamizu, K.; Ishii, K.; Susan, M. A. B. H.; Watanabe, M., Physicochemical properties and structures of room temperature ionic liquids. 2. variation of alkyl chain length in imidazolium cation. *Journal of Physical Chemistry B* **2005,** *109* (13), 6103-6110.

60. Zhao, W.; Leroy, F.; Heggen, B.; Zahn, S.; Kirchner, B.; Balasubramanian, S.; Müller-Plathe, F., Are there stable ion-pairs in room-temperature ionic liquids? Molecular dynamics simulations of 1-n-butyl-3-methylimidazolium hexafluorophosphate. *Journal of the American Chemical Society* **2009,** *131* (43), 15825-15833.

61. Shim, Y.; Kim, H. J., Dielectric relaxation, ion conductivity, solvent rotation, and solvation dynamics in a room-temperature ionic liquid. *Journal of Physical Chemistry B* **2008,** *112* (35), 11028-11038.

62. Liu, Z.; Huang, S.; Wang, W., A refined force field for molecular simulation of imidazolium-based ionic liquids. *Journal of Physical Chemistry B* **2004,** *108* (34), 12978-12989.

63. Moganty, S. S.; Baltus, R. E., Diffusivity of carbon dioxide in room-temperature ionic liquids. *Industrial and Engineering Chemistry Research* **2010,** *49* (19), 9370-9376.

64. Shiflett, M. B.; Yokozeki, A., Solubility and diffusivity of hydrofluorocarbons in room-temperature ionic liquids. *AIChE Journal* **2006,** *52* (3), 1205-1219.

65. Ying, H.; Baltus, R. E., Experimental measurement of the solubility and diffusivity of CO 2 in room-temperature ionic liquids using a transient thin-liquid-film method. *Industrial and Engineering Chemistry Research* **2007,** *46* (24), 8166-8175.

66. Kowsari, M. H.; Alavi, S.; Ashrafizaadeh, M.; Najafi, B., Molecular dynamics simulation of imidazolium-based ionic liquids. II. Transport coefficients. *Journal of Chemical Physics* **2009,** *130* (1).

67. Lynden-Bell, R. M.; Del Pópolo, M., Simulation of the surface structure of butylmethylimidazolium ionic liquids. *Physical Chemistry Chemical Physics* **2006,** *8* (8), 949-954.

68. Margulis, C. J.; Stern, H. A.; Berne, B. J., Computer simulation of a "green chemistry" room-temperature ionic solvent. *Journal of Physical Chemistry B* **2002,** *106* (46), 12017-12021.

69. Morrow, T. I.; Maginn, E. J., Molecular dynamics study of the ionic liquid 1-n-butyl-3-methylimidazolium hexafluorophosphate. *Journal of Physical Chemistry B* **2002,** *106* (49), 12807-12813.

70. Tsuzuki, S.; Shinoda, W.; Saito, H.; Mikami, M.; Tokuda, H.; Watanabe, M., Molecular dynamics simulations of ionic liquids: Cation and anion dependence of self-diffusion coefficients of ions. *Journal of Physical Chemistry B* **2009,** *113* (31), 10641-10649.

71. Umecky, T.; Kanakubo, M.; Ikushima, Y., Self-diffusion coefficients of 1-butyl-3-methylimidazolium hexafluorophosphate with pulsed-field gradient spin-echo NMR technique. *Fluid Phase Equilibria* **2005,** *228-229*, 329-333.

72. Antony, J. H.; Mertens, D.; Dölle, A.; Wasserscheid, P.; Carper, W. R., Molecular reorientational dynamics of the neat ionic liquid 1-butyl-3-methylimidazolium hexafluorophosphate by measurement of 13C nuclear magnetic relaxation data. *ChemPhysChem* **2003,** *4* (6), 588-594.

73. Gurkan, B. E.; De La Fuente, J. C.; Mindrup, E. M.; Ficke, L. E.; Goodrich, B. F.; Price, E. A.; Schneider, W. F.; Brennecke, J. F., Equimolar CO2 absorption by anion-functionalized ionic liquids. *Journal of the American Chemical Society* **2010,** *132* (7), 2116-2117.

74. Finotello, A.; Bara, J. E.; Camper, D.; Noble, R. D., Room-temperature ionic liquids: Temperature dependence of gas solubility selectivity. *Industrial and Engineering Chemistry Research* **2008,** *47* (10), 3453-3459.

75. Hudiono, Y. C.; Carlisle, T. K.; Bara, J. E.; Zhang, Y.; Gin, D. L.; Noble, R. D., A three-component mixed-matrix membrane with enhanced CO2 separation properties based on zeolites and ionic liquid materials. *Journal of Membrane Science* **2010,** *350* (1-2), 117-123.

76. Frisch, M. J. T., G. W.; Schlegel, H. B.; Scuseria, G. E.; Robb, M. A.; Cheeseman, J. R.; Montgomery, Jr., J. A.; Vreven, T.; Kudin, K. N.; Burant, J. C.; Millam, J. M.; Iyengar, S. S.; Tomasi, J.; Barone, V.; Mennucci, B.; Cossi, M.; Scalmani, G.; Rega, N.; Petersson, G. A.; Nakatsuji, H.; Hada, M.; Ehara, M.; Toyota, K.; Fukuda, R.; Hasegawa, J.; Ishida, M.; Nakajima, T.; Honda, Y.; Kitao, O.; Nakai, H.; Klene, M.; Li, X.; Knox, J. E.; Hratchian, H. P.; Cross, J. B.; Bakken, V.; Adamo, C.; Jaramillo, J.; Gomperts, R.; Stratmann, R. E.; Yazyev, O.; Austin, A. J.; Cammi, R.; Pomelli, C.; Ochterski, J. W.; Ayala, P. Y.; Morokuma, K.; Voth, G. A.; Salvador, P.; Dannenberg, J. J.; Zakrzewski, V. G.; Dapprich, S.; Daniels, A. D.; Strain, M. C.; Farkas, O.; Malick, D. K.; Rabuck, A. D.; Raghavachari, K.; Foresman, J. B.; Ortiz, J. V.; Cui, Q.; Baboul, A. G.; Clifford, S.; Cioslowski, J.; Stefanov, B. B.; Liu, G.; Liashenko, A.; Piskorz, P.; Komaromi, I.; Martin, R. L.; Fox, D. J.; Keith, T.; Al-Laham, M. A.; Peng, C. Y.; Nanayakkara, A.; Challacombe, M.; Gill, P. M. W.; Johnson, B.; Chen, W.; Wong, M. W.; Gonzalez, C.; and Pople, J. A. *Gaussian 03*, Revision E.01; Gaussian, Inc: Wallingford CT.

77. Breite, M. D.; Cox, J. R.; Adams, J. E., Energetics of intercavity diffusion in a simple model of a low-density p-tert-butylcalix[4]arene crystal. *Journal of the American Chemical Society* **2010,** *132* (32), 10996-10997.

78. Wang, J.; Wang, W.; Kollman, P. A.; Case, D. A., Automatic atom type and bond type perception in molecular mechanical calculations. *Journal of Molecular Graphics and Modelling* **2006,** *25* (2), 247-260.

79. Pearlman, D. A.; Case, D. A.; Caldwell, J. W.; Ross, W. S.; Cheatham Iii, T. E.; DeBolt, S.; Ferguson, D.; Seibel, G.; Kollman, P., AMBER, a package of computer programs for applying molecular mechanics, normal mode analysis, molecular dynamics and free energy calculations to simulate the structural and energetic properties of molecules. *Computer Physics Communications* **1995,** *91* (1-3), 1-41.

80. Wang, J.; Wolf, R. M.; Caldwell, J. W.; Kollman, P. A.; Case, D. A., Development and testing of a general Amber force field. *Journal of Computational Chemistry* **2004,** *25* (9), 1157-1174.

81. Alavi, S.; Thompson, D. L., Molecular dynamics studies of melting and some liquid-state properties of 1-ethyl-3-methylimidazolium hexafluorophosphate [emim] [PF6]. *Journal of Chemical Physics* **2005,** *122* (15).

82. Einstein, A., *Investigations on the Theory of the Brownian Movement*. Dover Publications: 1956.

83. Liu, H.; Maginn, E., A molecular dynamics investigation of the structural and dynamic properties of the ionic liquid 1-n-butyl-3-methylimidazolium bis(trifluoromethanesulfonyl) imide. *Journal of Chemical Physics* **2011,** *135* (12).

84. Rey-Castro, C.; Vega, L. F., Transport properties of the ionic liquid 1-ethyl-3-methylimidazolium chloride from equilibrium molecular dynamics simulation. the effect of temperature. *Journal of Physical Chemistry B* **2006,** *110* (29), 14426-14435.

85. *MATLAB and Statistics Toolbox Release 2012a*, The MathWorks, Inc.: Natick, Massachusetts, 2012.

VITA

Daniel Shaughnessy was born in New York, New York on April 5th 1984. He graduated high school from Saint Mary's Hall in San Antonio, TX in 2002. He received his Bachelor of Arts in Chemistry from Westminster College in 2007. He was accepted as a chemistry PhD candidate by the Chemistry Department of the University of Missouri-Columbia in 2007 and achieved his degree in May of 2015.